Micromechanical Resonant Switches ("Resoswitches") and Resonant Power Converters

Yang Lin

Electrical Engineering and Computer Sciences
University of California at Berkeley

December 1, 2015

Micromechanical Resonant Switches ("Resoswitches")
and Resonant Power Converters

By

Yang Lin

A dissertation submitted in partial satisfaction of the

requirements for the degree of

Doctor of Philosophy

in

Engineering − Electrical Engineering and Computer Sciences

in the

Graduate Division

of the

University of California, Berkeley

Committee in charge:

Professor Clark T.-C. Nguyen
Professor Tsu-Jae King Liu
Professor Liwei Lin

Fall 2014

Micromechanical Resonant Switches ("Resoswitches")
and Resonant Power Converters

Abstract

Micromechanical Resonant Switches ("Resoswitches") and Resonant Power Converters

by

Yang Lin

Doctor of Philosophy in Electrical Engineering and Computer Sciences

University of California, Berkeley

Professor Clark T.-C. Nguyen, Chair

Micromechanical resonant switches ("resoswitches") that harness the high-Q resonance and nonlinear dynamical properties of micromechanical structures are demonstrated that can achieve higher switching speed, better reliability (even under hot switching), and lower actuation voltage, all by substantial factors, over existing RF MEMS switches. Various mechanical structures (low to high resonance frequencies) with different structural and contact materials (medium to low resistances) are designed and fabricated to verify the advantages predicted by theory. Ample amounts of data were gathered and analyzed and new phenomena have been discovered.

The first prototype resoswitch was based on a 61MHz wine-glass mode disk constructed in doped polysilicon. As the pioneer demonstration vehicle, this device requires an actuation voltage of only 2V to switch with sub-nanosecond switching times. It further achieved over 16.7 trillion hot-switched cycles, made possible in part by a large restoring force (>160mN) afforded it orders of magnitude larger stiffness than conventional RF MEMS switches. The contact resistance is on the kilo ohm range but reasonable considering the fact that doped polysilicon is the contact interface. The already impressive 16.7 trillion hot-switched cycle life time might have been much longer if not for undesirable impacting at the drive port that occurred with this initial device.

An immediate solution to the high contact and series resistances of the polysilicon resoswitch is to construct everything in metal instead. Therefore, an electroplated nickel surface micromachining process was developed that allows for unequal electrode-to-resonator gap spacings in order to eliminate drive port impacting. The process uses only metal materials to keep the process temperature below 80°C in an effort to permit post CMOS process compatibility. This process led to demonstration of a 25MHz wine-glass mode nickel disk resoswitch that delivered 17.7dB of power gain in a simple power amplifier topology, where the power gain comes about mainly through substantial reduction

of contact resistance. Despite the introduction of unequal electrode-to-resonator gaps, endurance did not improve, mainly because the method used introduced an asymmetry that lowered the pull-in voltage of these devices.

To address this issue, a 153MHz digitally specified displacement amplifier was then designed that employs asymmetrical mechanical coupling to generate larger displacement along the switch axis than that along the drive axis. The prototype device used polysilicon structural material, so did not have a lower enough contact resistance to demonstrate an actual power amplifier. However, the device did greatly extend the hot-switched cycle life time, which now achieves 173.9 trillion cycles using an open-loop drive circuit. If driven by a closed-loop drive circuit, an even larger count is expected.

Finally, by synthesizing a group of comb-driven resoswitches, MEMS-based charge pumps were demonstrated with promise to eventually remove the diode voltage drop and junction breakdown issues that plague conventional transistor versions, allowing them to transfer charge with any input voltage level and achieve much higher voltages, perhaps eventually as high as 200V. A number of different topologies were successfully implemented, including single and multiple stages of Dickson's and charge transfer series voltage doubling designs, which proves the feasibility and agility of this technology.

Professor Clark T.-C. Nguyen

Committee Chair

To my wife, my sweet boy and my parents

Table of Contents

List of Figures

List of Tables

List of Symbols

ALD	Atomic Layer Deposition
CTS	Charge Transfer Series
DMD	Digital Micromirror Display
FEM	Finite Element Method
FET	Field Effect Transistor
FOM	Figure of Merit
FSK	Frequency Shift Keying
HBT	Heterojunction Bipolar Transistor
LPCVD	Low Pressure Chemical Vapor Deposition
LSI	Large Scale Integrated
MEMS	Micro-Electro-Mechanical Systems
NiTi	Nickel Titanium
ODE	Ordinary Differential Equation
PA	Power Amplifier
Q	Quality Factor
RF	Radio Frequency
RTA	Rapid Thermal Annealing
SEM	Scanning Electron Microscope
TiW	Titanium Tungsten
VHF	Very High Frequency

Acknowledgements

I sincerely would like to first express my gratitude towards my research advisor, Professor Clark T.-C. Nguyen, for his strict but patient inculcation and continuous support. It's been a great honor to be his student. His enthusiasm in micromechanical resonant devices; his beliefs in perfectionism and the spirit of never ever giving up any possibilities of exploring the truth will continue to guide me and encourage me in my future career and life.

Special thanks go to Professor Elad Alon, Professor Tsu-Jae King Liu and Professor Liwei Lin for their advice and inspiring discussions. I also thank Professor Kahlil Najafi for involving me in his research project when I was pursuing my MS degree in University of Michigan, Ann Arbor.

PhD life is mostly fun but sometimes could be extremely tedious, confusing or even frustrating. My all-time best friends in and out of the research lab, Chih-Ming Lin, Wei-Chang Li, Matilda Lai, and Tommi Riekkinen (in no particular order), have given me unbelievable technical and more importantly mental support and for that, they all deserve special thanks. In particular, Wei-Chang and I have spent many years working together including countless all nighters. His passion, determination and meticulousness have led to a great part of results in this work. Discussions with Chih-Ming and Matilda are always fun and encouraging and Chih-Ming's apartment near campus makes a prefect recharging station (dumplings and wii games) before pulling all nighters. Tommi is a knowledgeable friend and mentor to me and his dedicated advising helped me complete the metal switch project. Time spent with him debugging processes (and "golfing") and with his sweet family, especially his two little angels, Eva and Mona, is always delightful.

The help received from the senior students and engineers of Nguyen group, Jing Wang, Sheng-Shian Li, Yu-Wei Lin, Wen-Lung Huang and Zeying Ren, is highly appreciated. Sheng-Shian and Yu-Wei were always very patient answering my questions despite a very busy thesis writing time they were at. Jing's guidance in the first project I was assigned has made my transition from course work study to real research work smooth and steady. Wen-Lung and Zeying have spent considerable time teaching me in both clean room and the testing lab. Without their training, I would not have possessed timely the essential skills and hands on experiences that benefit substantially my following research work. Especially, Zeying's abundant experiences in microfabricaiton, humorous personality and willingness to lend a hand whenever I need it provide great psychological support in the clean room.

I'd also like to thank the other former or current Nguyen group members for their contribution and kind help, Mehmet Akgul, Bongsang Kim, Li-Wen Hung, Ilya Gurin, Ashkan Borna, Victor Yeh, Lingqi Wu, Robert Schneider, Henry Barrow, Brian Pepin, Thura Lin Naing, Tristan Rocheleau, Turker Beyazoglu, Ruonan Liu, Jalal Naghsh Nilchi,

Alper Ozgurluk and Divya Kashyap. I am also grateful for the warm companionship of all my good friends in Berkeley, Yenhao Philip Chen, Jun-Chao Chien, Nuo Zhang, Wenchao Li, Ryan Sochol, Adrienne Higa, Yingqi Jiang, Shijing Yao, Yue Lv, Jiashu Chen, Lingkai Kong, Hanh-Phuc Le, Wei Li, Huang Xiang, Zhichao Song, Huaming Xu, Yung-Kan Chen, Yu-Chu Huang, Yao-Ting Mao, etc.

This work would not have been possible without the assistance from all the staff of the Marvell Nanofabrication Laboratory (previously Berkeley Microfabrication Laboratory) especially Joe Donnelly and Xiaofang Meng, who have provided tremendous support on various metal evaporation and sputtering machines; Kim Chan and Evan Stateler, who were always extremely patient whenever I needed help on photolithography and SEM tools. Life in clean room has been much easier because of their expertise and professional suggestions.

I also want to thank the crew of BSAC's (Berkeley Sensor and Actuator Center) administrative office: John Huggins, Kim Ly, Richard Lossing, etc. for their decent organization. Those Tuesday noon's of biting yummy "Stuffed Inn" tuna sandwiches while listening to the intriguing seminar talks will always be remembered. I did my first ever academic presentation in BSAC IAB and Kim's magic words before each of my BSAC talks would always appease my nervousness. Experiences in BSAC IAB's are my lifetime great assets and I have been and will always be proud of being a "BSACer".

Lastly but not least, I should express my supreme gratitude towards my family. My parents' unconditional trust and love at all times have always been the propulsion forces that drive me to where I am now. Their everlasting encouragement and support null all my worries and concerns while chasing down this goal. Finally and most importantly, my wife, Lamei, has given me the deepest love since we met. Your absolute understanding and selfless devotion to our family are invaluable. I am almost speechless, as I can't find a word to describe how grateful I am at present. I love you, Lamei.

CHAPTER 1   *Introduction*

The history of MEMS switches dates back to the 1980's, though they did not gain serious attention until Dr. Larry Larson introduced the first MEMS switch in 1990 that was able to create open and short circuits in a transmission line in the radio frequency range [1]. In fact, that was the debut of the name "RF MEMS switches" and people almost automatically recognized it as the only kind of MEMS switches from then on. Although a number of companies (e.g., Motorola, Omron, Radant MEMS, Rockwell Scientific and Texas Instruments, etc.) and research labs have been making considerable effort since then, so far RF MEMS switches still exclusively focus on microwave applications, such as antenna switching and reconfigurable apertures. Part of the reason is that RF MEMS switch researchers have been focusing on improving the switch performance via: 1) scaling down device dimensions to obtain faster switching speed; 2) changing contact interface material or tuning alloy material composition to optimize insertion loss and cycle life time and 3) improving mechanical structure design to increase contact force. These are reasonable approaches to improve switch performance, but not strong enough to push them to a whole new level.

What is really needed here is to think outside the box, like the work of the resonant gate transistor [2] (*c.f.* Figure 1-1), where a suspended and movable beam (clamped-free or clamped-clamped) is driven into resonance dynamically changing the electric field within the channel and hence modulating the drain current. Inspired by that work and with the firm belief that MEMS switches should not be limited to applications in the microwave domain and should also be fairly competitive for applications where the field-effect transistor (FET) currently dominates, this dissertation proposes a brand new type of MEMS switch called the micromechanical resonant switch ("resoswitch"), which revolutionizes the way traditional MEMS switches operate by driving them into resonance. Benefits and issues for this new operation will be explained. For demonstration purpose, several prototype devices with different structures and materials were fabricated and characterized and exemplary new applications based upon them were successfully shown.
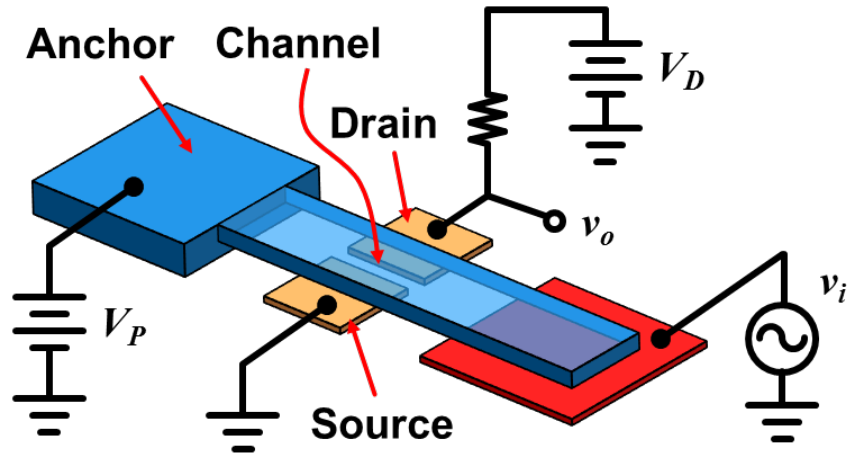
Figure 1-1: Schematic of a clamped-free resonant gate transistor.

While focusing mainly on the innovation of operation, the importance of fundamental research on other aspects of switches, such as contact interface materials and contact force engineering, is also emphasized. In fact, the introduction of the new MEMS resonant switches actually loosens up some design constraints and therefore helps to push the canonical studies towards broader design space.

1.1 Target Applications

Resonant switching means that the device is actuated with constant period. This immediately reminds us of the high volume applications, e.g., switched-mode power amplifier and power converter (*c.f.* Figure 1-2), where FET switches or p-i-n diodes are commonly used to modulate current or direct charge. The performance of the power amplifiers and power converters relies heavily on the figure of merit (*FOM*) of the regulating switches. Since switch devices are usually modeled as resistors in the "on" state, and capacitors in the "off" state, the microwave industry normally uses a $FOM = 1/(2\pi R_{on}C_{off})$, where R_{on} is on resistance, C_{off} is off capacitance, to gauge the switching characteristics of different switch elements. Higher *FOM* is favored because the highest frequency that the device can perform as a switch is about 1/10 of its *FOM*; meanwhile, high *FOM* also means higher efficiency.

MEMS switches offer lower C_{off} and intrinsic R_{on}, and thus higher switch *FOM* can be achieved which then leads to better off-state isolation and lower loss. In addition, MEMS switches are usually more linear, generating less harmonic distortion than solid state devices. Therefore, MEMS switches are probably better switch elements for the power amplifying and converting applications, depicted in Figure 1-2. This dissertation analyzes the deficiencies of conventional MEMS switches compared to solid state ones and explains how the proposed resonant operation addresses the issues to truly make
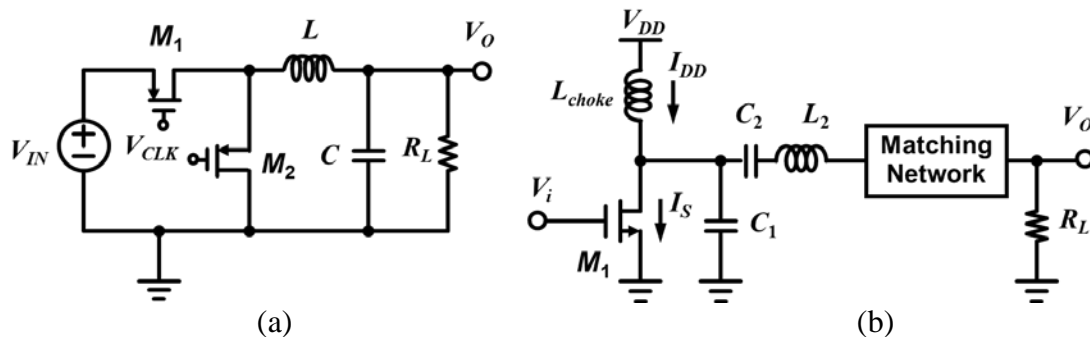
Figure 1-2: Circuit schematics of (a) switched-mode DC-DC power converter (buck step-down) and (b) switched-mode class-E power amplifiers.

MEMS switches suitable for low cost high efficiency power converters and power amplifiers.

Perhaps the biggest advantage of developing MEMS-based power converters and power amplifiers lies in benefiting MEMS technology itself, as MEMS devices generally require high voltages. If high bias voltages, on the order of 50-200V, were available on-chip, the corresponding increase in the electromechanical coupling strengths of many capacitively transduced MEMS devices, from gyroscopes, to micro-phones, to timing oscillators, would bring about substantial performance and cost benefits. Indeed, the size of a mechanical element can often be made substantially smaller when capacitive coupling becomes stronger, since less overlap is required to achieve a given coupling strength. If power management blocks can be implemented in MEMS domain, MEMS products will soon be decoupled from other technologies. By virtue of the flexibility and adaptivity of MEMS design and fabrication processes, given a MEMS device, MEMS switches (and hence MEMS power converters and amplifiers) can be constructed using virtually the same fabrication process sequence that achieved that MEMS device. In that case, a fully integrated self-biased MEMS sensor/actuator can be envisioned as follows: 1) MEMS power converters will be fabricated alongside with MEMS sensors and actuators to provide ultrahigh DC bias voltages that are becoming exponentially challenging as CMOS technology scales down; 2) MEMS power amplifiers will also be integrated to boost the output signal amplitude sufficient for post processing without extra conditioning.

1.2 DC-DC Power Converters

Of the various power management components, this dissertation will be primarily focusing on the potential for implementing DC-DC power converters using MEMS switches, not only because DC-DC power converters are strongly desired for many MEMS products, but also because they are very widely used in portable electronic devices, e.g., laptop computers, tablets and cell phones, whose markets are enormous and yet still expanding. Mobile devices are powered by batteries with output voltages ranging from 3-
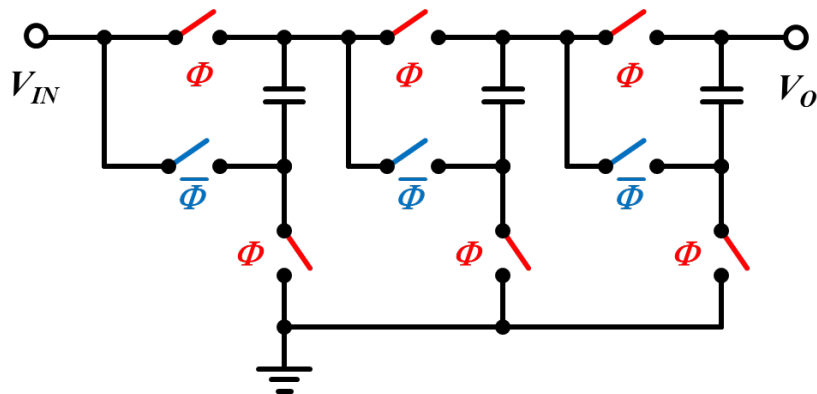
Figure 1-3: Circuit schematics of a serial-parallel type of switched capacitor DC-DC power converter.

12V, while chips they contain usually require supply voltages lower than that. DC-DC power converters are therefore demanded as they can boost or lower the battery DC voltage of the system to levels required by specific components. DC-DC converters have also gained growing attention as the number of cores within CPU's increases as it is beneficial to use independent power supplies for each constituent core [3].

Compared to traditional linear regulators, switching DC-DC converters offer higher efficiency over a wider range of output voltages [3] and more flexible functionality (step-up, step-down or invert). For decades, the inductor-based converter, as shown in Figure 1-1(a), has been the default design for switching type converters [4] [5], however, the inductors, which are acting as the energy storage elements, are either bulky when implemented as off-chip components or costly due to the needed additional fabrication steps if monolithic integration is desired. In contrast, on-chip capacitors, which are automatically integrated into the CMOS fabrication process, can provide substantially higher capacitance density and lower series resistance. Therefore, the switched capacitor DC-DC converters (*c.f.* Figure 1-3), which contain only capacitors as energy storing passives, can achieve much higher power and energy density while maintaining reasonably high efficiencies (60%-80%). As a result, this work, for demonstration purpose, targets to demonstrate switched capacitor DC-DC power converters that utilize resonant MEMS switches to transfer energy.

On the other hand, MEMS-based power converters are not limited to be of the switched capacitor type. Implementation of an integrated inductor-based design, which is still dominating the high power and tight regulation applications [6], is also practically achievable because the cumbersome (for CMOS technology) thick metal layer required by integrated inductors is longer an issue for MEMS processes. In fact, many MEMS devices use 10-100μm of electroplated metal as structural layer [7]. Therefore, when im-
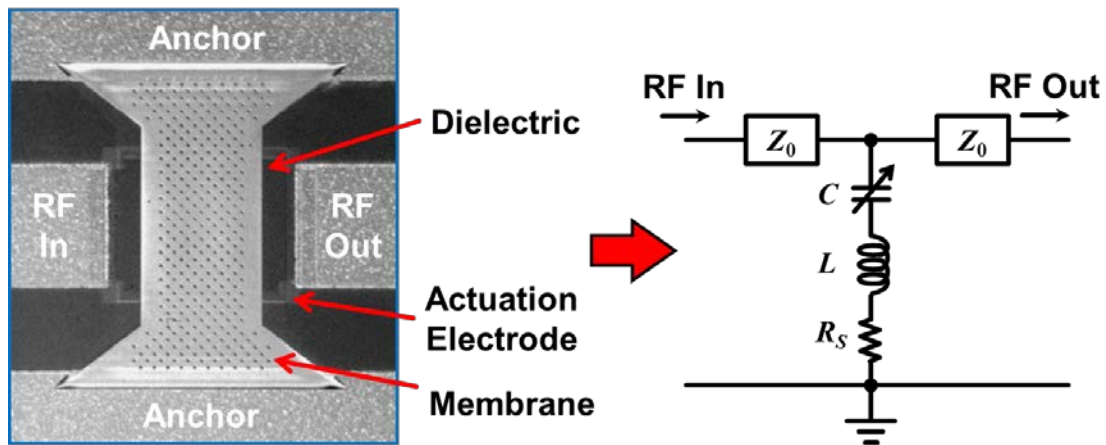
Figure 1-4: SEM picture of the Raytheon MEMS shunt switch and its equivalent circuit model.

Table 1-1: Parameters of the Raytheon MEMS switch.

Parameters	Values
C_{off}	35fF
R_{on}	0.3Ω
FOM	15THz
Actuation Voltage	30-50V
Switch Time	8μs

plemented using MEMS components, design of switching power converters can be much more flexible.

1.3 Conventional RFMEMS Switches

Conventional RF MEMS switches, no matter shunt [8] or series [9] configurations, are used to create open and short circuits in transmission lines, whereas the switches needed in the power converters and power amplifiers act as the charge regulating components. Figure 1-4 shows the SEM pictures and equivalent circuit model of the RF MEMS switch developed in Raytheon. Table 1-1 summarizes its parameters, where the reasons why it cannot be readily used as the building block of power converters and amplifiers are shown. Although having C_{off} and R_{on} as small as 35fF and 0.3Ω, respectively, and thus a switch FOM as high as 15THz, it switch time of 8μs in total greatly limits its max-

imum operating frequency to be 125kHz. In addition, the actuation voltage is 30-50V, which makes it a consumer of a DC-DC power converter instead of a provider. What plagues it even more is the fact that the hot switched life time is usually a few million cycles [10], several orders of magnitude below the number required by switching power converter and amplifier applications. Some parameters in Table 1-1 can be improved at the cost of worsening the others. For example, when the structure is made softer or the actuation gap is reduced to lower actuation voltage, such as the one demonstrated by [11], not only does restoring force that stands to overcome sticking becomes smaller therefore compromising the switch reliability but the switching speed also becomes slower. It seems that MEMS devices are facing a bottleneck.

Since mechanical optimization cannot solve all the issues, it calls for more fundamental reformation. Do mechanical devices have other unique properties that they can take advantage of to surmount solid state devices? The answer is yes. The success of high-Q micromechanical vibrating resonators [12] [13] reminds us there is at least one more merit that we can count on: resonance! If properly designed, resonant MEMS devices can have extremely high Q factors [14] [12], meaning that the mechanical movement in resonance can be amplified by Q times at nearly no additional energy cost. Benefiting from the displacement gain, the mechanical structures can then be designed to be much stiffer without worrying about actuation voltage, and stiffer structure subsequently improves both the reliability and the switching speed. With high *FOM* and high-Q resonance, MEMS switches are now truly ready to take off.

1.4 Conclusions

MEMS switches are promising switching elements for better power management components, but seemingly dilemmatic design issues has hindered their development and limited them to microwave switching applications. Operating traditional MEMS switches at resonance provides an excellent solution to this problem. The main goal of this dissertation is to investigate the validity of this new approach through theoretical derivation and experimental verification.

1.5 Overview

This dissertation starts in Chapter 2 with a detailed comparison between static and resonant switches followed by an experimental study on polysilicon wine-glass mode disk resoswitch that clearly shows the advantages of resonance operation. After that, in Chapter 3, a wine-glass mode disk resoswitch constructed in electroplated nickel is presented which achieves a R_{on} small enough for on-chip power amplification. Demonstration of these two early versions of resonant switches also exposes the design imperfection that causes switch degradation. Chapter 4 then proposes an asymmetrically coupled disk displacement amplifier that effectively avoids unwanted impacting at the input and the resoswitch based upon it does show an extended life time. Chapter 5 demonstrates the potential of resoswitch for switched capacitor power converters by constructing charge

pumps using comb-driven resoswitches. Using the comb-driven version resoswitch, dynamical instability of resoswitches is studied and the working solutions to tolerate unstable switching as well as fabrication induced resonance frequency variation are elucidated. Chapter 6 then discusses the frequency and Q variances that the resonant devices have due to finite fabrication tolerance. Finally, Chapter 7 wraps up with conclusions and suggestions for future work.

CHAPTER 2 *Micromechanical Resonant Switches ("Resoswitches")*

RF MEMS switches operating at RF to millimeter-wave frequencies substantially outperform p-i-n diode and FET counterparts in insertion loss, isolation, and switch figure of merit ($FOM = 1/(2\pi R_{on}C_{off})$, where R_{on} is on resistance, C_{off} is off capacitance) [8] [15] [16]. Unfortunately, their much slower switching speeds (e.g., 1-15µs versus the 0.16-1ns [17] of FET's) and cycle lifetimes on the order of 100 billion cycles (for the good ones [18]) relegates them mainly to antenna switching, reconfigurable aperture, and instrumentation applications, and precludes them from much higher volume applications, such as the switched-mode power amplifiers and power converters introduced in the previous chapter.

The main focus of this dissertation is on developing MEMS based switch-mode power converters and power amplifiers that can outperform the current FET ones. The key component, that makes this task possible, is a revolutionized MEMS switch. This chapter, therefore, concentrates on the mechanical design of this new kind of switch, describing its unique dynamic properties, followed by the fabrication and testing technologies.

2.1 Resonant Operation versus Non-Resonant Operation

Indeed, the benefits afforded to switched-mode power applications that would ensue if the transistors they presently employ were replaced by switches with *FOM*'s on the order of those exhibited by RF MEMS switches would be enormous. For example, switched-mode power amplifiers that ideally should be able to achieve 100% drain efficiency presently cannot attain such values in practical implementations, in part because the transistors they use for switching exhibit large input capacitance (for small "on" resistances) and are often limited in the supply voltages they can support. On the other hand, MEMS switches, being made of metal, have very small "on" resistances and would be able to support higher supply voltages. However, if they are to be used in switched-mode power applications, their actuation voltages would need to be lowered substantially (from >50V [8] down to the single-digit volt range), their speeds would need to be much

(a) Top View
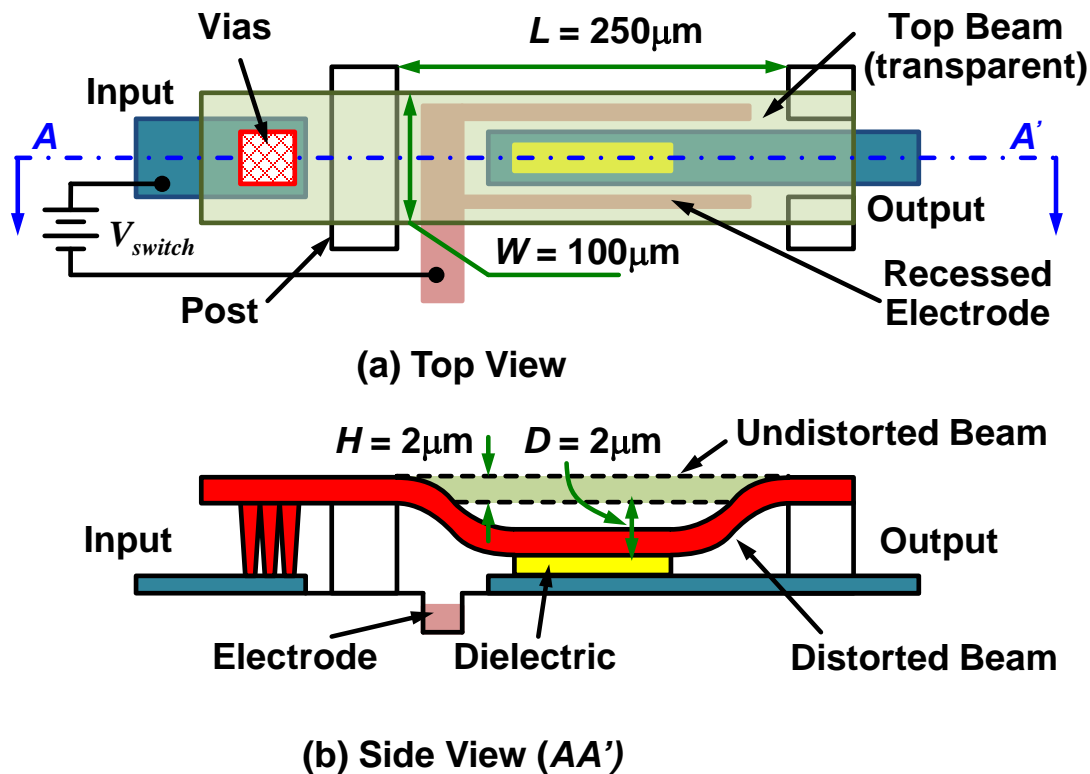
(b) Side View (*AA'*)

Figure 2-1: Schematic of a conventional micromechanical switch showing both (a) top and (b) cross-sectional side views, and indicating key dimensions.

higher (e.g., ns switching time), and their reliability enhanced substantially, since typical power amplifier and converter applications would require cycle counts in the quadrillions.

Pursuant to achieving a switch suitable for power amplifier and converter applications, this work demonstrates a micromechanical switch, dubbed the "resoswitch", that harnesses the resonance and nonlinear dynamical properties of its mechanical structure to greatly increase switching speed and cycle count (even under hot switching), and lower the needed actuation voltage, all by substantial factors over existing RF MEMS switches. All these improvements are brought by operating the switches at their resonances.

2.1.1 Lower Actuation Voltage

The advantages provided by a switch that harnesses resonance dynamics are perhaps best conveyed via comparison with conventional RF MEMS switch counterparts that do not. For this purpose, Figure 2-1 presents the top view and cross-section of a typical conventional RF MEMS switch, in this case one demonstrated by Goldsmith [8]. As shown, this switch consists of a metal membrane (or beam) suspended above a switch contact

Table 2-1: Geometrical Dimensions of the Switch Depicted in Figure 2-1.

Dimensions	Values
L	250 μm
W	100 μm
H	2 μm
D	2 μm
A	50 μm x100 μm

electrode that can be electrostatically pulled down onto the contact electrode by applying a sufficient actuation voltage V_{switch} to an underlying "gate" electrode. The switch is essentially a clamped-clamped beam whose stiffness and pull-in voltage can be evaluated as following:

$$k = 16\frac{EWH^3}{L^3} \tag{2.1}$$

$$V_P = \sqrt{\frac{8kD^3}{27A\varepsilon}} \tag{2.2}$$

where W, H, L and D are the dimensions labeled in Figure 2-1, A is the area of the actuation electrode, E is Young's modulus of the material and ε is the permittivity of the medium surrounding the device.

For the case of a suspended beam with the typical dimensions indicated in Table 2-1, the effective stiffness of the beam (at its midpoint) is on the order of 57 N/m, and the required actuation voltage (i.e. pull-in voltage) is about 55V, according to (2.1) and (2.2), respectively. It is noteworthy that (2.2) is a first order approximation to the pull-in voltage for the structure of Figure 2-1, and more accurate value can be obtained through FEM. Figure 2-2 shows a 3D FEM model built in ANSYS in order to calculate the electrostatic pull-in voltage. The mechanical structure is constructed by Solid185 element and the electrostatic field is modeled by Trans126 element. DC voltage V_{switch} is applied across the beam and the electrode and static analysis is performed to calculate the deflection of the beam. Figure 2-3 plots the maximum deflection of the beam versus V_{switch}, indicating

	Element Type
Structure	Solid185
Air gap	Trans126
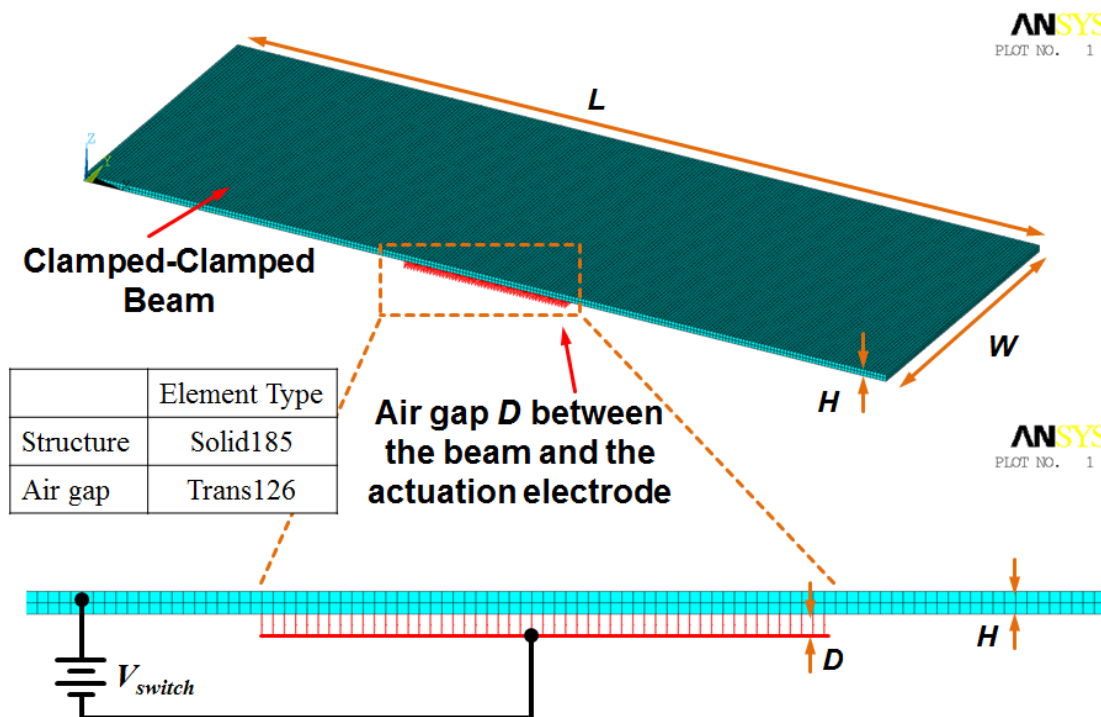
Figure 2-2: 3D FEM model of a clamped-clamped beam switch constructed in AN-SYS.

that the switch pulls in at an actuation voltage of about 60V. Similar results are also obtained by CoventorWare MEMS+ 3.0.

This actuation voltage can be lowered by either reducing the beam stiffness or reducing the gap spacing between the beam and the underlying electrode. Both of these approaches, however, come with drawbacks: the former reduces the restoring force with which the beam can overcome sticking forces, thereby sacrificing its reliability; while the latter not only decreases the restoring force but also increases the capacitance of the switch, thereby reducing its off-state isolation (and its *FOM*). It is these trade-offs that constrain the actuation voltages of RF MEMS switches to the 60V range, which in turn constrains their stiffness and mass to values that limit switching speed to microseconds and that compromises reliability.

Suppose now that the application for the switch is one that requires periodic switching, where the switch must turn on and off in with nearly constant period. Some of the highest volume applications of switches, namely switched-mode power converters [19] [20] [21] [22] and power amplifiers [23] [24], in fact operate in such a mode, where their switches switch continuously with essentially constant period within specified bandwidths. The use of a micromechanical switch in place of the switching transistor in these
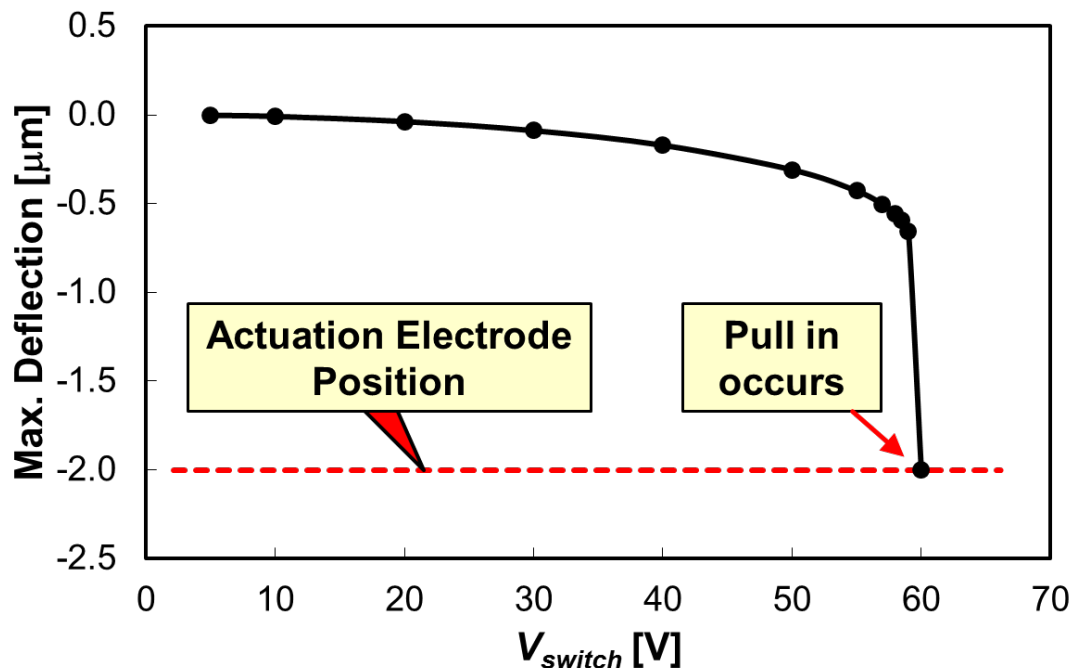
Figure 2-3: Simulated beam maximum deflection versus V_{switch} in ANSYS

applications stands to greatly enhance performance by raising the *FOM* of the switch and by allowing the use of much higher supply voltages (e.g., 10V vs. the 1V limit of conventional CMOS) [25], which raises the efficiency of switched-mode power amplifiers and raises the voltage levels achievable by boosting power converters.

Although it might be possible to utilize a properly scaled (to nanodimensions [26]) non-resonant switch that switches with constant period for such applications, it is much more advantageous to employ the resonance characteristics of the mechanical structure. In particular, if the switch of Figure 2-1 were driven by an actuation voltage at the resonance frequency of the beam, then the actuation voltage V_{switch} required to attain the same displacement of the beam (i.e., to close the switch) would be Q times smaller than that for off-resonance actuation inputs. In other words, if the beam had a Q of 5,000, then the needed actuation voltage would shrink from 55~60V, to only around 1-2V. To get the exact actuation voltage, a pre-stressed harmonic analysis is done in ANSYS. Besides that, to simulate the device more efficiently, an equivalent 2D FEM model, which is the cross-section of half of the 3D beam in Figure 2-2, is built as shown in Figure 2-4(a). A combination of a DC bias $V_P = 1.5V$ and an AC driving voltage $v_{in} = 1.5V$ are applied to the beam simultaneously and the displacement of the mid-point versus frequency is shown in Figure 2-4(b), indicating that an actuation voltage of 1.5V is sufficient to generate a displacement greater than 2μm at the mid-point making the beam to impact the bottom electrode and hence switch.
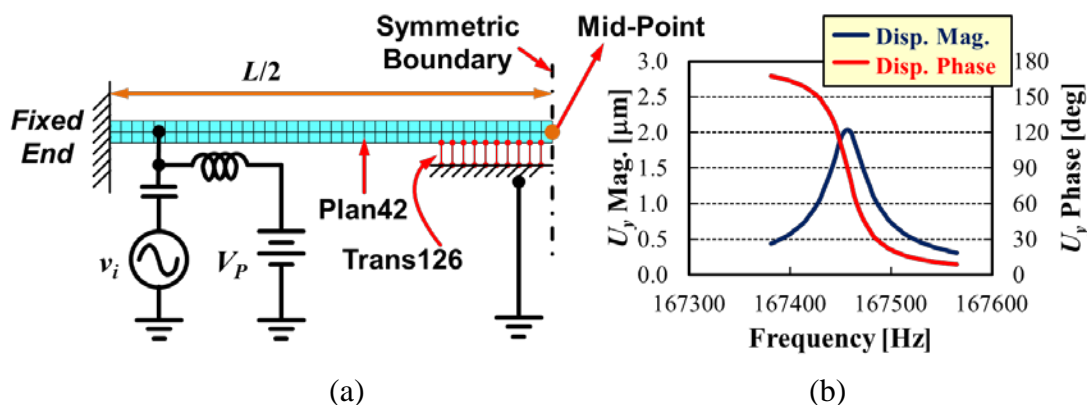
Figure 2-4: (a) Equivalent 2D model constructed in ANSYS using Plan42 and Trans126 elements and (b) the simulated displacement of the mid-point vs frequency.

In addition, the resonance frequency of a mechanical structure is close to the highest frequency at which it can operate, so operation at resonance maximizes the switching speed.

2.1.2 Larger Restoring Force

Orders of magnitude lower actuation voltage and faster switching speed already constitute tremendous improvement, but the advantages of resonance operation do not stop here. In particular, the actuation voltage (from the above example) need not be as small as 1.5V; rather, reduction of the actuation voltage down to 3V would already be compatible with advanced CMOS transistor technologies. To back off the actuation voltage, a designer might either raise the stiffness of the beam, by making it thicker or by shrinking its length dimension; or reduce the beam-to-drive electrode overlap capacitance, by increasing the beam-to-drive electrode gap spacing or by reducing its overlap area.

Raising stiffness is quite beneficial, since it effectively raises the speed of the switch by increasing its resonance frequency. It also improves the reliability of the switch by increasing the restoring force available to overcome adhesion forces that might otherwise cause the beam to stick to the electrode. For example, if the thickness of the beam of Figure 2-1 were increased to 5 µm, and its length reduced to 150 µm, then the effective beam stiffness at its midpoint would become 4,150 N/m, raising its frequency range (i.e., its resonance frequency) from 180 kHz to 1.06 MHz, which corresponds to a switching speed of $[(4)(1.06)(10^6)]^{-1} = 236$ ns, where switching speed here is approximated as one-fourth the switching period. The available restoring force is also increased by this design change from 0.11 mN to 8.3 mN, as illustrated by the following calculation:

Table 2-2: Comparisons of beam switches with different thickness.

Parameters	Original Values	Improved Values
D	2 µm	5 µm
L	250 mm	150 mm
f_o	0.18 MHz	1.06 MHz
t_{sw}	1389 nsec	236 nsec
$F_{restore}$	0.11 mN	8.3 mN

$$F_{restore} = k \cdot D = \begin{cases} 0.11 \, mN \Leftarrow k = 57 \, N/m \\ 8.3 \, mN \Leftarrow k = 4{,}150 \, N/m \end{cases} \tag{2.3}$$

where $F_{restore}$ is the restoring force, k is the stiffness of the beam, and D (=2 µm) is the distance between the beam and the contact electrode. Finally, despite the increase in stiffness, the needed resonance actuation voltage amplitude remains quite reasonably small, at a calculated 6.6 V. The calculations above are summarized in Table 2-2.

Beyond increasing stiffness, the other option for backing off on actuation voltage, i.e., decreasing the beam-to-electrode overlap capacitance, is also quite beneficial, since it reduces the off-state capacitance of the switch, thereby raising its *FOM*. Thus, the use of resonance operation improves switch performances in both the mechanical and electrical domains.

2.1.3 Larger Contact Force

What is more interesting, the resonance dynamical operation not only helps to improve reliability, but also provides a large impulsive contact force generated by impact that allows for a much smaller contact resistance than otherwise possible. Operating at resonance, the static contact of traditional switches now becomes dynamic impact, where much larger (usually 5~10x) instantaneous contact forces are available [27]. Modeling the dynamic behavior of the resoswitch starts by first solving the differential equation of motion, given by:

$$m_{re}\ddot{x} + c_{re}\dot{x} + k_{re}x = F \tag{2.4}$$
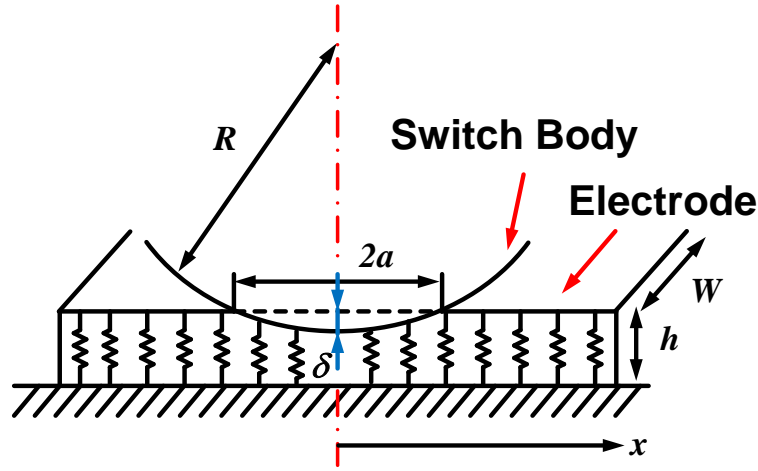
Figure 2-5: Schematic of a cylinder shape of body contacting an elastic foundation.

where m_{re}, c_{re}, k_{re} are the equivalent mass, damping and stiffness, respectively, of the resonator at the contact (i.e., impact) point, and F is the net force applied to drive the disk. Before contact, F comprises only an electrostatic force that takes the form:

$$F = \frac{1}{2}\left(V_P - v_i cos(\omega t)\right)^2 \frac{\partial C}{\partial x} \quad (x < d_o) \tag{2.5}$$

where V_P is the DC bias voltage applied to the disk, v_i is the amplitude of the AC voltage applied to the drive electrode as shown in Figure 2-4, and $\partial C/\partial x$ is the change in electrode-to-resonator capacitance per unit displacement. It is noteworthy that unlike [28], $\partial C/\partial x$ is a function of x now since the displacement range of interest here is much larger than those normally achieved in [28] and the value of $\partial C/\partial x$ increases rapidly as the gap approaches zero. When the displacement x becomes larger than the disk-to-electrode gap d_o along the switch axis, a second term that models the contact force arises to yield

$$F = \frac{1}{2}\left(V_P - v_i cos(\omega t)\right)^2 \frac{\partial C}{\partial x} - k_{contact}(x - d_o) \quad (x \geq d_o) \tag{2.6}$$

where $k_{contact}$ is the contact stiffness whose value depends on contact interface material properties and the contact shapes. The contact stiffness can be derived from contact mechanics theory. Of the various contact models, e.g., Hertz theory for non-adhesive elastic contact and Johnson-Kendall-Robert (JKR) model for adhesive elastic contact, Hertz theory is perhaps the simplest, so is used here.

For the clamped-clamped beam resoswitch shown in Figure 2-1, the electrode lying underneath the structure can be modeled as an elastic foundation as shown in Figure 2-5 [29]. The whole contact area is axis-symmetric about axis at the center denoted as the red dotted line. Profile of the switch penetrating into the electrode and contact pressure, which are all functions of x coordinate, can be expressed:

$$u(x) = \frac{a^2 - x^2}{2R} \quad (-a \leq x \leq a)$$

$$\delta = u(x = 0) = \frac{a^2}{2R} \tag{2.7}$$

$$p(x) = \frac{K(a^2 - x^2)}{2Rh}$$

where R is local radius of the beam at contact point, which can be calculated through the mode shape expression in [30]. a is half width of the contact area and δ is the maximum indentation located at the very center. K is the elastic modulus of the foundation, in this case Young's modulus of electrode material, and h is the thickness of the electrode. Integrating the contact pressure $p(x)$ over the contact area ([-a, a]) yields the net contact force:

$$F = \frac{2}{3} \frac{Ka^3}{hR} \tag{2.8}$$

Here, the force calculated is actually the contact force per unit length, as we assume the contact status is homogeneous along the beam width W direction. In order to be consistent with Hertz theory, one condition has to be met:

$$\frac{K}{h} = \frac{1.18E^*}{a} \tag{2.9}$$

where E^* is the contact modulus, which depends on the Young's Modulus E and Poisson's ratio ε of the contact bodies. And when contact bodies share the same E and ε, E^* becomes:

$$\frac{1}{E^*} = \frac{2(1 - \varepsilon^2)}{E} \tag{2.10}$$

Plugging (2.9) into (2.8), the contact force F can be rewritten as:

$$F = 0.787 \frac{E^* a^2}{R} \tag{2.11}$$

And thus, the equivalent contact stiffness $k_{contact}$ can then obtained by dividing the net contact force with the maximum indentation δ:

$$k_{contact} = \frac{F \cdot W}{\delta} = \frac{0.787 EW}{(1 - \varepsilon^2)} \tag{2.12}$$

This effective contact stiffness can then be used in the governing 2nd order differential equation of the system (2.4) to solve for the dynamic behavior of the switch numerically. In experimental study, one can also estimate the contact force by approximating the contact area size, 2a, from measuring the dimension of the beam crushing area under SEM [31].

For the switch shown in Figure 2-1, when actuated by the pull in voltage of 55V, around 480μN of contact force can be achieved. When driven at its resonance frequency with 3.6V, a dynamic impact force of 4mN can be obtained by solving (2.5) (2.6) and (2.12) with the dimensions summarized in Table 2-1. Even when the stiffness has been raised to 4,150N/m with the improved design shown in Table 2-2, 2mN of impact force can still be achieved with 8V of driving voltage applied. Larger contact force not only reduces the contact resistances but also makes available some materials, such as W, Mo, etc., that are previously considered too lossy for switch applications but are far more resistive to both mechanical wearing and hot-switched melting than Au, which is commonly used in RF MEMS switches.

As will be seen, the nonlinear dynamical behavior of the resoswitch offers even greater advantages for specific switched-mode applications, such as bandwidth and duty cycle control, which are important for power amplifiers and power converter applications.
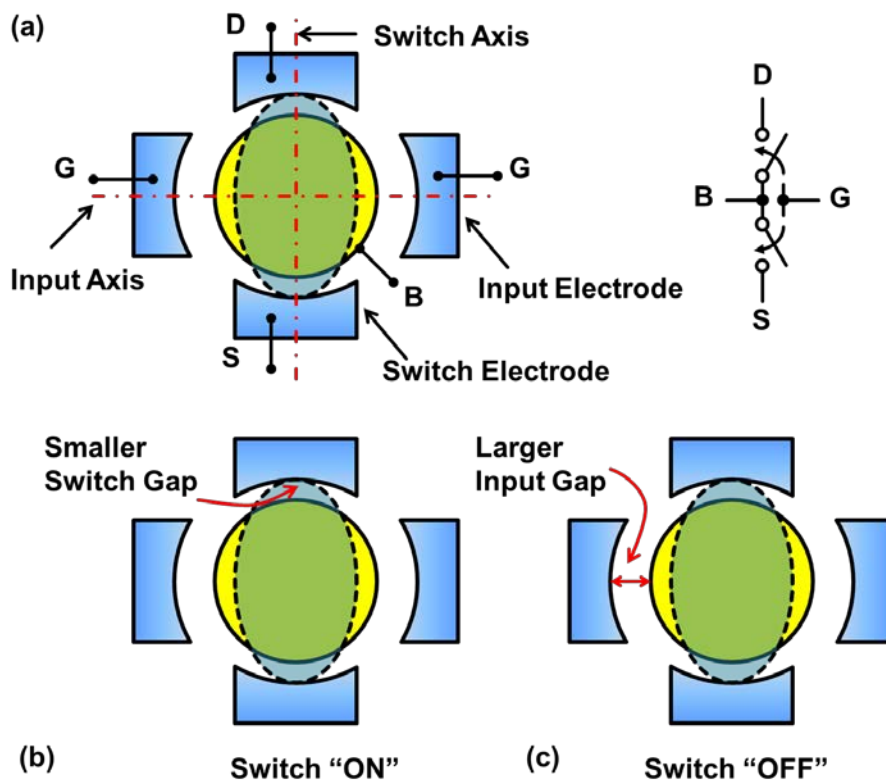
Figure 2-6: Schematics showing (a) the physical structure of the micromechanical resoswitch, identifying its ports and equating it to a functional equivalent circuit; (b) its "on"; and (c) its "off" states.

2.2 Polysilicon Wine-Glass Mode Disk Resoswitches

As summarized in the previous section, micromechanical resoswitches use resonance operation to greatly improve switch performance. In particular, when at resonance, displacements amplify by Q, so actuation voltages are small even though the stiffness of the device can be quite large. The large stiffness in turn allows very fast operation (due to the high resonance frequency) and very reliable operation, since large stiffness equates to large restoring forces against any sticking phenomenon. Although the resoswitch example so far discussed does present clear advantages over its non-resonant counterpart, its use of a clamped-clamped beam structure confines it to resonance frequencies lower than 100 MHz, since anchor losses plague this design at higher frequencies [32]. To attain the higher frequencies demanded by many switched-mode power amplifier applications, disk [33] or ring [34] resonator geometries are much more appropriate.

With this in mind, Figure 2-6 presents schematics describing the structure and operation of one simple rendition of a resoswitch that comprises a capacitively-transduced
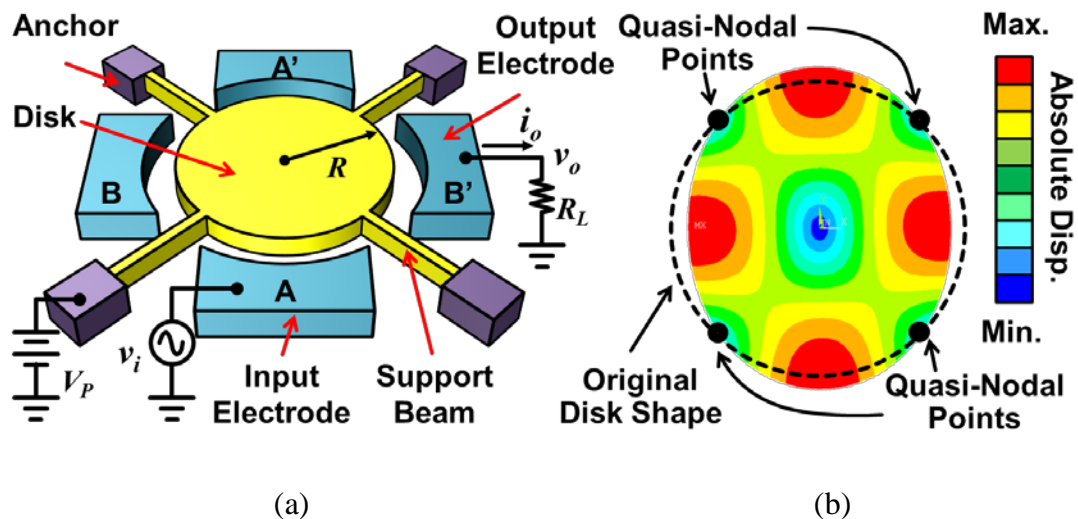
Figure 2-7: (a) Perspective-view schematic of a micromechanical wine-glass-mode disk resonator in a typical two-port bias and excitation configuration (where A, A' are electrically connected, as are B, B'). (b) ANSYS simulated wine-glass mode shape.

wine-glass disk micromechanical resonator [28] (*c.f.*, Figure 2-7) made in a conductive material (preferably, a metal) and surrounded by four electrodes, two of which are situated along an indicated input axis having larger electrode-to-resonator gaps than their counter-parts along an orthogonal switch axis.

To operate the switch, an ac input voltage at the wine-glass mode disk resonance frequency is applied to the input electrodes (along the input axis), electrically forcing the disk into the wine-glass mode shape delineated by the dotted curve in Figure 2-6(a).As the resonance amplitude rises, the disk eventually impacts the (closer) electrodes along the switch axis, as shown in Figure 2-6(b). This then ideally steals energy from the disk, effectively limiting its amplitude so that when the disk elongates along the input axis on the next cycle, it does not impact the (more distant) input electrodes, as shown in Figure 2-6(c). Essentially, in this structure, control electrodes more distant from the disk are used to drive the disk into its resonance mode shape (indicated by the dotted curve), where at sufficient amplitude it impacts closer electrodes along the orthogonal axis, closing the switch at a frequency equal to (or near) the resonance frequency of the disk. Because the input is applied at the resonance frequency of the disk, the required input voltage amplitude that effects switching along the switch axis is quite small, on the order of 1-3V, which is much smaller than the >50V required by most conventional RF MEMS switches.

Table 2-3: Parameters of 61MHZ Polysilicon Wine-glass Mode Disk Resoswitch.

Parameters	Values	Unit
Disk Radius, R	32	µm
Disk Thickness, H	2	µm
Input Electrode-to-Resonator Gap, d_i	100	nm
Output Electrode-to-Resonator Gap, d_o	50	nm
Resonator Quality Factor, Q	10,0000	–
Equivalent Stiffness, k_{re}	1.14×106	N/m
Equivalent Mass, m_{re}	8.03×10^{-12}	kg
Equivalent Damping, c_{re}	3.03×10^{-8}	N/ms^{-1}
DC-Bias voltage, V_P	10	V
AC Driving Signal Amplitude, v_i	0.6	V

As already mentioned, for the switched-mode power amplifier and power converter application targets of this dissertation, the cycle count of the resoswitch would need to be much larger (several quadrillions) than so far achieved by conventional non-resonant RF MEMS switches (1 trillion for the best "hero" devices [35]). In this regard, the reliability of the present resoswitch benefits from two major advantages:

1) The stiffness of its actuating disk resonator is on the order of 1.15×10^6N/m (for a 61-MHz wine-glass disk made of polysilicon), which is several orders larger than that of a conventional RF MEMS switch. Thus, with a full gap displacement of 80 nm, the structure provides a restoring force of 92mN much larger than the 0.11mN of conventional non-resonant counterparts, allowing it to much more effectively overcome sticking forces.

2) The energy stored via resonance vibration of the device provides a momentum that further increases the effective restoring force. In particular, depending upon the elasticity of the contact interface, a bounce effect helps to separate the vibrating disk from the impacted electrode, thereby further reducing the probably of sticking.

Again, the use of such a large spring restoring force is made possible by resonance operation, under which the displacement of the actuator is Q times larger than off-resonance, allowing a mere 1-3V amplitude drive voltage to generate impacting switch axis amplitudes in spite of the large stiffness of the disk structure.
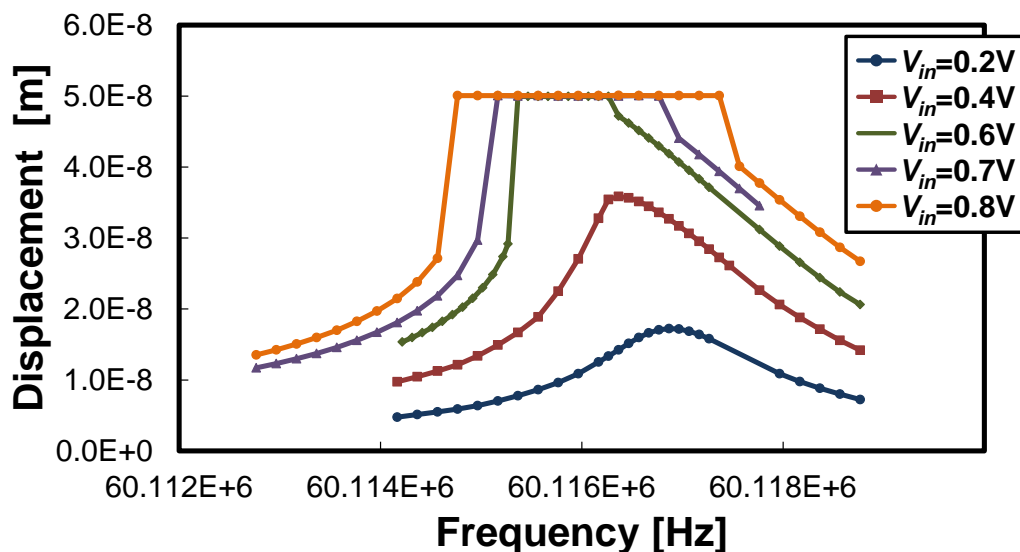
Figure 2-8: The displacement of a 61MHz wine-glass mode disk resoswitch versus frequencies of AC driving signal for various AC signal amplitudes simulated numerically using MATLAB.

2.2.1 Theoretical Modeling

The dynamical behavior of the wine-glass mode disk resoswitch can also be modeled by solving (2.5) and (2.6) with parameters summarized in Table 2-3. Figure 2-8 presents theoretical plots of disk displacement along the switch axis versus excitation frequency for various input AC signal amplitudes simulated using 4th order Runge-Kutta numerical methods. Here, as the input voltage increases the vibration amplitude x rises steadily until it matches the 80nm gap spacing, at which point the disk impacts the switch axis (output) electrode.

From Figure 2-8, the bandwidth over which impacting occurs is controllable via the amplitude of the ac input voltage. In effect, the larger the input voltage amplitude, the lower the frequency of first limiting on the frequency characteristic of the device, and the higher the frequency of last limiting. This band-width-widening is a nonlinear dynamical effect that provides simultaneous high-Q and wide bandwidth—something not generally available in purely linear systems, where high Q often means small bandwidth. In particular, nonlinear resonance dynamics provides on the one hand high Q along the input axis, which lowers the required input ac voltage; while also providing on the other hand a wide effective bandwidth along the switch (or output) axis. The availability of simultaneous high-Q and wider-than-linear bandwidth obviously benefits the aforementioned filter-LNA application, where a finite receive channel bandwidth must be received. It also ben-
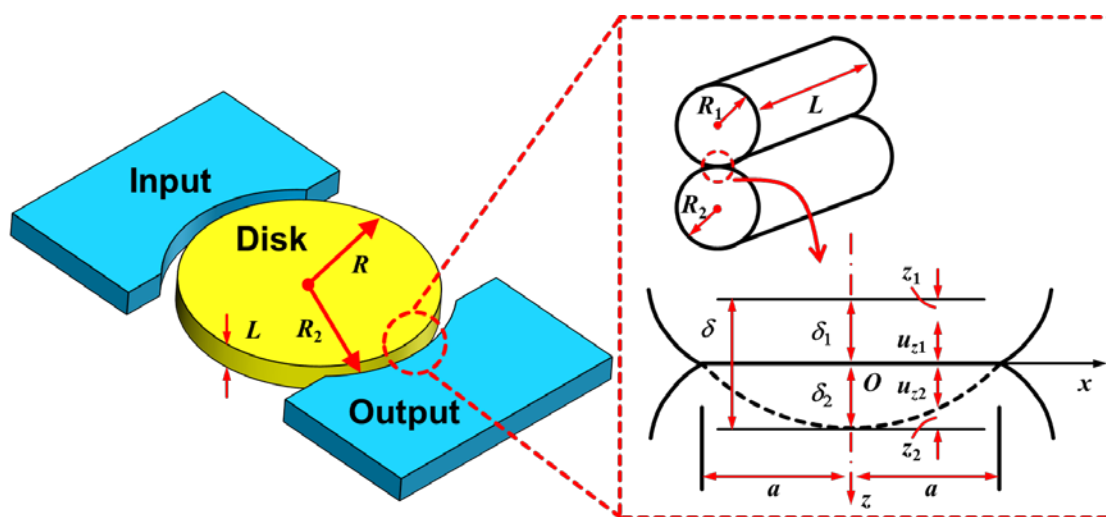
Figure 2-9: Model of a wine-glass disk resoswitch contact as two-dimensional contact of cylindrical bodies with parallel axes.

efits transmit power amplifier applications in communications, since it permits wide frequency modulations on the transmitted signal while simultaneously lowering the input capacitance needed to operate the device with a given input signal amplitude.

Having much higher resonance frequencies and quality factors than the clamped-clamped beam ones, the impulsive contact forces achievable by the wine-glass disk resoswitch are expected to be larger and this can also be verified by the Hertz theory. For wine-glass disk resoswitch, one appropriate Hertz model to be used is "two-dimensional contact for cylindrical bodies" as illustrated in Figure 2-9. The left part of Figure 2-9 is the schematic of a disk switch consisting of a disk with radius R hitting an electrode with inner side of a cylindrical surface of radius R_2. This kind of contact can be simplified as the contact of two cylindrical bodies with parallel axes. Two things need to be taken care of before expanding the detailed analysis. First, at the moment of impact the disk deforms from the circular shape to an ellipse, thus R_1 is the local radius at the vertex of the major axis of the elliptical disk. Second, since output electrode is of concave shape instead of convex as shown in top right, R_2 needs to have negative sign in the following derivations.

The right part of Figure 2-9 is a zoom in to the contact area, where contact width is still assumed to be $2a$ and is symmetric about the Oz axis. If the solids did not deform, their profiles would overlap as shown by the dotted lines. The maximum deformation δ, happening at the very center, equates to the sum of δ_1 and δ_2 which stands for the deformations of each body, respectively. Deformation of other points within contact area is a function of coordinate x and can be written as:

$$u_z(x) = u_{z1}(x) + u_{z2}(x) = \delta - \frac{x^2}{2R} \tag{2.13}$$

where R is the relative curvature of the contact defined as:

$$\frac{1}{R} = \frac{1}{R_1} + \frac{1}{R_2} \tag{2.14}$$

According to Hertz theory, given contact loading F, the contact semi width a can be calculated by

$$a = \left(\frac{4FR}{\pi L E^*}\right)^{1/2} \tag{2.15}$$

$$a = (R\delta)^{1/2}$$

where L is the lengths of the cylinders, i.e. the thickness of the disk and the electrode and E^* is the same contact modulus defined in (2.10). Combining the relationship between a and δ as also shown above, the equivalent contact stiffness $k_{contact}$ can then be written as:

$$k_{contact} = \frac{F}{\delta} = \frac{\pi E^* L}{4} \tag{2.16}$$

Figure 2-10 plots the simulated transient disk displacement and contact force using (2.6) with $k_{contact}$ defined in (2.16) when ac driving signal's frequency is within the impacting flat band of the spectrum in Figure 2-8. As expected, the contact force is around 25mN at steady state, which is 2-3 orders of magnitude higher than what a conventional RF MEMS switch can normally achieve and yet the driving voltage is only 0.8V. By virtue of this relatively large contact force contact resistances can be substantially reduced. In particular, as will be shown in the next section, contact resistance of resoswitches made of doped polysilicon goes down from values insufficient to implement ohmic contact [31] [36] to less than 2kΩ.
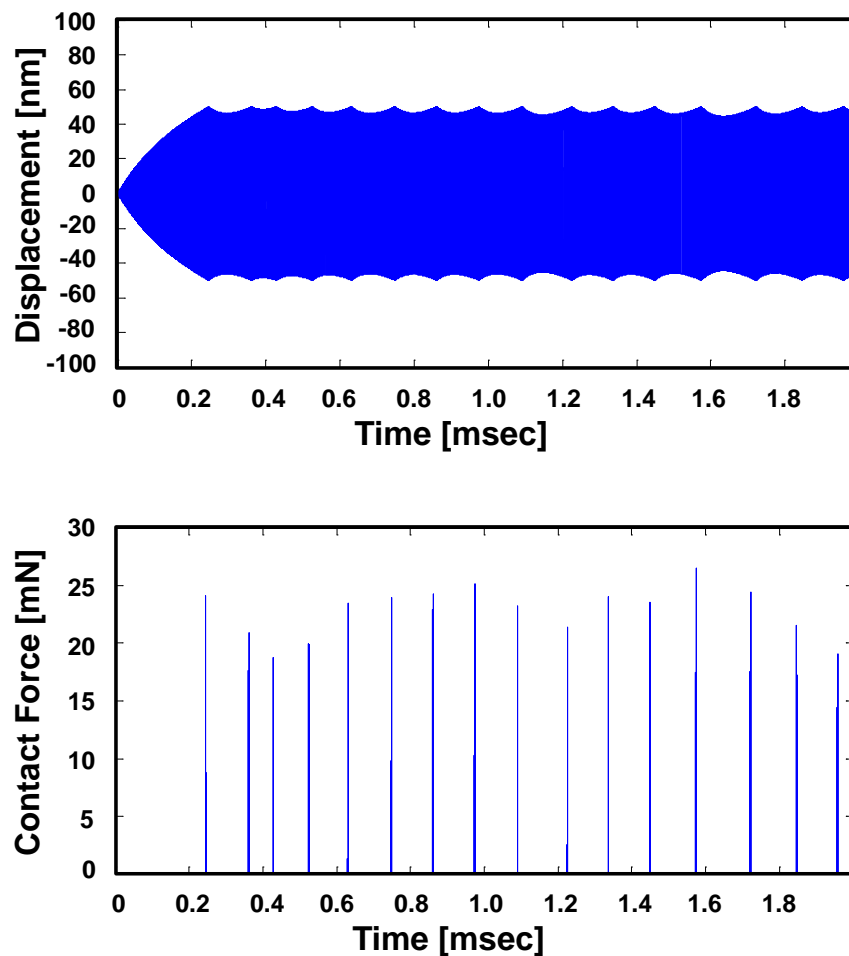
Figure 2-10: MATLAB simulated displacement and contact force of the 61MHz wine-glass mode disk resoswitch assuming $V_{in} = 0.8$V is applied.

2.2.2 Measurement Results

Figure 2-11(a) presents the SEM of one of a 61-MHz wineglass disk resoswitch fabricated via the process in [33], with a zoom-in shot in (b) showing the tiny gap between the disk and its switch electrode along the switch axis.

Again, for most power amplifier and converter applications, the resoswitch should be constructed of metal, not polysilicon, to reduce its contact and series resistance. The use of doped polysilicon in this work does compromise resoswitch performance, especially with regards to the switch "on" resistance. Nevertheless, it still allows demonstration of practically all other important resoswitch performance parameters. It should be noted that,

f_o = 61MHz
V_P= 10V
Q = 120,000
k = 1.15x10^6 N/m

(a)   (b)
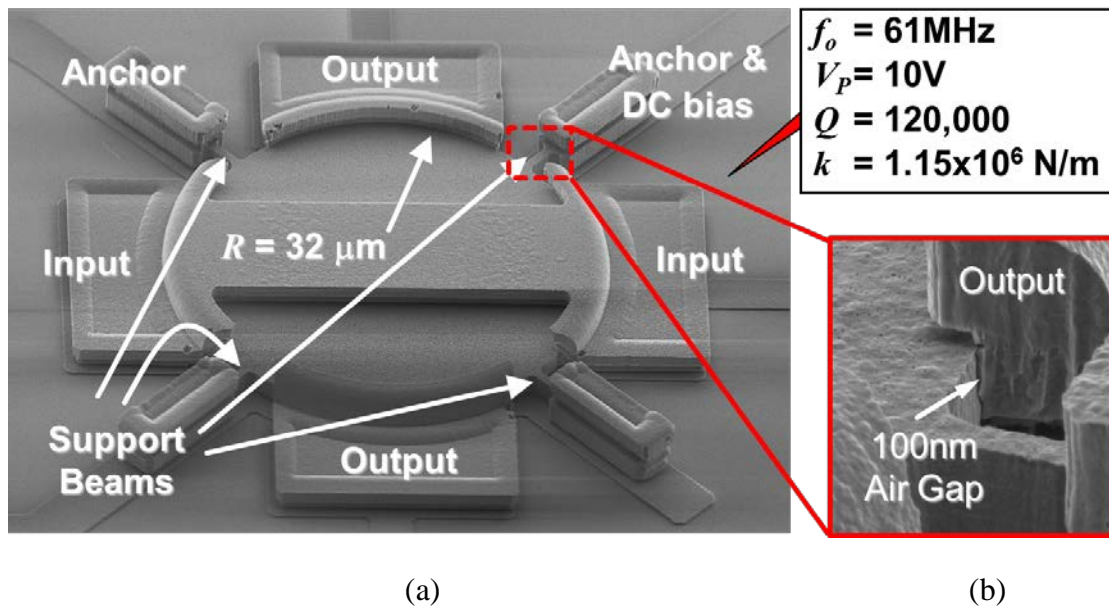
Figure 2-11: (a) SEM of the polysilicon wine-glass disk resoswitch with properly spaced and positioned electrodes; and (b) zoom-in on the electrode-to-resonator gap of the device along the switch axis.

despite its high series resistance, the polysilicon version of the resoswitch is actually still quite applicable for use in low current drain switched-mode on-chip dc-to-dc power converters (i.e., charge pumps), such as needed to supply the large dc-bias voltages often required by vibrating resonators and RF MEMS devices [8] [32] [33] [34].

For simplicity in this early demonstration, the strategy of using different electrode-to-disk spacings along the input and switch axes shown in Figure 2-6 was not used in this implementation. Rather, the electrode-to-resonator gap spacings for both axes were 100 nm for direct contact switches, in which the conductive disk and electrode materials actually make electrical contact; and about 97 nm for capacitive switches, in which a thin layer of oxide exists over conductive surfaces that prevents electrical contact, but still allows switching through the large capacitance that results when the disk impacts its switch electrodes. For the direct contact version of the resoswitch, one obvious consequence of the use of identical input and switch axis electrode-to-resonator gaps is that the input gets shorted to the disk during operation, which then complicates use of the resoswitch in actual applications. (For example, the Class-E power amplifier topology later shown in Figure 2-17 would not be permissible under these conditions.)

To deal with input shorting, the test set-up used to measure resoswitch performance, depicted in Figure 2-12, uses a less practical configuration, but one still valid for evaluation of switch performance. Here, a dc-bias voltage V_P is applied to the disk structure that
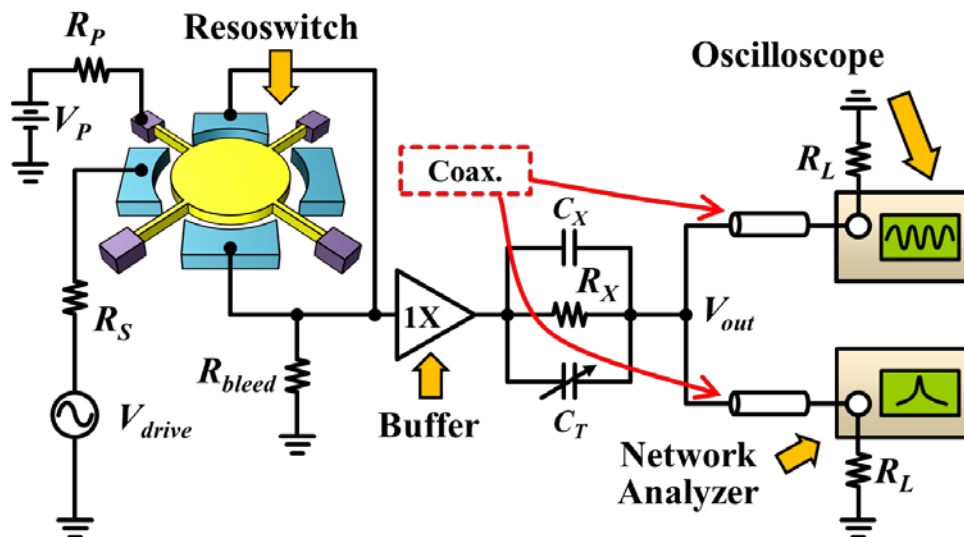
Figure 2-12: Test set-up used to evaluate the 61MHz wine-glass disk resoswitch.

is effectively applied to the output node when the switch closes (i.e., comes "on") in the fashion shown in Figure 2-7. As shown, this circuit allows both time domain (i.e., oscilloscope) and frequency domain (i.e., network analyzer) observation of the resoswitch output. The output buffer used in this circuit effectively removes the 80pF of coaxial capacitance that would otherwise load the output node of the resoswitch and greatly reduce the signal level due to 3dB bandwidth roll-off. The output buffer, however, is not perfect, as it still loads the output node of the resoswitch with about 4pF. This is large enough to filter out the higher order harmonics of the expected output waveform so that it looks more sinusoidal.

Figure 2-13 and Figure 2-14 present the oscilloscope waveform and swept frequency response spectrum (for various input amplitudes), respectively, of the direct contact resoswitch, verifying switching operation, impact limiting, and also the band-width-widening effect previously discussed. Switching clearly occurs when the frequency response grows suddenly and limits with a "flat top", as shown on Figure 2-14. This occurs when the voltage amplitude reaches 2.5V. The measured output signal in Figure 2-13 has a peak-to-peak amplitude of about 1V, which is the value expected when considering attenuation via the finite 3dB bandwidth of the measurement circuit of Figure 2-12, and when considering the voltage divider formed by the parasitic polysilicon interconnect resistance R_p and the bleed resistor R_{bleed}. The signal is not quite a square wave due to bandwidth limitations of the measurement circuit, but the amplitude is correct. To emphasize this point, Figure 2-13 also includes a SPICE simulated waveform that includes the effects of 1.1kΩ of parasitic resistance R_p and 3.5pF of buffer input capacitance, and that clearly resembles the measured waveform.
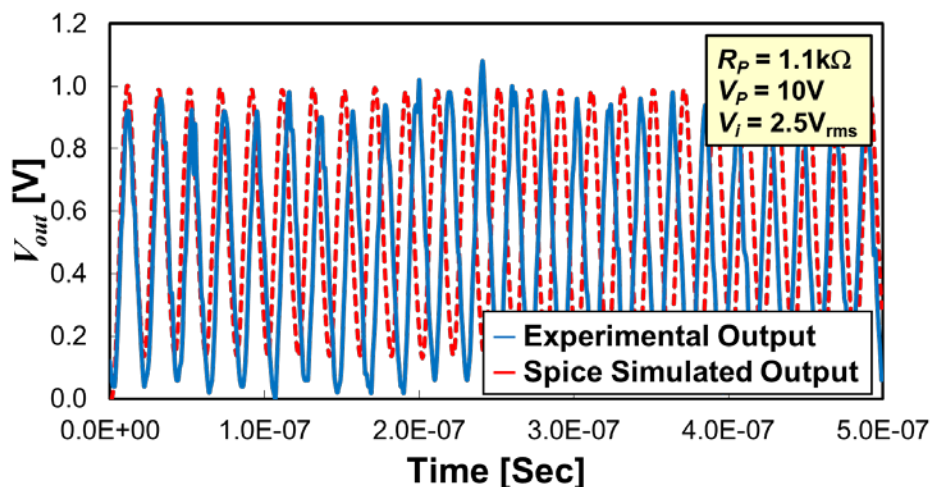
Figure 2-13: Oscilloscope (i.e., time domain) waveform and SPICE simulated prediction seen at the resoswitch output node of Figure 2-12 when driven by a resonance input signal with 2.5V amplitude.
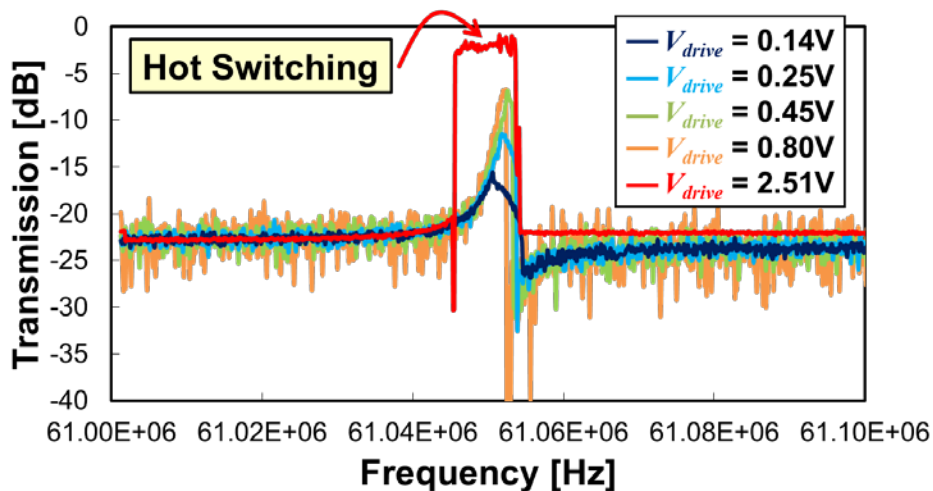
Figure 2-14: Frequency response (in vacuum) as measured by a network analyzer of the direct contact version of the resoswitch for varying resonance input ac voltage amplitudes.

Figure 2-15 presents a measured plot of output power (seen at the switch axis output node) versus frequency. Here, the buffer of Figure 2-12 was not used, so load-induced attenuation somewhat compromised the measurement, resulting in a measured output power considerably lower than in Figure 2-14. Nevertheless, Figure 2-15 does verify the
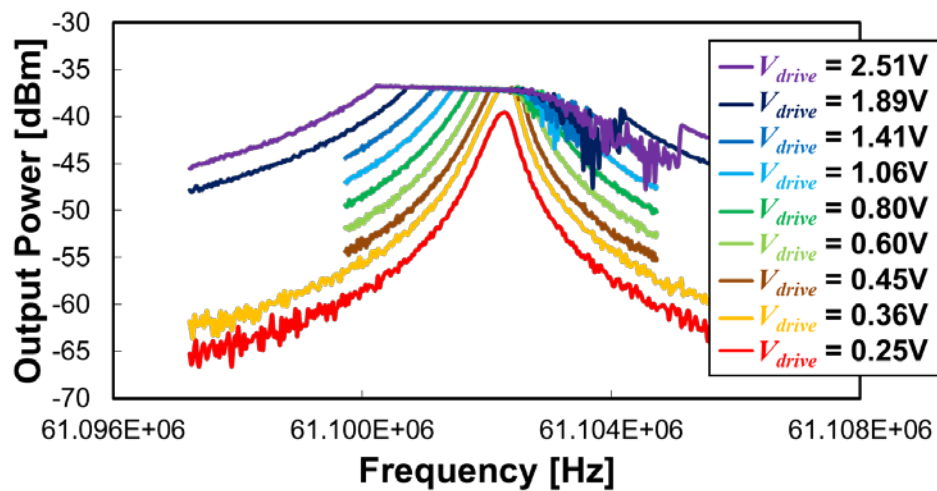
Figure 2-15: Measured output signal power versus frequency for the capacitive version of the resoswitch. Here, the output power clearly limits when the disk impacts the switch electrode.
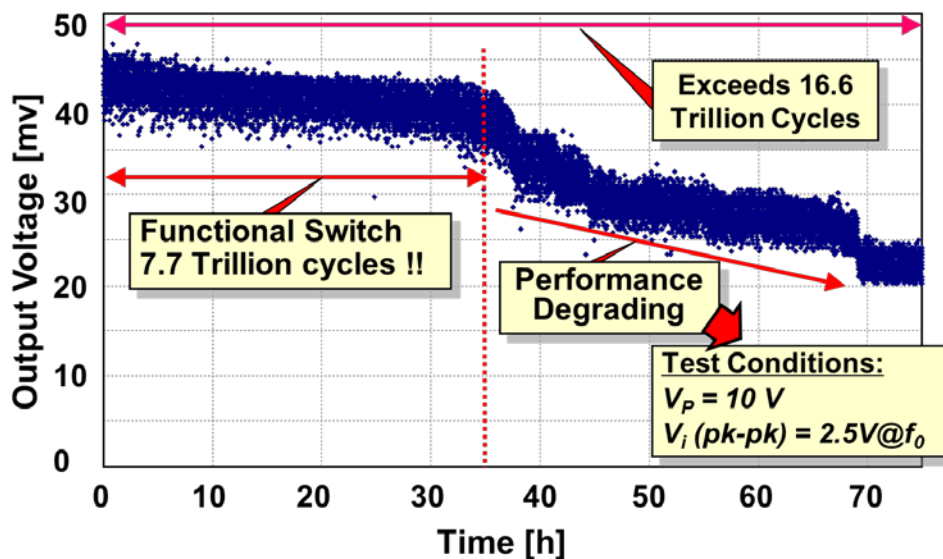
Figure 2-16: Lifetime test of the 61MHz wine-glass polysilicon disk resoswitch.

nonlinear resonance dynamical behavior of the resoswitch, since the bandwidth does indeed widen as the input voltage amplitude increases.

To evaluate reliability at low power levels, the resoswitch was operated continuously with $V_P = 10$V for 75 hours (~3 days or 16.5 trillion cycles) without failure at a frequency

of 61 MHz [37], which is a frequency in the flat region of Figure 2-14, and thus, a frequency where impacting occurs. Figure 2-16 presents a plot of output amplitude versus time for the polysilicon version of the resoswitch. Although no failure was observed, degradation was seen, where after about 1.5 days, the output voltage began to decrease significantly. Although 1.5 days corresponds to 7.7 trillion cycles at 61 MHz, which is more than two orders of magnitude higher than the 100 billion cycles typically achieved by (good) RF MEMS switches, there is still cause for concern, here, since typical switched-mode power applications will require quadrillions of cycles. More study into the degradation mechanism is needed, but one possible reason for the observed degradation could be the growth of a thicker oxide or other dielectric on the switch contact interfaces. In the future, resoswitches constructed of metal with engineered contact surfaces, probably having noble metal coated over the contacts, will be investigated.

2.3 Conclusions

In this chapter, the resonance and nonlinear dynamical properties of a micromechanical wine-glass disk have been harnessed to demonstrate an impacting micromechanical switch with substantially higher switching speed, better reliability (even under hot switching), and lower actuation voltage, all by substantial factors, over existing RF MEMS switches. Although next generation versions of this resoswitch constructed in metal material [38] should be more widely applicable, the present polysilicon version can still find application to low current drain applications, such as Dickson's charge pumps [20], where replacement of diodes with resoswitches should allow a very high output voltage, suitable for dc-biasing of capacitively transduced micromechanical resonators.

Perhaps the best way to gauge the benefits of the described resoswitch is by comparison with other switches. To this end, Table 2-4 compares the described micromechanical resoswitches with transistor FET and RF MEMS switch counterparts, showing clear advantages in maximum supply voltage and input capacitance over transistor FET's, and in actuation volt-age and speed over RF MEMS switches, and more importantly, the nickel resoswitch finally bests the semiconductor by orders of magnitude in *FOM*, which is the main parameter that governs performance in power amplifiers and converters.

Although the device-to-device comparisons are already favorable for the resoswitch, the advantages provided by the resoswitch are perhaps best elucidated in the context of an application. To this end, Figure 2-17 shows the circuit topology of (a) a conventional Class-E power amplifier (PA) using a transistor switch device; and (b) one simplified rendition of the same amplifier utilizing the vibrating micromechanical resonant switch demonstrated in this work. The use of a micromechanical resoswitch in place of the switching transistor in this application stands to enhance performance as follows:

1) It allows the use of much higher voltages (e.g., 10V vs. the 1-3V limit of conventional CMOS) [25]. This then allows the resoswitch rendition to directly drive the 50Ω load, and thereby dispense with the lossy matching network needed by the transistor ver-

Table 2-4: Comparison of Switch Technologies.

Parameter	FET	Conventional MEMS	PolySi Resoswitch	Units
Actuation Voltage	1-3	20-80	2.5	V
Switching time	$0.16\text{-}1\times10^{-9}$	$1\text{-}300\times10^{-3}$	$\sim4\times10^{-9}$	sec.
Life time	Very large	100 Billion	16.6 Trillion	cycles
Off State Power	0.2-3μ [81]	0	0	W
On Resistance R_{ON}	0.5 [81]	0.1-1 [82]	~1100	Ω
Input Capacitance	$\sim20\times10^{-12}$ [10]	$1\text{-}10\times10^{-15}$ [82]	18×10^{-15}	F
$FOM=1/(2\pi R_{ON}C_{off})$	590G	63T	8G	Hz
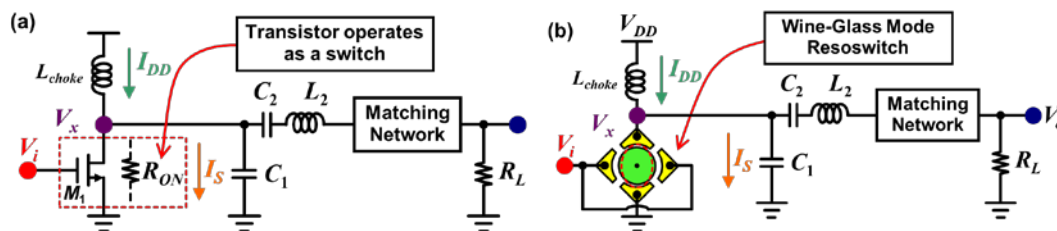
Figure 2-17: Circuit topologies of (a) a conventional Class-E amplifier using a transistor switch device; and (b) one simplified rendition of the proposed Class-E amplifier utilizing the described vibrating micromechanical resonator switch.

sion. Removal of the matching network and raising the driven impedance from 2Ω to 50Ω can raise the efficiency of a Class-E power amplifier by as much as 23%.

   2) The use of the resoswitch further allows the same or smaller "on" resistance than its FET counterpart, but with substantially smaller input capacitance, e.g., only 20fF for the resoswitch versus 20pF for a CMOS PA switch—a 1000× difference that removes much of the input power that would otherwise be needed to drive the PA. Again, better efficiency ensues.

   Again, the benefits summarized here ensue only when the resoswitch is implemented in a metal structural material. Work towards more reliable metal resoswitches will be discussed in the next chapter.

CHAPTER 3 *Nickel Resoswitches for On-Chip Power Applications*

A micromechanical resonant switch, or "resoswitch" (*c.f.*, Figure 3-1), constructed in nickel metal rather than previously used polysilicon attains a switch *FOM* >50THz, which is several times higher than so far attained by power FET devices and pin diodes. Here, the use of metal reduces the "on" resistance of the resoswitch to less than 1Ω, allowing it to generate 17.7dB of sustained electrical power gain at 25MHz when embedded in a simple switched-mode power amplifier circuit, marking the first successful demonstration of RF power gain using a micromechanical resonant switching device. The high *FOM* of this device may soon permit the near 100% efficiency predicted for Class-E switched-mode power amplifiers that has eluded transistor-based versions for decades. This in turn would greatly extend battery lifetimes for portable wireless communications and other applications.

Although improvements in transistor performance have certainly transformed the capabilities of digital circuits over the past few decades, they have had a much more measured effect on analog circuits. Indeed, in wireless circuits, the power amplifier (PA) remains a primary obstacle against longer battery lifetime, since PA efficiency over the years has improved relatively slowly. Among PA topologies, switched-mode ones like Class-E can theoretically achieve 100% drain efficiency, provided the switches used have sufficiently high figure of merit [$FOM = 1/(2\pi R_{on}C_{off})$, where R_{on} is on resistance, C_{off} is off capacitance]. Unfortunately, CMOS so far offers switch *FOM*'s less than 600GHz [39] with reasonable breakdown voltages; and even the GaAs HBT's commonly used in PA's only muster 3THz [40]. On the other hand, RF MEMS switches [8] attain much higher *FOM* >60THz, so would be ideal for PA's if not plagued by issues like low switching speed, large actuation voltage, and poor reliability.

Pursuant to circumventing these issues, the micromechanical resonant switch ("resoswitch") introduced in previous chapter harnesses the resonance and nonlinear dynamical properties of its mechanical structure to greatly increase switching speed and cycle count (even under hot switching), and lower the needed actuation voltage, all by substantial factors over existing RF MEMS switches, making it suitable for high efficiency
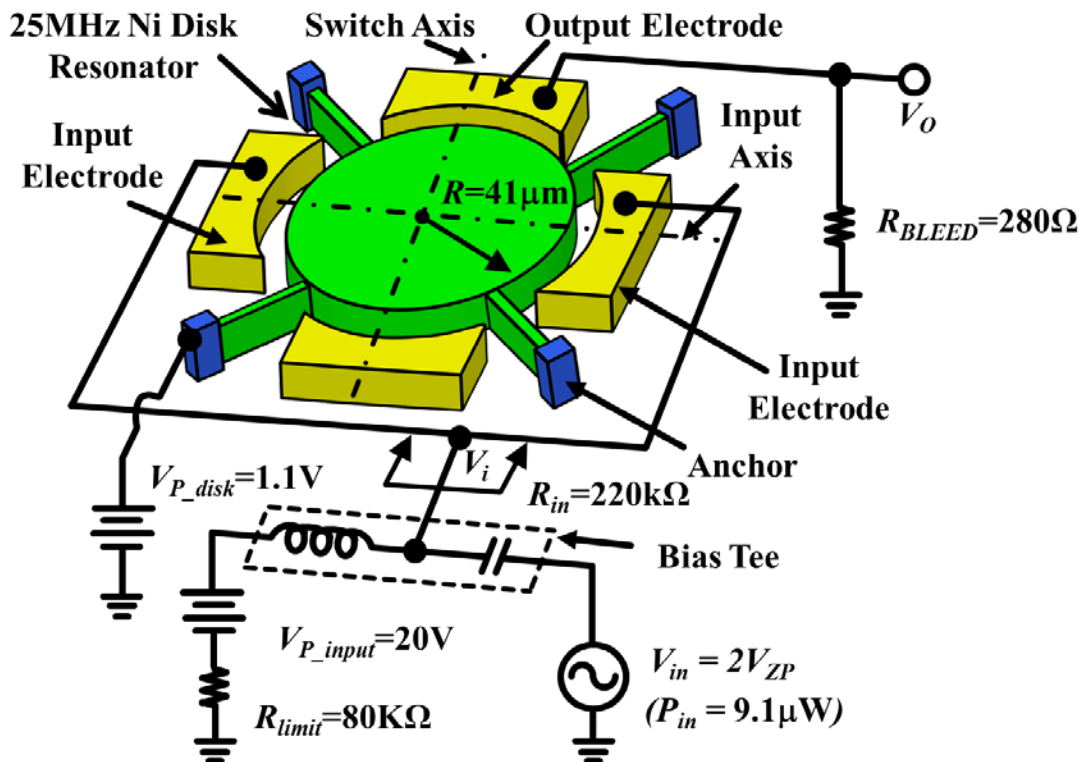
Figure 3-1: Schematic of the micromechanical resonant switch in a simple switched-mode power amplifier circuit.

power amplifier applications. The switch of [37], however, was constructed in doped polysilicon, which compromised its ability to achieve power gain, since its high series and contact resistances loaded down its *FOM*. This work overcomes the problem by constructing the resoswitch in nickel metal to attain a switch *FOM* greater than 50 THz, which is several times higher than so far attained by power FET devices and pin diodes [41]. Here, the use of metal reduces the "on" resistance of the resoswitch to less than 1Ω, allowing it to generate 17.7dB of sustained electrical power gain at 25 MHz when embedded into the simple switched-mode PA circuit of Figure 3-1, marking the first successful demonstration of RF power gain using a micromechanical resonant switch.

3.1 Device Structure and Operation

Figure 3-1 presents a schematic of the metal resoswitch in the simple circuit used to demonstrate switched-mode power gain. As shown, the device consists of a 41μm-radius Ni disk designed to mechanically vibrate at 25 MHz in the wine-glass mode shape shown in Figure 3-2, where the disk expands and contracts along orthogonal axes. The disk is suspended 700 nm above a NiTi/Ni metal ground plane (attached to the substrate) by four support beams located at nodes in the mode shape to minimize energy loss to the sub-
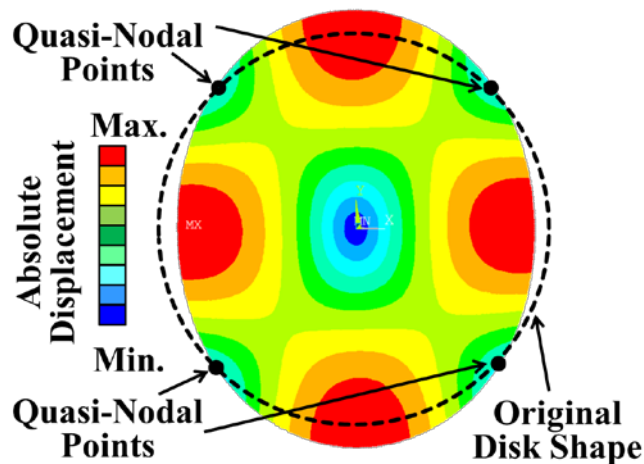
Figure 3-2: Finite element simulated wine-glass disk mode shape, in which the disk expands and contracts along orthogonal axes.

strate. Ni electrodes surround the disk, spaced 120 nm from its edges along the input axis, i.e., along the axis where the input drive signal is applied; and 80 nm along the orthogonal switching axis, i.e., the axis along which the disk contacts the output electrodes.

A 2V zero-to-peak sinusoid near the disk resonance frequency applied to the input electrodes is sufficient to drive the disk so that it impacts the electrodes along the switch axis, but not along the larger gapped input axis, as shown in Figure 3-3. Periodic switching thus ensues as vibration of the disk opens and closes the contact with a period and duty cycle set by the frequency and amplitude of the input signal.

Operation at resonance provides many advantages over non-resonant switches. In particular, because resonance operation effectively multiplies the displacement amplitude by the system Q, which can be in the thousands, a resoswitch can be designed with a much larger stiffness on the order of 1.6×10^6N/m, compared with the 50 N/m of a typical conventional MEMS switch, while also reducing the actuation voltage to a more reasonable value. The large stiffness of a resoswitch in turn allows it to operate at much higher frequency than a conventional MEMS switch while simultaneously improving reliability, since the higher stiffness now generates a much larger force with which to overcome stiction forces. In addition to these benefits, impacting operation actually expands the bandwidth of the resonant switch, as shown in Figure 2-15, allowing the device to amplify over a bandwidth much larger than that of a non-impacting resonator. In fact, as the peak flattens it spreads out over a larger bandwidth. Effectively, the amplifying bandwidth of the resoswitch is a function of the drive voltage, so can be controlled at will.

Of course, operation at resonance constrains this switch to applications that require periodic switching, which makes it unsuitable for digital logic or antenna switching. For-
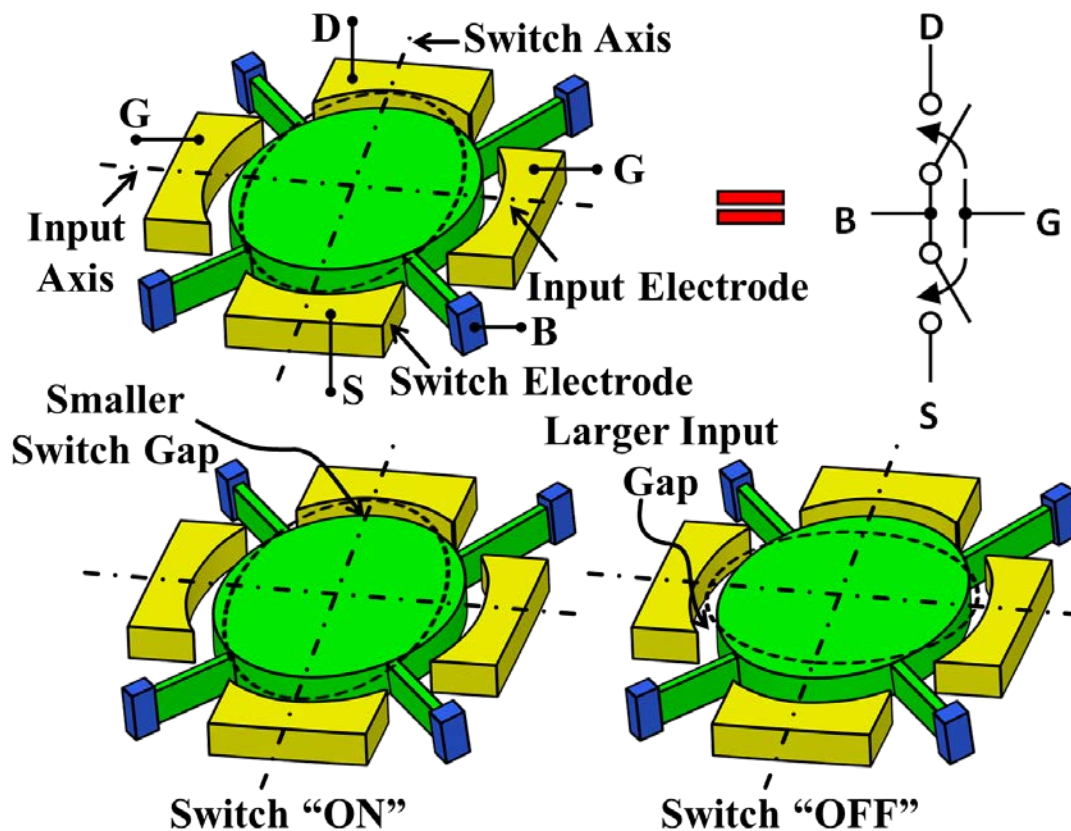
Figure 3-3: Schematic depicting impacting in the wine-glass mode resoswitch along the switch axis, but not along the input axis.

tunately, the majority of power applications, e.g., power amplifiers and power converters, require periodic switching, and these applications are arguably much more lucrative, since it is in these where existing on-chip devices are most lacking.

3.2 Fabrication Process

Pursuant to confirming the benefits of resonance operation, plus demonstrate power gain, Figure 3-4 presents the process flow used to fabricate nickel metal resoswitches with the design of Figure 3-1. The process begins with successive LPCVD depositions of SiO_2 and low stress Si_xN_y at $450^{\circ}C$ and $835^{\circ}C$, respectively, to provide electrical isolation from the conductive silicon substrate. (Note that these layers are not needed when fabricating above CMOS.) Successive films of 5 nm of NiTi alloy adhesion layer and 100 nm of Ni are then sputtered and patterned via liftoff to form electrical interconnects as shown in Figure 3-4(1). Next, 700 nm of TiW is blanket sputter deposited to serve as a bottom sacrificial layer that temporarily supports structures to be released later. Anchor vias are
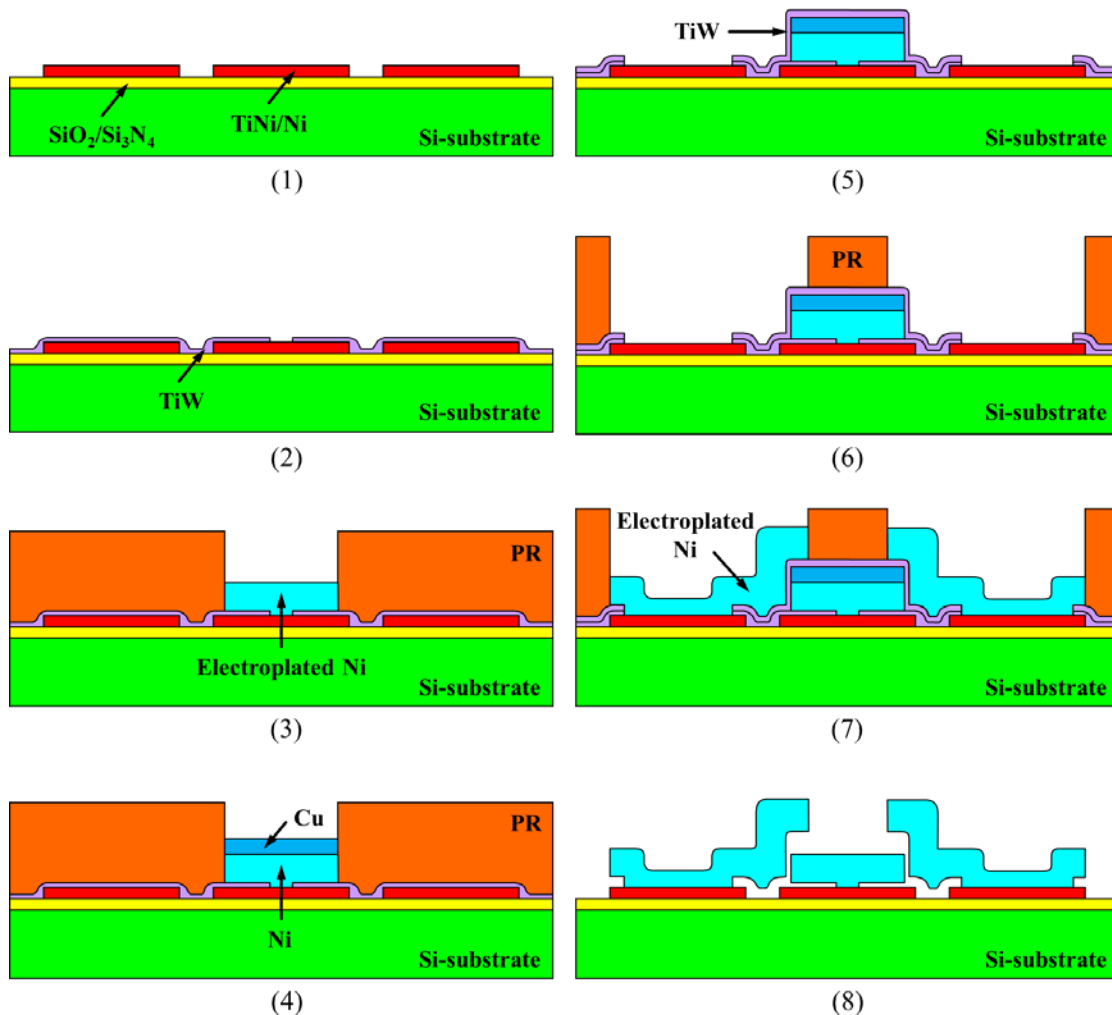
Figure 3-4: Surface-micromachining fabrication process for the nickel resoswitch.

then plasma etched into the TiW using an SF_6+O_2 chemistry, yielding Figure 3-4(2), followed by O_2 plasma cleaning of residues formed during dry etching to improve structure-to-interconnect contact, both electrical conductivity and mechanical strength. Next, the Ni structural layer is electroplated 3μm-thick into the open spaces of a 6μm photoresist mold defining the resonator disks and support beams as shown in Figure 3-4(3). Cu is then electroplated using the same mold to yield Figure 3-4(4) and to serve as a capping layer over all structures that separates the eventual electrodes from the tops of the disks.

A second film of TiW, this time 80 or 120 nm-thick (depending on direction), is blanket sputter deposited to serve as a sidewall sacrificial layer that defines the gap spacing between the electrodes and the resonator disk. This sputtering step is surprisingly conformal over the sides of the disks, but fortuitously, not completely isotropic. In partic-
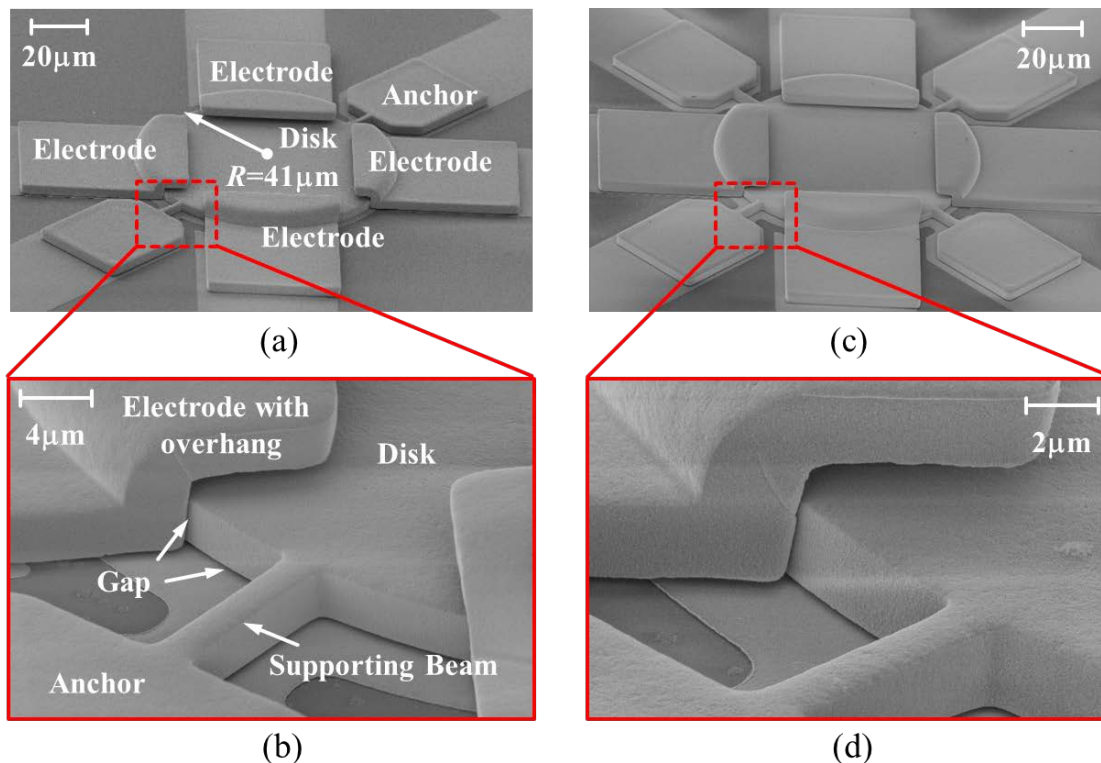
Figure 3-5: SEM's of a 25-MHz wine-glass mode electroplated-nickel disk resonant switches with (a) two and (c) four supporting beams, and (b) and (d).zoom in on an anchor and on the electrode-to-disk gap of both devices, respectively.

ular, proper orientation of the wafer in the sputtering chamber permitted deposition of different thicknesses along the different axes of the disk, allowing this process to realize the unequal input and switch axis electrode-to-resonator gaps needed for proper switch operation [42] [43]. After the gap-defining deposition, anchors for the electrodes are patterned and etched into the total TiW layer, and electrodes surrounding the disk are electroplated through a 2nd photoresist mold to yield Figure 3-4(6). Finally, the TiW sacrificial layer is removed via a $NH_4(OH)+H_2O_2$ wet etch in the very last step of the process to free devices and yield Figure 3-4(8).

Figure 3-5 presents the SEM of a 25-MHz nickel disk resoswitch resulting from this process, with a zoom in on a support beam that also includes one of the tiny disk-to-electrode gaps. Since temperatures (after the isolation layers, which aren't needed when fabricating over CMOS) never exceed $100^{o}C$, the process of Figure 3-4 is quite compatible with CMOS, so can potentially enable a single-chip RF transmitter solution, where CMOS up-conversion circuits precede a highly efficient resoswitch-based power amplifier.
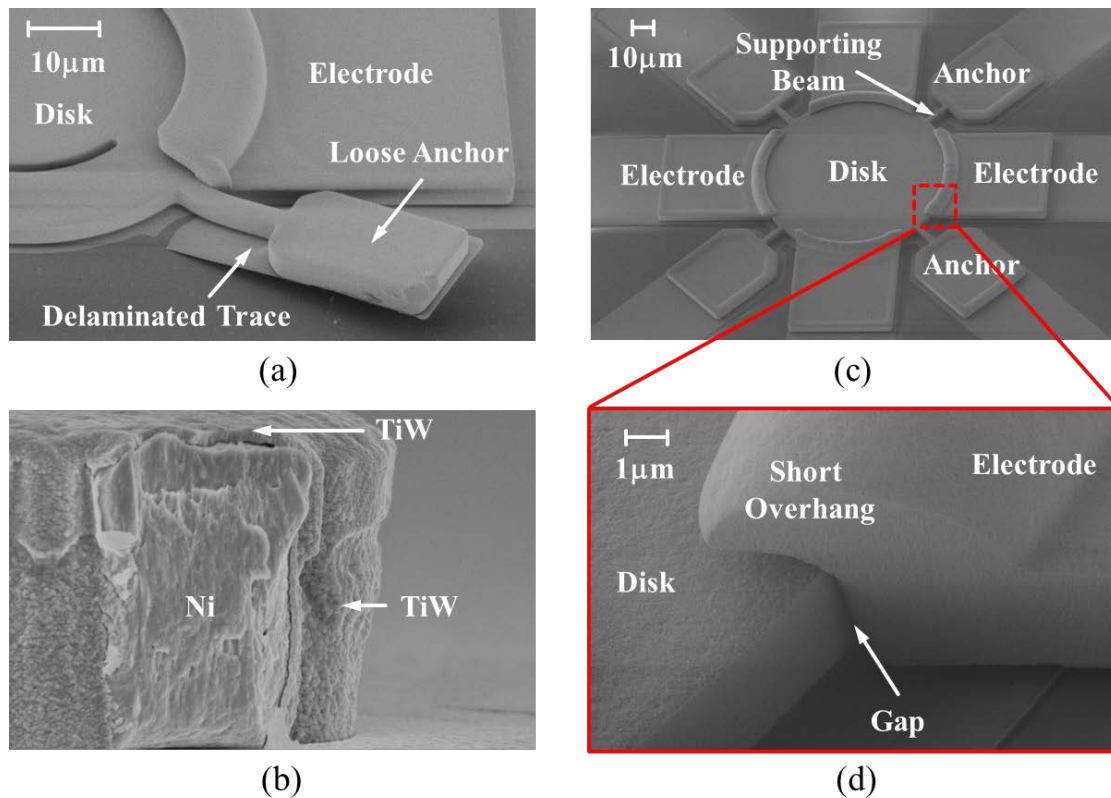
Figure 3-6: SEM's of (a) device with delaminated trace that uses Ti and TiW as adhesion layer and (b) cross-section of a Ni beam covered conformably by sputtered TiW. (c) SEM of a 25MHz wine-glass mode electroplated-nickel disk resonant switch that has shorter overhang using "etch back" process with (d) zoom in on the electrode overhang.

The details of the process flow have been summarized in the Appendix. The process developed here is an improved version compared to that of [44]. Several of the key improvements are list below:

(1) The selection of adhesion layer material and thickness is essential. Three types of materials, sputtered Ti, TiW and NiTi, have been used and compared, where the first two kinds of materials turned out not being able to sustain the release etchant for the time needed to release the structure and delamination has been observed as shown due to the large undercut. Figure 3-6(a) shows the SEM picture of a delaminated interconnect layer using TiW as bottom adhesion layer after one hour of wet release, which is still not sufficiently long enough to clean all the residues under the disk and in the electrode-to-disk gap. Sputtered NiTi alloy with a thickness of 5nm, however, is quite resistant to $NH_4(OH)+H_2O_2$ and can sustain hours of wet release, sufficient for all the devices.
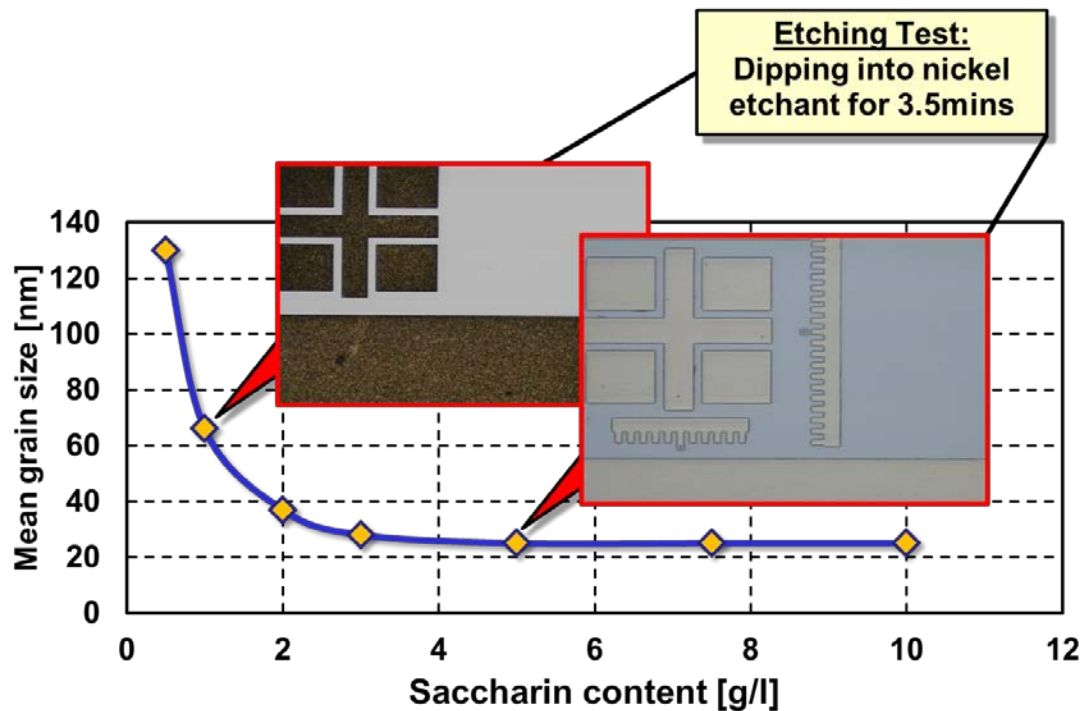
Figure 3-7: Mean grain size of the plated Ni film versus saccharin concentration with etching test results of different samples.

(2) The Cu capping layer electroplated right after plating the structural Ni, which is also etched during wet release, effectively improves the susceptibility of pull-in between the electrode and the disk. The capping layer is essential even when an "etch back" step introduced in [45] is used, because the electroplated electrode can still overflow over the top of disk and form a smaller overhang, as shown in Figure 3-6(c) and (d), that can still cause electrostatic field concentration limiting the maximum DC bias voltage that can be applied to the disk.

(3) Sputtered TiW was used as both bottom and sidewall sacrificial layers. The RF sputtered TiW sidewall is proved to be conformal enough to create 100nm or even smaller gap. Figure 3-6(b) is an SEM photo showing the cross-section of a plated beam with sputtered TiW covering the entire structure, where obviously TiW is conformal along the sidewall although the thickness on the sidewall seems a little thinner than the that on the horizontal surfaces as expected.

(4) Electroplated Ni quality has been optimized through tuning the conditions of the Ni sulfamate based solution, e.g., temperature, PH value, concentrations of chemical additives, etc. Through various trials, saccharine concentration is found be the most crucial factors in determining the quality of the plated film. Figure 3-7
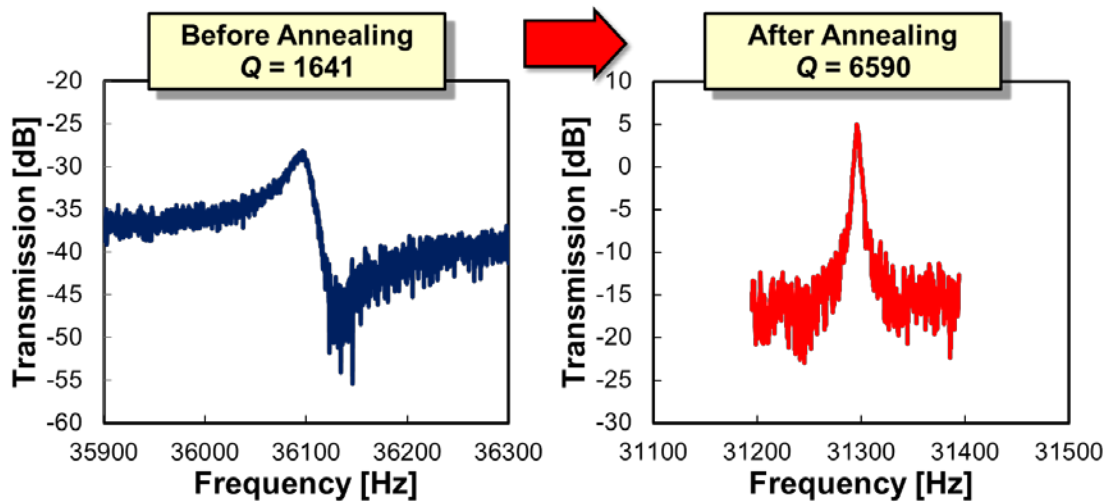
Figure 3-8: Measured spectra of a 36 kHz electroplated Ni comb-driven resonator before and after RTA annealing.

shows the dependence of grain size versus saccharine content, which serves as the brightener of the plating bath and can to some extent reduce the internal stress of the film. As saccharine concentration increases, the mean grain size of the plated film decreases and it saturates when saccharine is more than 3g/l. Smaller grain size is preferred, as it makes the film less vulnerable in the etchants involved thereafter in the process. To examine this, samples plated using baths with different saccharine concentrations are dipped into Ni etchant for 3.5mins and the results show that film plated using bath with 5g/l of saccharine barely gets attacked and remains shining and therefore is substantially better than the 1g/l sample.

(5) Similar to polysilicon devices in [33], post process RTA annealing in H_2 ambient at 400°C for 5mins has also been found to be able to further improve the plated Ni film quality. Figure 3-8 compares the measured spectra of a 36 kHz electroplated Ni comb-driven resonator before and after RTA annealing. Apparently, the quality factor has been boosted by 4× from 1641 to 6590. What is more interesting, samples plated using different current densities are showing different quality factors after annealing, although the quality factors before annealing are nearly the same. Figure 3-9 shows the measured spectra of post RTA annealing Ni comb-drive resonators plated using different current densities, where an obvious increase of Q as the current density decreases has been observed. In particular, when plated with a current density of 2.5mA/cm^2, the quality factor of the device can be as high as 13,500 after annealing, which verifies the feasibility of using electroplated Ni to construct high-Q resonators and resoswitches.
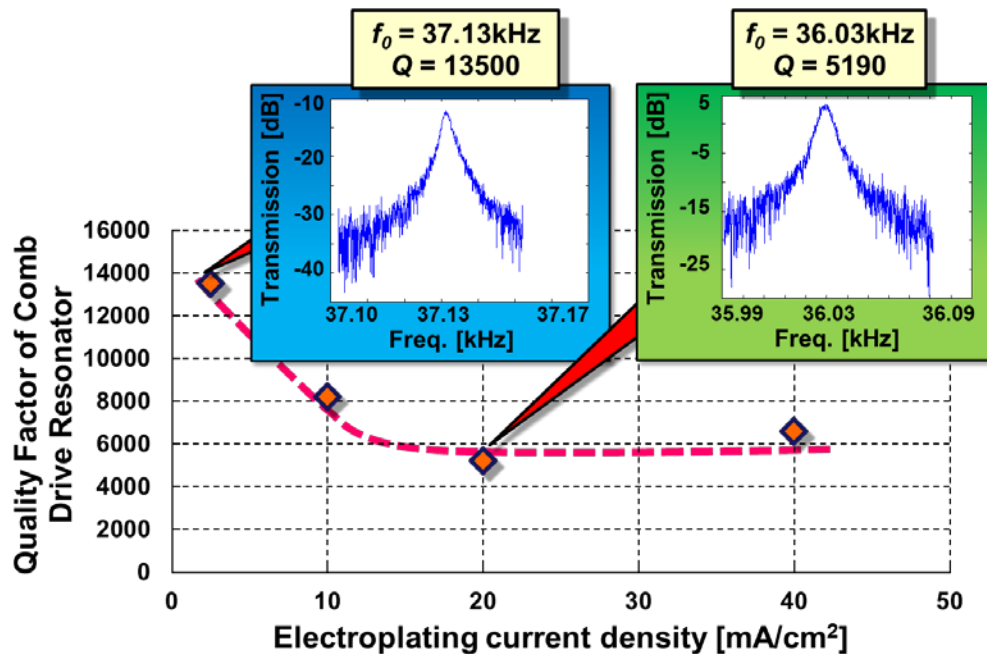
Figure 3-9: *Q*'s of post RTA annealed electroplated Ni comb-drive resonators versus plating current densities.

3.3 Measurement Results

The power gain circuit of Figure 3-1 is very similar in structure to that of an equivalent transistor version shown in Figure 3-10. In the resoswitch version, a dc-bias voltage $V_{P,input}$ (which could also just be dc charge) and an ac voltage v_{in} at resonance combine at the input electrode to generate a force within the resonator passband that drives the disk into vibration with the mode shape of Figure 3-2. When v_{in} is given a zero-to-peak amplitude of 2V, the disk amplitude becomes large enough to impact its electrodes along the switch axis, thereby making electrical contact and transferring power from the $V_{P,disk}$ = 1.1V supply to the output load R_{bleed}.

Figure 3-11 and Figure 3-12 plot the measured input power spectrum (on a network analyzer) and output waveform (on an oscilloscope), respectively, taken at the same time under a vacuum of 25μTorr. Note how the input power peaks at resonance, where the input impedance is minimized. Although the input zero-to-peak voltage amplitude of 2V is larger than the 0.55V at the output node, there is still power gain, since the output impedance is much smaller than the input impedance. In particular, the output impedance is merely the 280Ω load, and the input impedance is 220kΩ, as measured in the S11 plot of Figure 3-13. (3.1) explicitly calculates the power gain to be 17.7dB, which is quite respectable. The input power is 9.1μW, and this is amplified to 0.54μW delivered to the 280Ω output load.
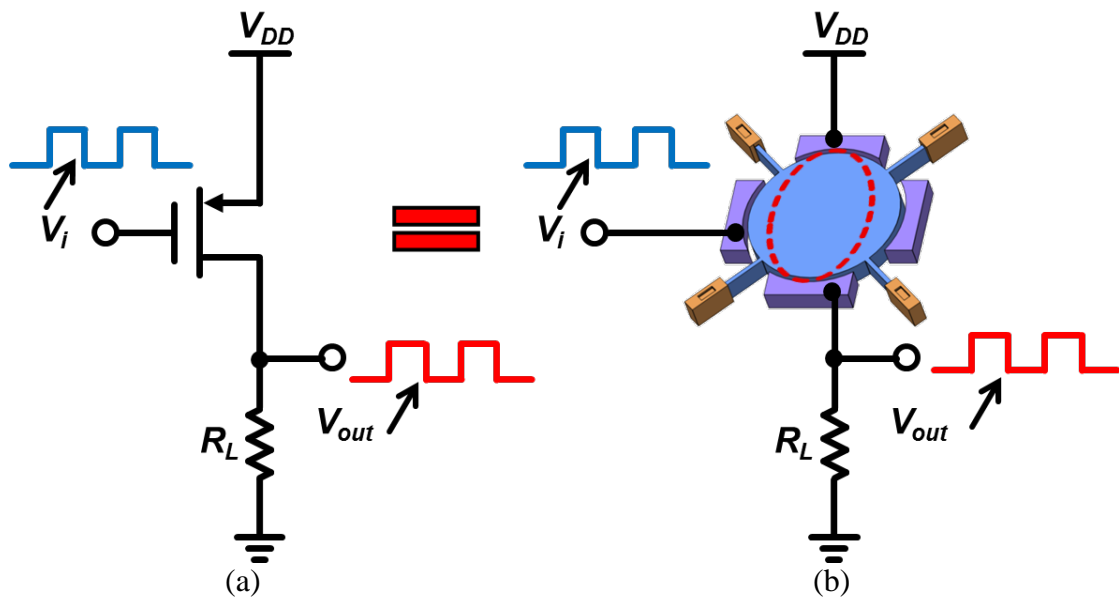
Figure 3-10: Comparison of power gain circuit schematics using (a) a transistor switch; and (b) a micromechanical resoswitch.
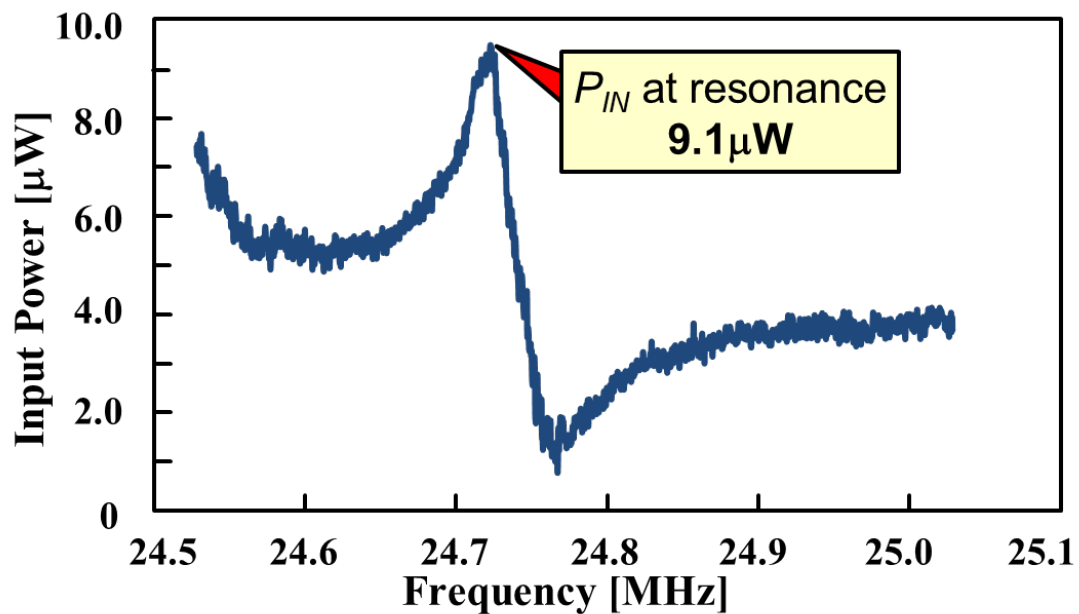
Figure 3-11: Input power as a function of frequency measured by a network analyzer at node V_i in Figure 3-1 and used to determine input impedance.
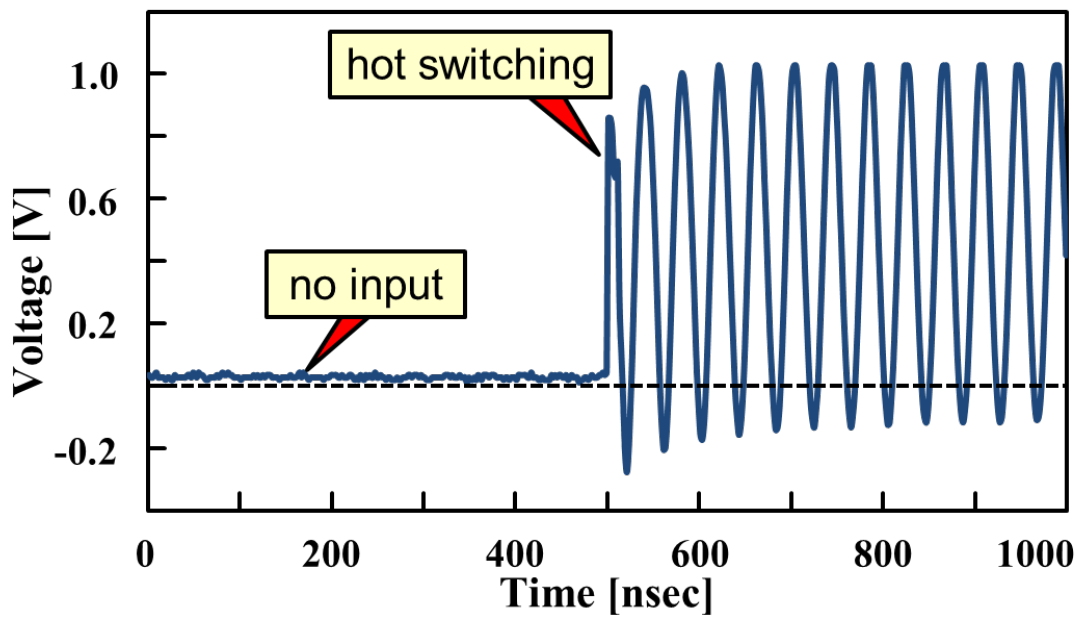
Figure 3-12: Output waveform at node V_o in Figure 3-1, measured using an oscillo-scope.
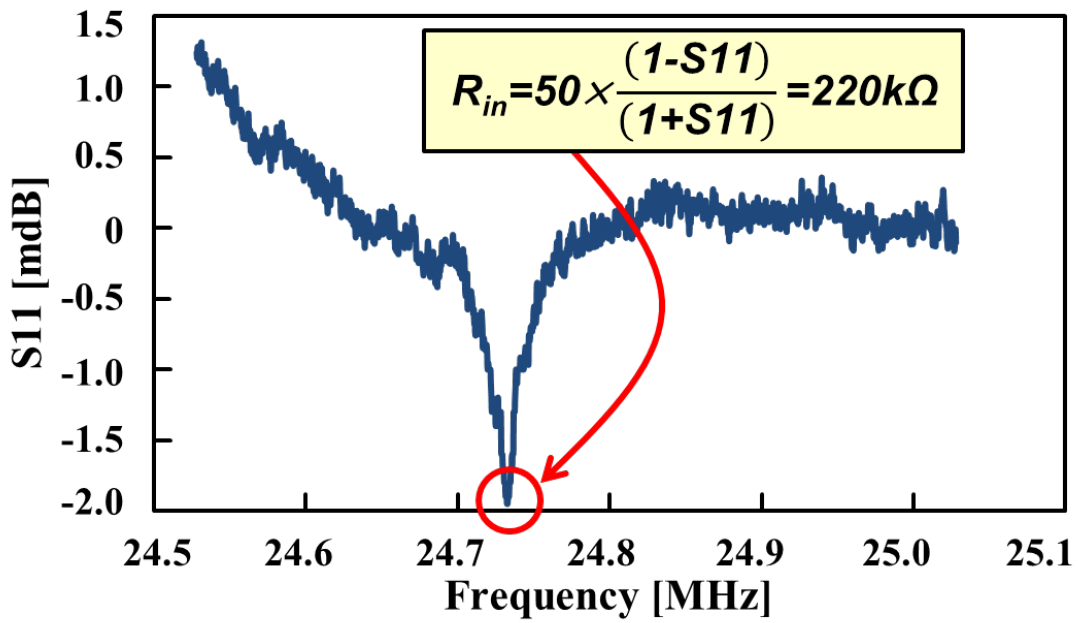
Figure 3-13: Measured S11 used to extract the resoswitch input resistance.

Table 3-1: Comparison of Power Switch Technologies.

Parameter	FET	Conventional MEMS	Nickel Resoswitch	Units
Actuation Voltage	1-3	20-80	2.0	V
Switching time	$0.16\text{-}1\times10^{-9}$	$1\text{-}300\times10^{-3}$	$\sim10\times10^{-9}$	sec.
Life time	Very large	100 Billion	200 Million	cycles
Off State Power	0.2-3μ [81]	0	0	W
On Resistance R_{ON}	0.5 [81]	0.1-1 [82]	~0.5	Ω
Input Capacitance	$\sim20\times10^{-12}$ [10]	$1\text{-}10\times10^{-15}$ [82]	7×10^{-15}	F
$FOM=1/(2\pi R_{ON}C_{off})$	590G	63T	> 50T	Hz

$$V_{in} = 2V_{ZP}, R_{in} = 220k\Omega, P_{in} = \frac{\left(2/\sqrt{2}\right)^2}{220k\Omega} = 9.1\mu W$$

$$V_{out} = 0.55V_{ZP}, R_L = 280\Omega, P_{out} = \frac{\left(0.55/\sqrt{2}\right)^2}{280\Omega} = 540.3\mu W \tag{3.1}$$

$$Power\ Gain = 10log(P_{out}/P_{in}) = 17.7dB$$

The power gain generated by the simple power amplifier circuit of Figure 3-1 comes about mainly due to the small on resistance R_{on} of the metal resoswitch, which at a measured 0.5 Ω is much smaller than the 1.1k Ω of a previous resoswitch made of doped polysilicon material [37]. The small R_{on} combines with a tiny off capacitance C_{off}, estimated at ~7fF, to achieve an impressive *FOM* of 50 THz. Table 3-1 compares the demonstrated metal resoswitch with its MEMS predecessor and with a top semiconductor FET contender [17]. Clearly, the metal resoswitch of this work bests the semiconductor by orders of magnitude in *FOM*, which is the main parameter that governs performance in power amplifiers and converters.

The output waveform shown in Figure 3-12 lasts for 200 million cycles, at which point instabilities pull the device into its electrode [2] (but do not destroy it, as it is actually recoverable). Defensive design to prevent pull-in should be possible in future renditions of this device. For example, instead of creating different disk-to-electrode gaps at input and output, the displacement amplifier designs described in [42] and [43] employing mechanical stiffness engineering to generate larger displacements at the output disk than the input, can prevent input impacting in a more repeatable and effective way. Fur-

thermore, removing electrode overhangs via the etch-back process introduced in [45] increases the dc pull-in voltage, thereby helping to stabilize the device during switching.

3.4 Conclusions

The use in this chapter of a CMOS-compatible process to realize a 25-MHz wineglass disk resoswitch in nickel structural material greatly reduces switch on resistance relative to previous polysilicon versions towards an *FOM* greater than 50 THz and a measured power gain of 17.7dB when emplaced into a simple switch-mode amplifier circuit. The demonstrated power gain, although ample, is not the most efficient possible, since the circuit used to generate it is not Class-E. To realize Class-E operation and perhaps get closer to its theoretical 100% efficiency, energy storage elements, i.e. inductors and capacitors, must be added at proper locations and in proper amounts. Work towards this continues.

CHAPTER 4 *Micromechanical Displacement Amplifier*

A micromechanical displacement amplifier comprising two asymmetric resonator array composites coupled by a quarter-wavelength beam has been demonstrated that permits specification of gain factor by mere (digital) selection of an appropriate ratio of the number of resonators in an input array to that in an output array. Like the method of [43], this displacement gain circuit is a key enabler for resoswitch-based mechanical power amplifiers and power converters, because it can prevent unwanted drive electrode-to-resonator impact in such circuits. This design, however, differs from that of [43] in that 1) it can be applied to radial-contour mode disks that can achieve much higher frequency than the wine-glass disks of [43]; 2) it preserves the frequency and Q of its constituent resonators (whereas the method of [43] changed the frequency and lowered the Q); and 3) its digital method for gain specification is much more straightforward, accurate, and repeatable.

4.1 Micromechanical Displacement Gain Stage

With a figure of merit [8] (*FOM*) potentially much larger than transistor counterparts, the micromechanical resonant switch (dubbed "resoswitch"), introduced in [37] [38] and depicted in Figure 4-1(a), offers the possibility of switched-mode power converters and power amplifiers with substantially better efficiency than presently available. The resoswitch even transcends the capabilities of conventional RF MEMS switches by harnessing resonance and nonlinear dynamical properties to greatly increase switching speed and cycle count (even under hot switching), and lower needed actuation voltages, all by substantial factors. However, as also summarized in Figure 4-1(a)-(c), the resoswitch described in [37] was only a demonstration prototype with several imperfections, one of which was that it impacted (i.e., closed with) not only its output electrodes, but also its input electrodes. This unwanted input closing limits resoswitch performance in certain applications.

To remedy this, the micromechanical resonant displacement gain stage, described in [43] and shown in Figure 4-1(d)-(e), employs stiffness engineering to effect displacement amplification from input axis to output axis. Here, a slotted wine-glass disk is used that allows displacements along the switch axis to be much larger than those along the input
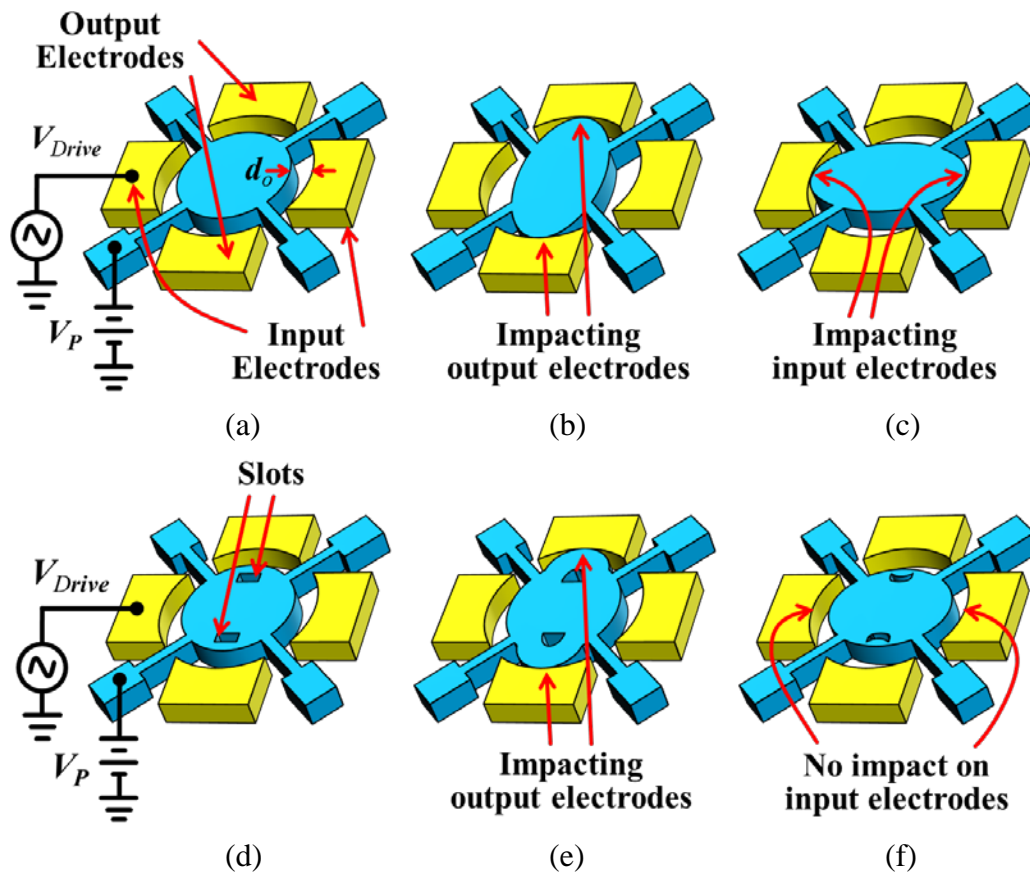
Figure 4-1: Micromechanical resoswitch of the (a) unslotted wine-glass disk version in [37] showing impact along (b) output and (c) drive axes; and (d) the slotted version of [43] impacting only along the (e) output switch axis, but not (f) input drive axis.

axis, thereby preventing impacts along the input axis, but allowing them along the switch axis. In so doing, this device enables the use of resoswitches in applications like that depicted in Figure 4-2, where a micromechanical resoswitch replaces the switching transistor in a Class-E switched-mode power amplifier to greatly improve its efficiency by virtue of the much higher *FOM* of the resoswitch versus a semiconductor transistor.

Unfortunately, as shown in [43], the introduction of slots into the disk structure ends up decreasing the *Q* of the structure and shifting its frequency, both of which are undesirable. In addition, there is so far no simple closed-form analytical expression that governs the displacement gain factor afforded by this method; rather, finite element simulation is used to determine the gain. Furthermore, this method is applicable mainly to geometries where expansion and contraction occur along orthogonal axes, like wine-glass disks. It is less directly applicable to radial-contour mode disks that expand and contract equally
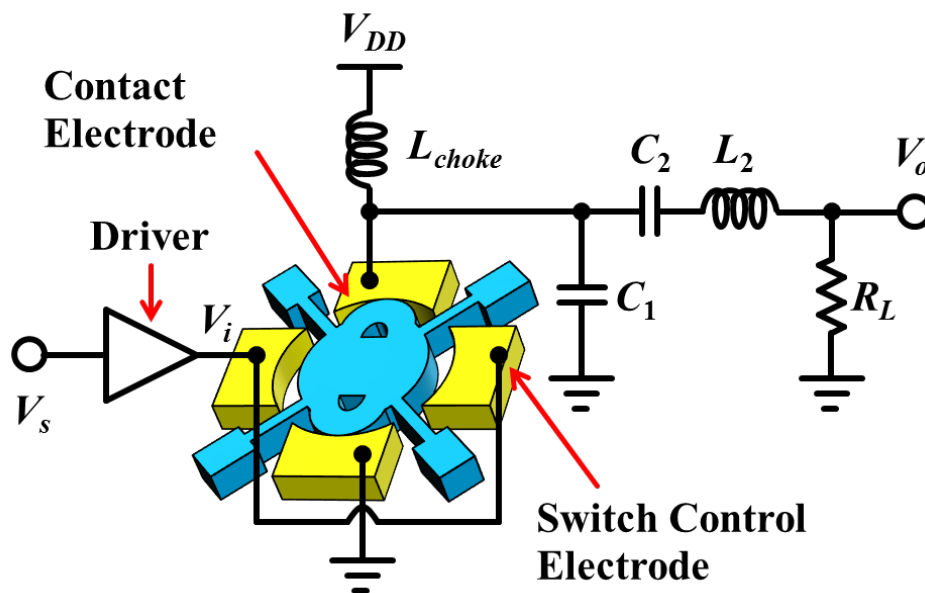
Figure 4-2: Circuit topology of a Class-E amplifier built using the slotted wine-glass mode resoswitch in place of a transistor, where the disk contorts more along the softer slotted axis to make contact.
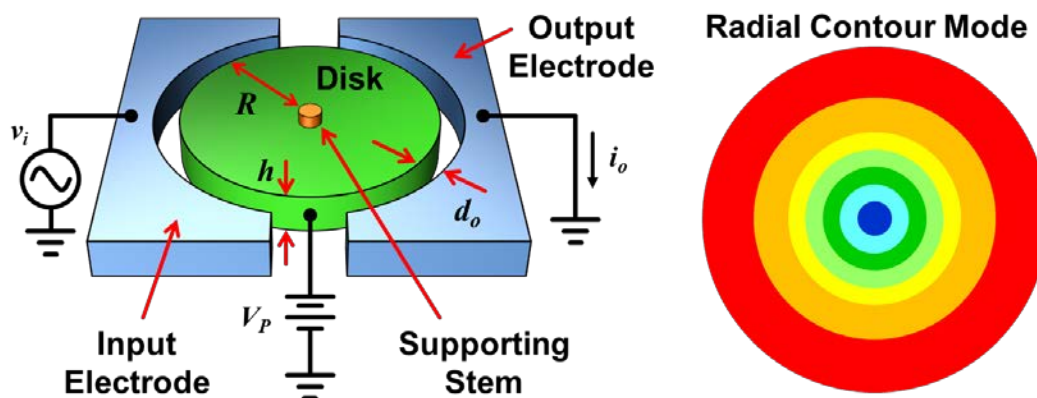
Figure 4-3: Schematic of a single contour-mode micromechanical disk resonator and its FEA-simulated mode shape.

along all radial axes (*c.f.*, Figure 4-3), so a better solution is desired if micromechanical power amplifiers are to harness the much higher frequency of radial-contour mode disks.

To overcome the above issues, this work takes a mechanical circuit design approach, as opposed to the device-centric approach of [43], that differs from that of [43] in that 1) it can be more readily applied to radial-contour mode disks capable of much higher fre-
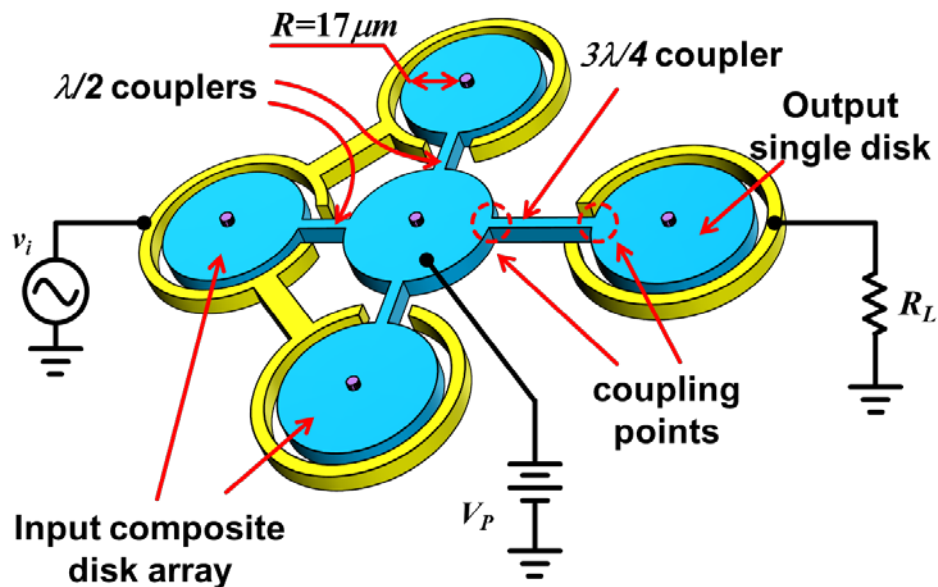
Figure 4-4: Schematic of the 152.3MHz radial contour-mode micromechanical displacement amplifier realized.

quency than the wine-glass disks of [43]; 2) it preserves the frequency and Q of its constituent resonators (whereas the method of [43] changed the frequency and lowered the Q); and 3) its digital method for gain specification is much more straightforward, accurate, and repeatable.

4.2 Micromechanical Displacement Amplifier

Figure 4-4 presents the schematic of the micromechanical displacement amplifier demonstrated in this work. Here, an array composite of disks on an input side (the left side) feeds via a 3 quarter-wavelength coupler into a single output disk (or another array) to effect an amplification of output disk displacement over that of the input. More specifically, on the left hand side, 4 disks with identical radii of 17μm are coupled by half-wavelength beams to form a composite array input resonant tank; while on the right hand side only one disk (again, with a 17μm radius) is used as the output tank. Electrodes for lateral capacitive transduction surround the output disk and three of the input disks, each spaced 100 nm from the disk sidewalls, and each fully surrounding its corresponding disk to favor the radial-contour resonant mode, depicted in Figure 4-3. Table 4-1 summarizes the design parameters of the device.

To operate the circuit, a dc-bias voltage V_P is applied to the conductive resonant structure (via the electrically connected ground plane underlying the disks) and an ac

Table 4-1: Micromechanical Displacement Amplifier Data.

Parameters	Values
Disk radius R	17 μm
Disk thickness h	3 μm
Electrode-to-resonator gap d_o	100 nm
Number of disks in input array N_I	4
Number of disks in output array N_O	1
Acoustic wave velocity of poly-silicon	8075.7 m/s
Resonance frequency f_o	153.2 MHz
Acoustic wave length λ	52.71 μm

voltage v_i at the resonance frequency applied to the input port. These voltages together generate an input force that drives the structure into resonance vibration. The velocity of the vibrating single output disk is then sensed as an output motional current generated across the V_P-biased time-varying disk-to-electrode capacitive gap.

4.2.1 Structural Design and Analytical Modeling

The use of a coupling beam dimensioned to correspond to a quarter-wavelength [30] at the frequency of resonance is key to maximizing the displacement gain provided by this design. The extensional mode coupling beam used here is similar in geometry and design to those used in previous vibrating RF MEMS devices, such as the micromechanical resonator array in the GSM-compliant oscillator of [46], and the LSI RF channel-select bandpass filter circuit of [47]. As in these works, the function of a given coupling beam is governed by its dimensions, and specifically on what fraction of a wavelength they correspond. For example, when an array of resonators is designed to form a composite resonator in order to lower motional impedance and raise power handling, as is done in both [46] and [47] [48], half-wavelength coupling beams are needed, since they simulate ideally infinite stiffnesses that accentuate one desired mode in which all resonators vibrate with the same amplitude. They further push all other modes to far away frequencies.

In fact, beams or bars vibrating in longitudinal or torsional modes can be modeled as transmission lines and therefore can use the transmission-line equations [49]. Figure 4-5 depicts one simple beam with length l, width w and thickness h. Dynamical state of an
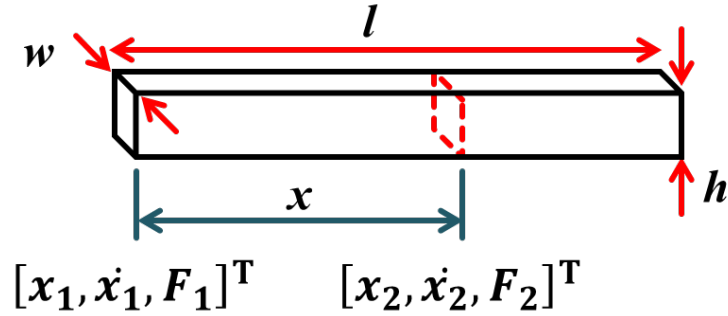
Figure 4-5: Geometry of a coupling beam.

arbitrary cross section plane along the longitudinal direction of the beam is described by the vector $[x, \dot{x}, F]^\mathrm{T}$, which contains displacement, velocity and force, respectively. The vector for the left end is written using subscript 1, whereas subscript 2 represents a plane spaced apart from the left end by a distance of x. Since the micromechanical resonant bodies and coupling elements are generally cascaded, thus the transmission *ABCD* matrix is usually used to describe the mechanical two-port networks. The transmission line equation between the two cross section planes separated with a distance x within the beam of Figure 4-5 is

$$\begin{bmatrix} \dot{x}_1 \\ F_1 \end{bmatrix} = \begin{bmatrix} \cos \alpha x & jZ_o \sin \alpha x \\ \dfrac{j}{Z_o} \sin \alpha x & \cos \alpha x \end{bmatrix} \begin{bmatrix} \dot{x}_2 \\ F_2 \end{bmatrix}$$

$$\begin{bmatrix} \dot{x}_1 \\ F_1 \end{bmatrix} = \begin{bmatrix} A & B \\ C & D \end{bmatrix} \begin{bmatrix} \dot{x}_2 \\ F_2 \end{bmatrix}$$

(4.1)

where Z_o is the characteristic mobility and α is the propagation constant defined as follows,

$$Z_o = \frac{1}{A\sqrt{\rho E}} = \frac{1}{wh\sqrt{\rho E}}$$

(4.2)

$$\alpha = \frac{\omega}{\sqrt{E/\rho}} = \frac{2\pi}{\lambda}$$

where ρ and E are density and Young's modulus of the material, respectively. $\sqrt{E/\rho}$ and λ are the velocity and wavelength of the extensional wave, respectively. And when $x = l$, then (4.1) becomes

$$\begin{bmatrix} \dot{x}_1 \\ F_1 \end{bmatrix} = \begin{bmatrix} \cos \alpha l & jZ_o \sin \alpha l \\ \dfrac{j}{Z_o} \sin \alpha l & \cos \alpha l \end{bmatrix} \begin{bmatrix} \dot{x}_2 \\ F_2 \end{bmatrix} \tag{4.3}$$

which describes the transmission line behavior of the coupling beam from one end to the other.

When $l = \lambda/2$, then $\alpha l = \pi$, and (4.3) reduces to (4.4), which means that the half-wavelength ($\lambda/2$) coupler forces the equal vibration velocity and displacement amplitudes but opposite phase (180°) on the coupling points, i.e. its left and right ends.

$$\begin{bmatrix} \dot{x}_1 \\ F_1 \end{bmatrix} = \begin{bmatrix} -1 & 0 \\ 0 & -1 \end{bmatrix} \begin{bmatrix} \dot{x}_2 \\ F_2 \end{bmatrix}$$

$$\dot{x}_1 = -\dot{x}_2 \tag{4.4}$$

$$F_1 = F_2$$

The characteristic of $\lambda/2$ described above forces equal vibration amplitude and phase of the structures attached to the coupling points. That is why as shown in Figure 4-4, the present displacement amplifier design utilizes half-wavelength couplers in its input array to realize a composite resonator array that behaves like one resonator. As in [48], this "one" composite resonator has an effective stiffness at any given location equal to N_I times that at the same location on a single one of its constituent disk resonators, where N_I is the number of resonators used in the array. In effect, arraying can be used to increase the effective stiffness of a composite resonator, which as will be seen, is instrumental to attaining a digitally specifiable displacement gain using the circuit of Figure 4-4.

To effect the most efficient displacement gain, a quarter-wavelength coupler is utilized to connect the input and output networks, much like those used to set the bandwidths of filters like that of [30]. In the micromechanical filters so far demonstrated, quarter-wavelength elements generally couple purely symmetric networks that present the same impedance to the coupling element at each of its attaching ends, i.e., the resonators or composites attached to both ends of the coupler are identical. The displacement amplifier of this work differs from filters in that it quarter-wavelength couples dissimilar

resonator structures, specifically, a 4 disk array composite on one (input) side, to a single disk on the other (output) side.

Displacement amplification occurs because quarter-wavelength coupling constrains the mechanical circuit network so that the energy or power on the left and right sides are equal. This behavior can also be modeled through (4.3) by plugging $l = \lambda/4$ and $\alpha l = \pi/2$.

$$\begin{bmatrix} \dot{x}_1 \\ F_1 \end{bmatrix} = \begin{bmatrix} 0 & jZ_o \\ j/Z_o & 0 \end{bmatrix} \begin{bmatrix} \dot{x}_2 \\ F_2 \end{bmatrix} \tag{4.5}$$

Therefore, the velocity and force relationship between the two coupling points becomes

$$\dot{x}_1 = jZ_o F_2$$
$$F_1 = \frac{j}{Z_o} \dot{x}_2 \tag{4.6}$$

Multiplying the two equations in (4.6) and apply absolute value operation on both sides

$$|F_1 \cdot \dot{x}_1| = |F_2 \cdot \dot{x}_2| \tag{4.7}$$

Product of force and velocity equates mechanical power and equal mechanical power means equal energy over the same amount of time. Mechanical energy becomes pure elastic energy as shown in (4.8) when the displacement reaches maximum while velocity drops to zero.

Since the stiffnesses of the input and output arrays now differ, different amount of displacements ensue to maintain the same energy on both sides. Quantitatively, the gain factor is governed by:

$$E_I = E_O \rightarrow \frac{1}{2} k_I (X_I)^2 = \frac{1}{2} k_O (X_O)^2$$
$$\frac{X_O}{X_I} = \sqrt{\frac{k_I}{k_O}} = \sqrt{\frac{N_I}{N_O}} \tag{4.8}$$
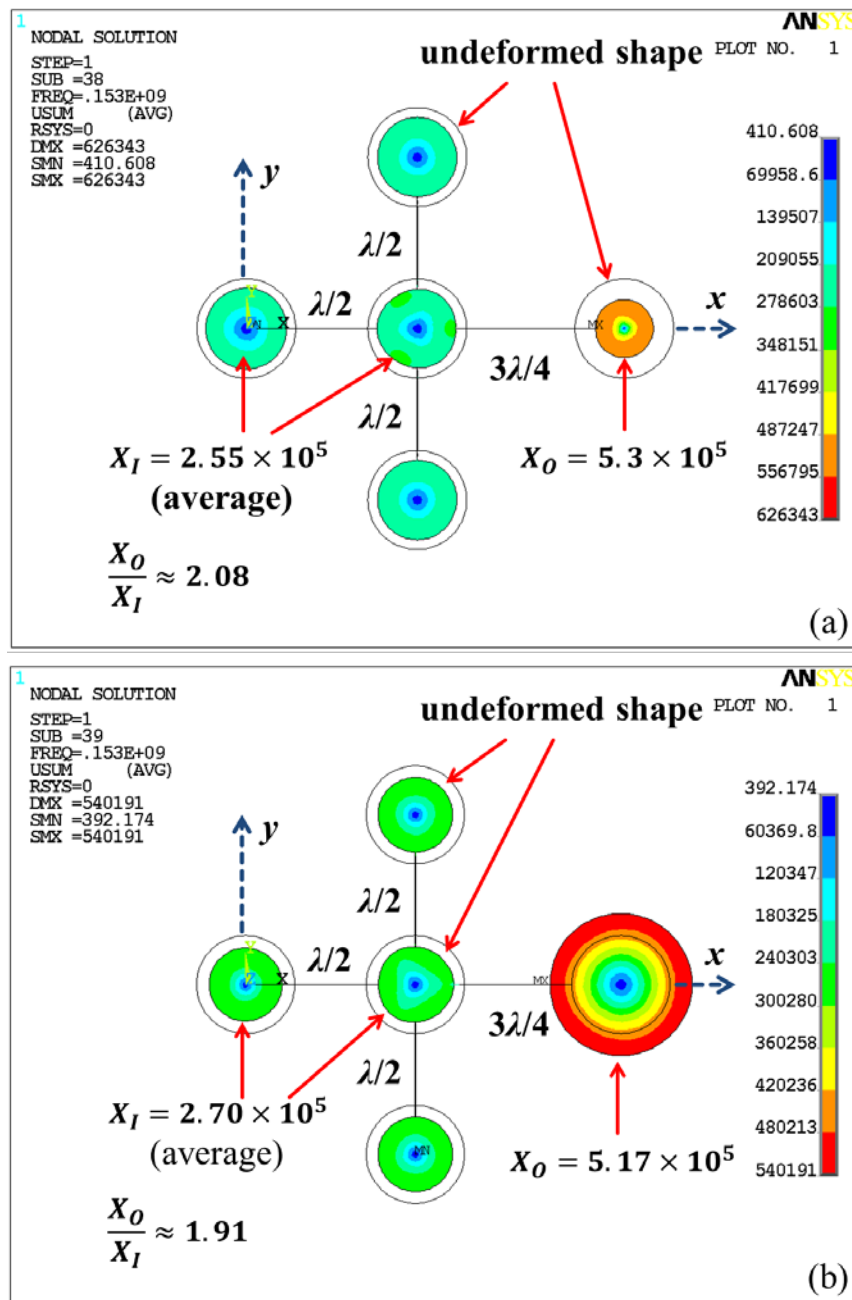
Figure 4-6: FEA modal simulations of the 153.3MHz contour-mode micromechanical displacement amplifier showing displacement gain of about (a) 2.08× for the lower frequency in phase mode and (b) 1.91× for the higher frequency out of phase mode.
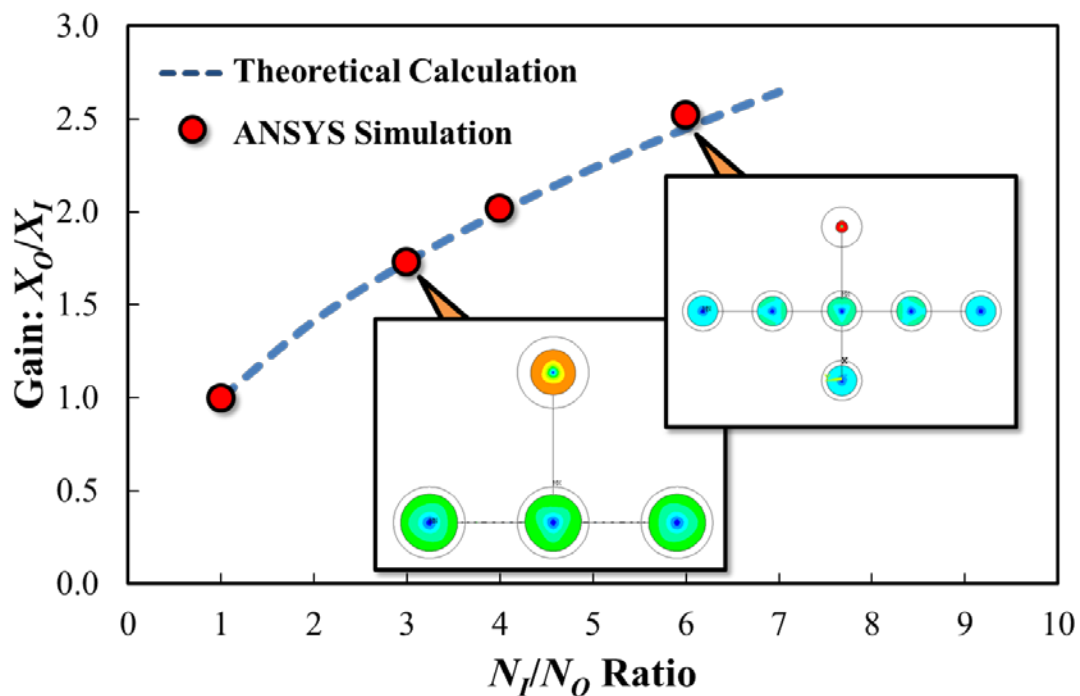
Figure 4-7: Plots of theoretical calculated and ANSYS simulated displacement gains for various N_I/N_O ratios.

where subscripts I and O denote parameters for the input and the output ports (or "tanks"), respectively; E is the total vibration energy stored in a given resonant tank at resonance; k is the equivalent stiffness of a given tank at the coupling location; X is the displacement amplitude of a given tank; and N is the number of resonators in the composite array (i.e., in the tank) at each port.

Equation (4.8) indicates that the displacement gain of this mechanical circuit is governed simply by the square root of the ratio of the number of resonators in the input array composite to that in the output composite.

4.2.2 Finite Element Verification

Figure 4-6 presents finite-element modal simulations (ANSYS) of the Figure 4-4 structure, showing a displacement amplification of around 2.0 for both in and out of phase modes, which matches and verifies the value predicted by (4.8). Finite element simulations with other N_I/N_O ratios are also performed and plotted on Figure 4-7 together with the theoretical curve predicted by (4.8), which indicates a close match between the FEA simulation and the analytical calculation. Like amplifiers in analog circuits, the displacement amplifier of Figure 4-4 is also capable of being cascaded to form multiple
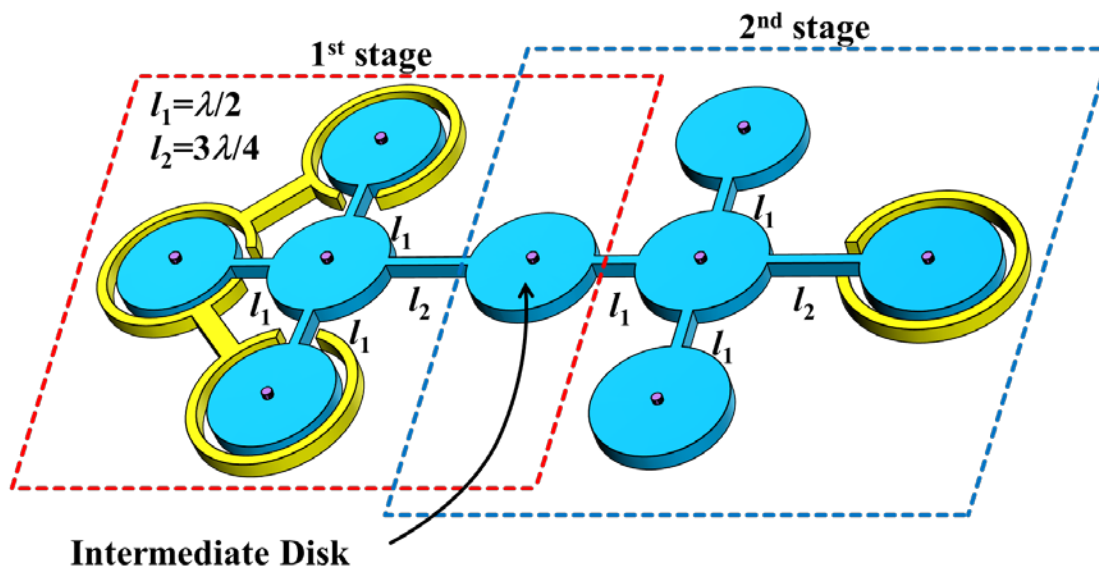
Figure 4-8: Schematic of a 2-stage cascaded displacement amplifier containing two basic cells of amplifier shown in Figure 4-4.

stages for achieving even higher displacement gains. Figure 4-8 depicts a two-stage cascaded displacement amplifier using the one in Figure 4-4 as a cell. As shown on Figure 4-8, the first stage is laying on the left and the second stage is laying on the right. The two stages are overlapping, where the labeled intermediate disk acts as both the output disk of the first stage and the constituent disk of the input composite disk array of the second stage simultaneously. By cascading two identical stages with displacement gain of 2.0 each, the overall displacement amplification from the left most input disk array to the right most output disk is therefore 2×2=4. Figure 4-9 presents the ANSYS modal simulation of the cascaded amplifier indicating a displacement gain of around 4.38, which again verifies the validity of both the displacement amplifier and the cascaded topology. The benefit of cascade is to achieve displacement gain with fewer disks, i.e. less area. If single stage was used to achieve the same 4× displacement gain, 17 disks would have been required, whereas only 9 disks are used in the two-stage cascaded design of Figure 4-8.

4.2.3 Equivalent Circuit Simulation

Beyond finite element simulation, given that it represents a circuit approach to attaining displacement gain, it should be no surprise that the Figure 4-4 circuit is quite amenable to simulation via circuit simulators, such as SPICE. As in [30] and [33], the micromechanical resonator can be modeled as series RLC resonant tank as depicted in Figure 4-10(a), where the element values can be calculated by:
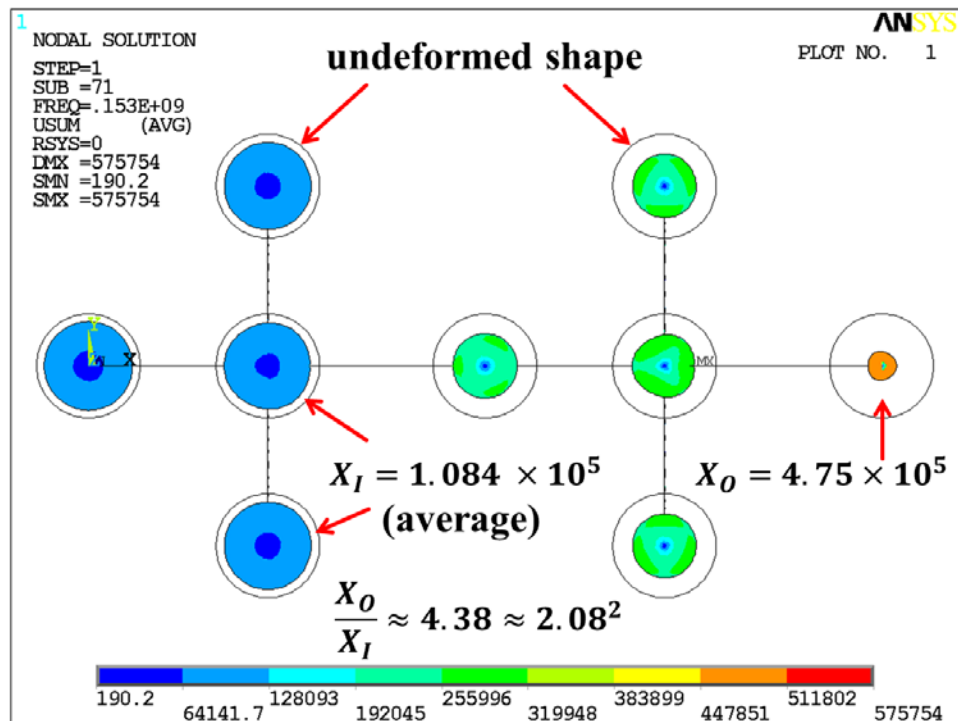
Figure 4-9: FEA modal simulations of the two-stage cascaded 153.3MHz con-tour-mode micromechanical displacement amplifier showing displacement gain of about 4.38×, which is approximately equal to the square of simulated single stage displacement gain.

$$c_x = \frac{1}{k_{re}} \qquad\qquad l_x = m_{re} \qquad\qquad r_x = \frac{1}{c_{re}} = \frac{\sqrt{k_{re}m_{re}}}{Q}$$

$$\eta_e = \frac{V_P \varepsilon 2\pi Rh}{d_o^2} \qquad\qquad\qquad \eta_c = 1$$

(4.9)

where k_{re}, m_{re} and c_{re} are the equivalent stiffness mass and damping coefficient, respectively, and Q is the quality factor of resonance.

The coupling beams that are modeled as a transmission lines previously can be represented by the T-model shown in Figure 4-10(b). Solving the series and shunt impedances yields:

(a)

(b)
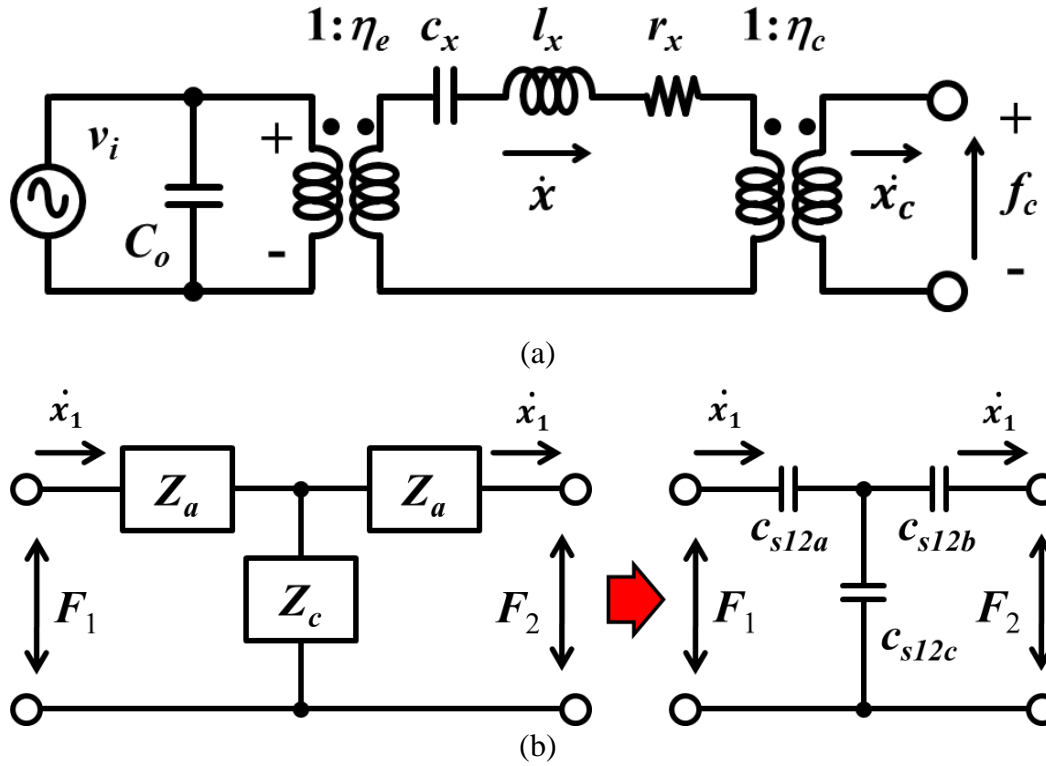
Figure 4-10: Equivalent circuits for (a) a micromechanical resonator and (b) a coupling beam using a transmission line *T*-model.

$$Z_a = Z_b = \frac{D-1}{B} = \frac{1}{j\omega_o C_{s12a}} = \frac{1}{j\omega_o C_{s12b}}$$

$$Z_c = \frac{1}{B} = \frac{1}{j\omega_o C_{s12c}}$$

(4.10)

where *A* and *C* are the elements of the *ABCD* matrix in (4.1).

Figure 4-11 presents the equivalent circuit of the displacement amplifier shown in Figure 4-4 with the element values calculated using (4.9). Figure 4-12 is the simulated small signal currents in input and output meshes, which correspond to the velocity of each vibrating disk. As can be seen from the simulation results, the four disks in the input composite array have the same vibration velocity and thus the same displacement amplitude due to $\lambda/2$ coupling, and the displacement of the output disk is exactly twice that of the input disks verifying that a displacement amplification gain of 2.0 is achieved.

(a)

(b)
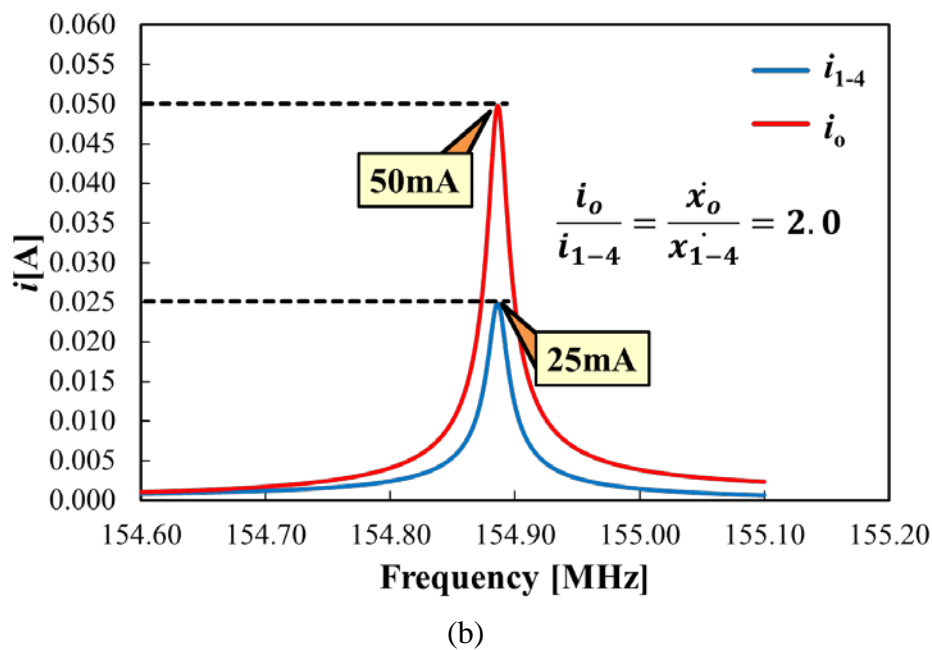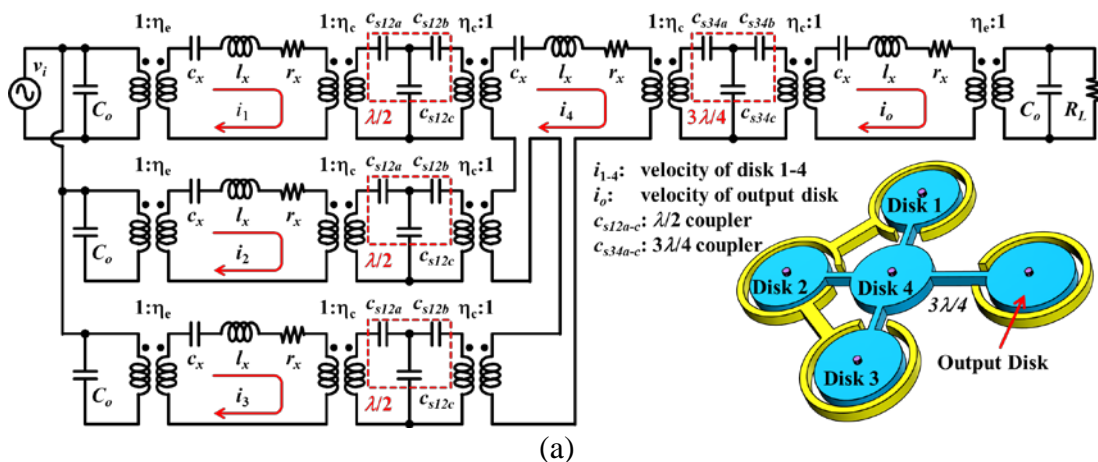
Figure 4-11: (a) Equivalent circuit of the displacement amplifier shown in Figure 4-4 and (b) small signal (AC) simulation using SPICE, showing a motional current gain of 2.0 at resonance between the output disk and the disks in the input composite array.

Figure 4-12(a) is the equivalent circuit of the two-stage cascaded displacement amplifier and Figure 4-12(b) shows the simulated small signal motional currents of first stage, second stage and output disks, indicating that the displacement has been amplified along the stages and a displacement gain of 4.0 has been obtained eventually.

The value of such amenability to circuit representation, of course, is the resultant amenability to simulation and computer aided design programs that can conveniently

(a)

(b)
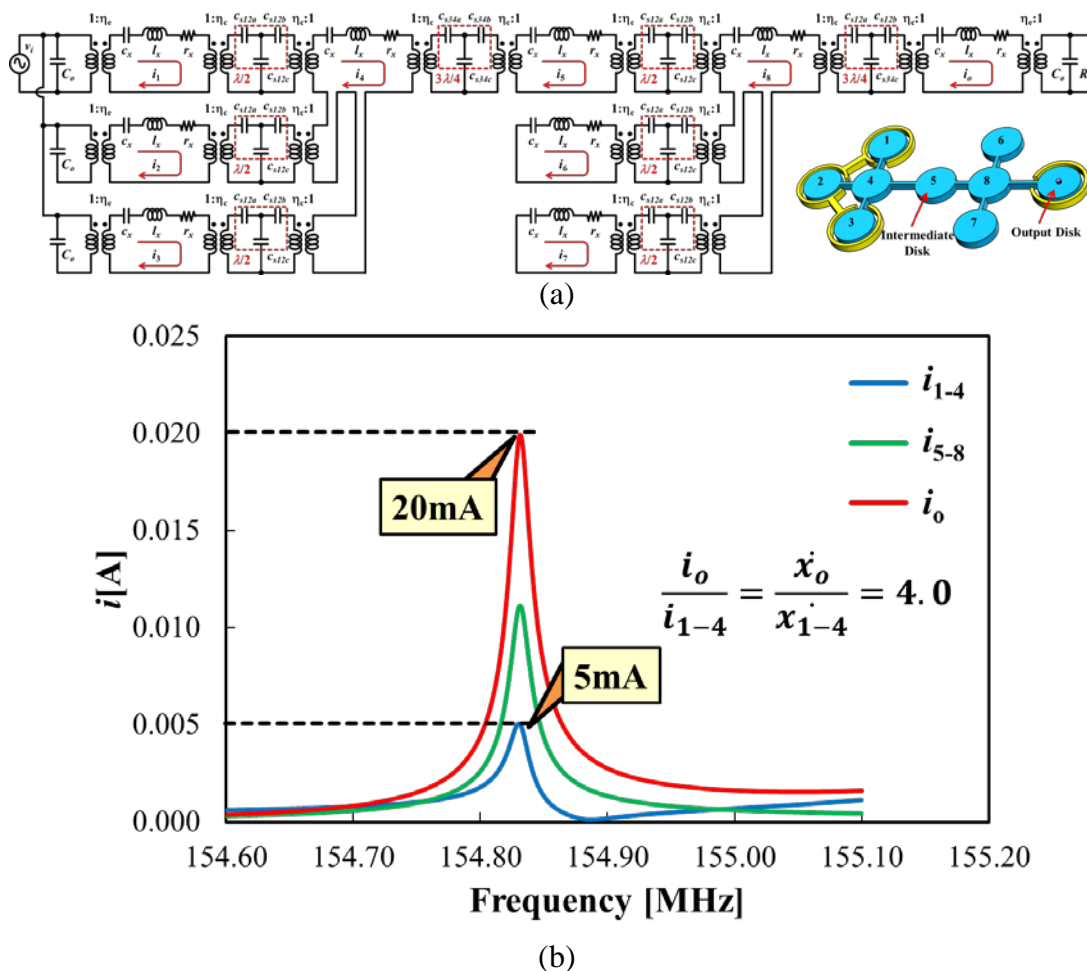
Figure 4-12: (a) Equivalent circuit of the two-stage cascaded displacement amplifier shown in Figure 4-8 and (b) SPICE small signal (AC) simulation, showing a motional current gain of 4.0 at resonance between the output disk and the disks in the first stage input composite array.

analyze and perhaps automatically generate more complex and more capable circuits based on the displacement gain principles of the Figure 4-4 circuit. Indeed, the analogy is not unlike that for transistor integrated circuits.

4.3 Measurement Results

Figure 4-13 and Figure 4-14 present the SEM and measured frequency characteristics for a fabricated version of the displacement amplifier circuit of Figure 4-4, showing a center frequency of 153.2 MHz and a Q of 10,500, which are essentially the same as that of a single resonator, verifying that this approach does not degrade Q. This is consistent
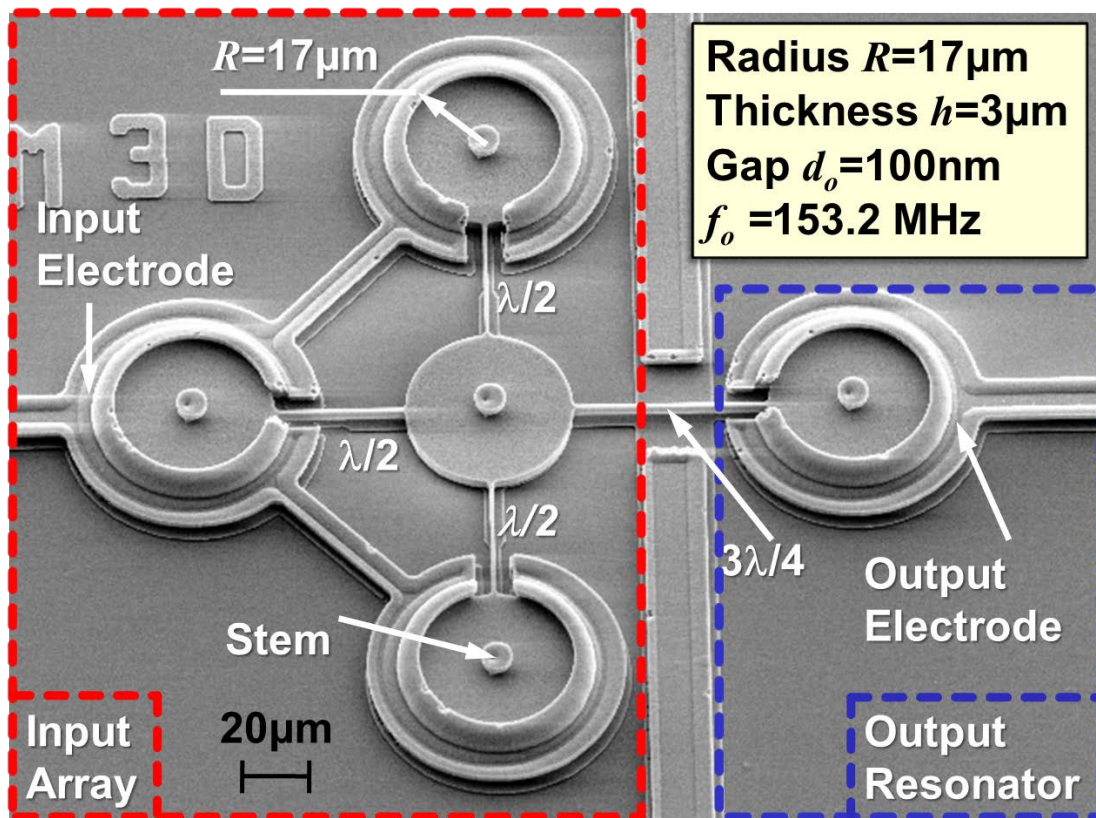
Figure 4-13: SEM photo of the contour-mode 153.2 MHz micromechanical displacement amplifier.

with [50], which showed that an array of identical resonators retains the same Q as any one of its constituents.

While the frequency characteristic of Figure 4-14 was measured using a direct network analyzer set-up [51], such as depicted in Figure 4-4, determination of displacement gain requires a more involved set-up. In particular, a set-up that allows simultaneous measurement of input and output disk displacement is needed. To do this, the "RF/LO mixing overtone test setup" introduced in [43] and depicted in Figure 4-16 is used. In this set-up, a network analyzer is still used as a signal source, but a spectrum analyzer is used (rather than the network analyzer) to sense the simultaneous output currents of both the input and output tanks. The local oscillator applied to the resonant structure (atop the dc-bias) mixes the output current of the input tank to higher frequencies, separating it in the frequency domain from the input drive current of the source, and thereby allowing detection of this current without interference from the drive current.
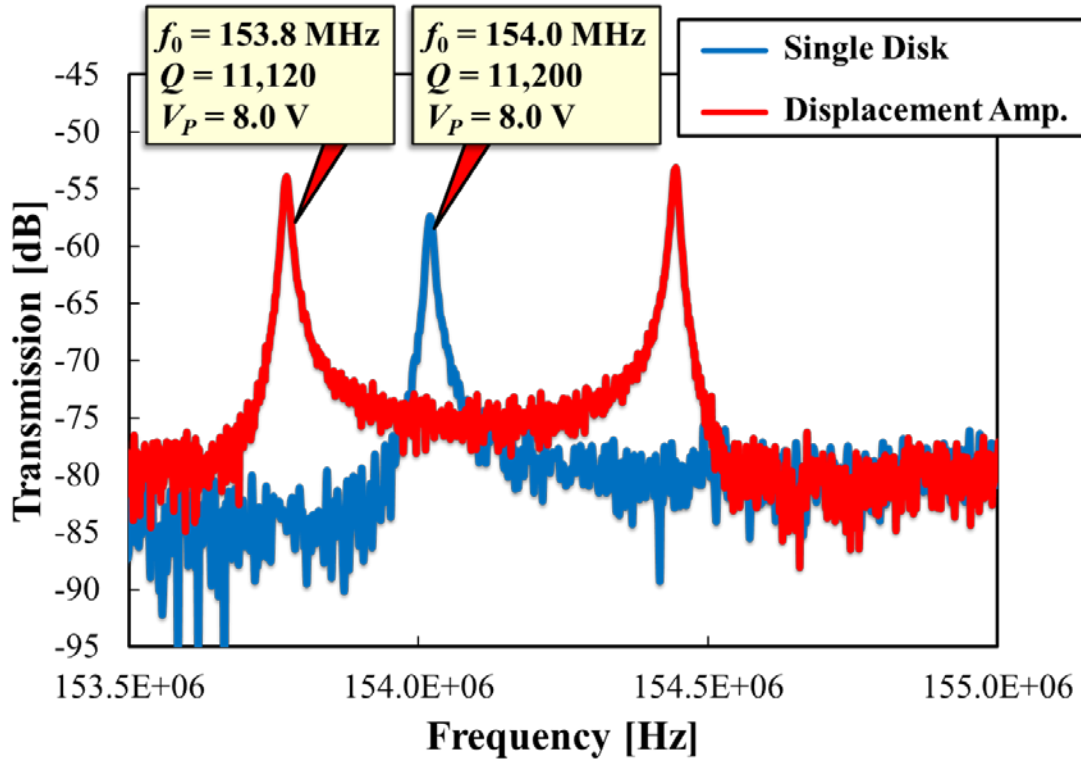
Figure 4-14: Measured frequency responses of a single disk and the displacement amplifier shown in Figure 4-13.

$$X = \sqrt{\frac{P}{R_L}} \frac{d_o^2}{V_P \cdot (2\pi\varepsilon_o R h) \cdot \omega_o} \tag{4.11}$$

The detected output power can then be converted to the associated disk displacement amplitude using (4.11), where R_L is the load resistance, d_o is the disk-to-resonator gap, R and h are the radius and thickness of the disk, respectively, and ω_o is its resonance frequency. Using (4.11) and plotting versus frequency yields the curves of Figure 4-15, where the ratio of the output disk displacement to that of each input disk in the input array composite is 2.17×, which is close to the prediction of (4.8).
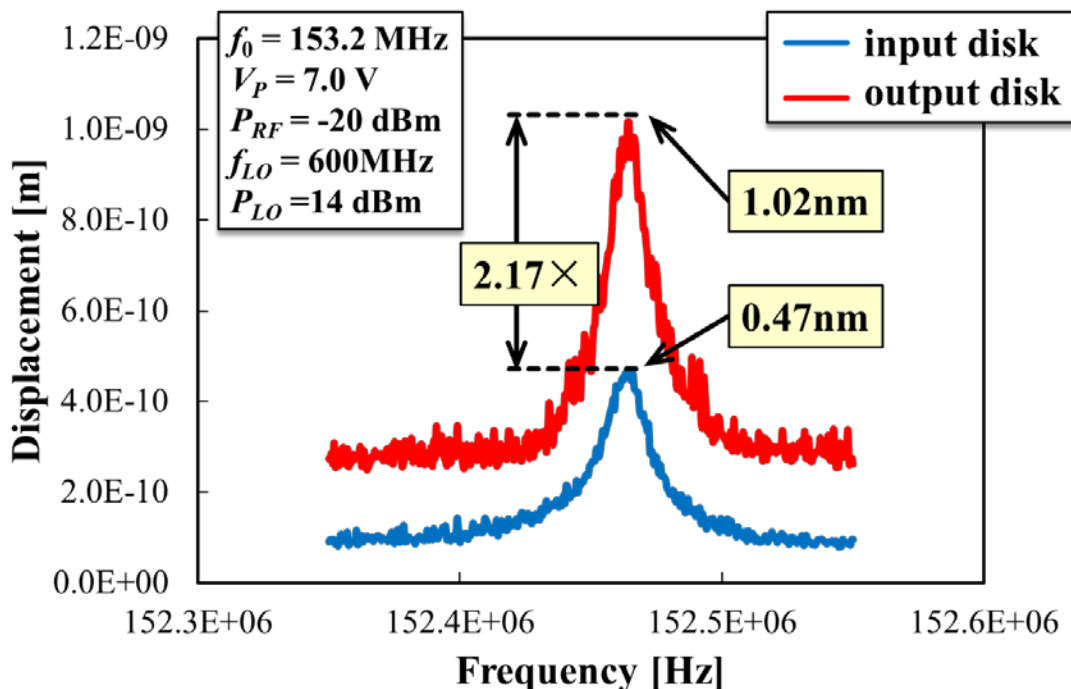
Figure 4-15: Input and output disk displacements using the measurement setup introduced in [43], clearly showing an amplification ratio of 2.17×.

4.4 Micromechanical Displacement Amplifier Based Resoswitches

As introduced in the previous section, the primary purpose of developing the displacement amplifier in this work is to generate a larger displacement at the output port than at the input in an air gap capacitively transduced micromechanical resonator, where the air gap is defined by the same sacrificial layer and thus is homogenous across the device. Larger displacement at output means that, as the disk is driven hard and harder, impact first initiates at the output port which then limits the vibration amplitude from growing, and therefore the unwanted impacts at the input port which is considered to be the one of the main reasons that caused the switch degradation observed in [37], can be completely avoided.

To verify the benefit of displacement amplification, the micromechanical displacement amplifier demonstrated in this work has been driven and tested as a resonant switch using a circuit shown in Figure 4-17(a). The circuit is mimicking the one used in [37], which used a unity gain buffer to drive the coaxial cables. The only modification made here is using a wider bandwidth buffer (LMH6559), whose frequency response has been measured and plotted in Figure 4-17(b). A bandwidth of 1.25GHz is a little lower than expectation but already sufficient for measuring the 153.3MHz device in this work.
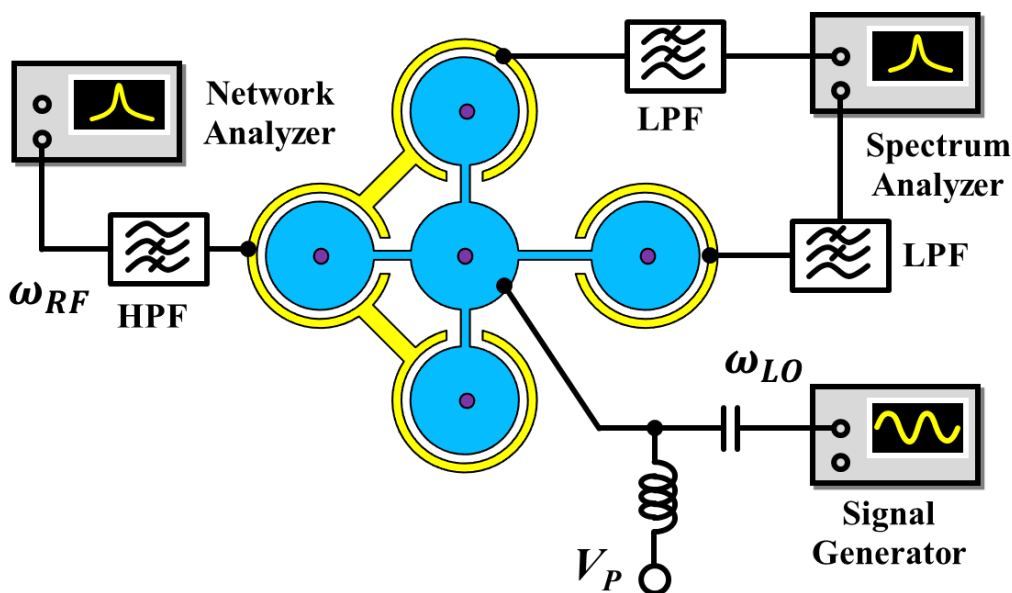
Figure 4-16: Schematic of the RF/LO mixing overtone test setup used to simultaneously measure the output currents (= displacements) of the input and output resonator networks.

Figure 4-18 shows the frequency responses of the resoswitch driven by various ac input voltages ranging from 1.41V to 2.51V with $V_P = 30$V, where the flat top response shows up starting from $v_i = 1.78$V, and as v_i increases flat top bandwidth gets widened. When the device is driven within the flat band, the time domain switch signal was recorded and plotted on Figure 4-19, where a sinusoidal switch output signal with a peak-to-peak amplitude of around 0.15V was obtained. The output signal has been attenuated from 30V down to 0.15V due to a high contact resistance, around 200kΩ as extracted, which forms a voltage divider with the bleeding resistor R_B shunting the input node of the buffer to the ground.

Despite a relatively small output power, the signals shown here are still hot switched cycles. To evaluate the reliability, the switch was operated under the same driving condition for 13 days without failure at the frequency of 153.4MHz in vacuum environment, which corresponds to more than 173 trillion cycles as presented in Figure 4-20. This is a lifetime 10× better than that of [37], 7-8 orders of magnitude higher than the 10 million cycles typically achieved by hot-switched RF MEMS switches [10] and 2-3 orders of magnitude higher than the 100-900 billion cycles of cold-switched RF MEMS switches [52] [35]. And yet, this is not the absolute lifetime of this switch, as the sudden signal amplitude drop shown in Figure 4-20 is not caused by switch failure, e.g. sticking or contact degradation. In fact, it is the change of resonance frequency that makes the frequency of the driving source out of the flat band region and thus the displacement of the disk is
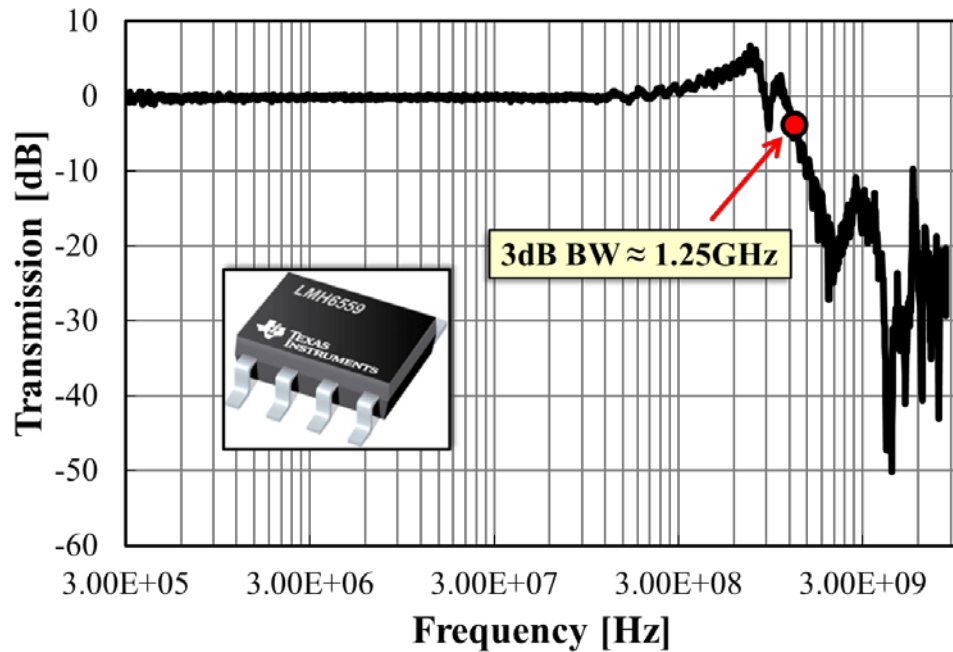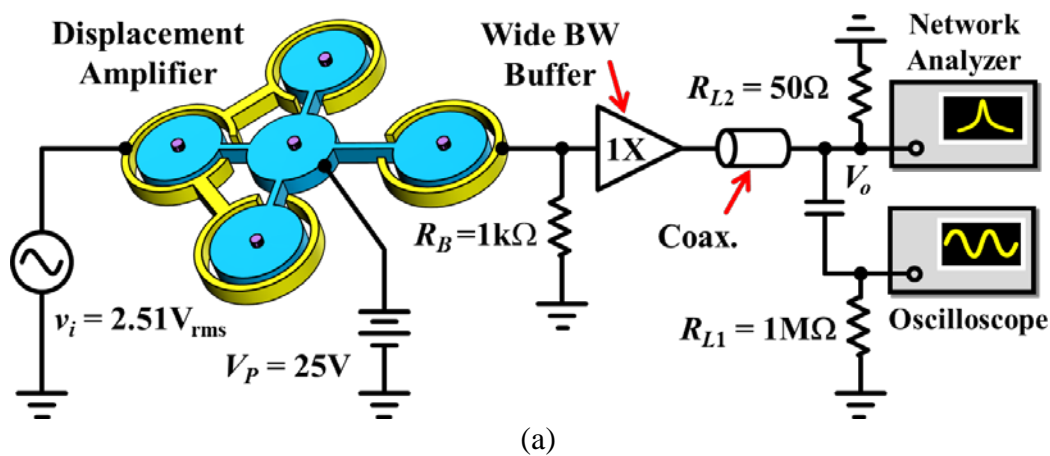
Figure 4-17: (a) Schematic of the testing circuit for the displacement amplifier based resoswitch, which measures the frequency domain transmission curve and time domain oscillation signal simultaneously. (b) Frequency response of the wide BW unity gain buffer.

insufficient to make effective contacts at the output. Therefore, when a close loop driving scheme is implemented as shown in Figure 4-21, the lifetime of the resoswitch is expected to be even longer than the current 173.9 trillion, and probably can meet 1-2 quadrillion required by switched-mode power amplifiers in cell phone transceivers.
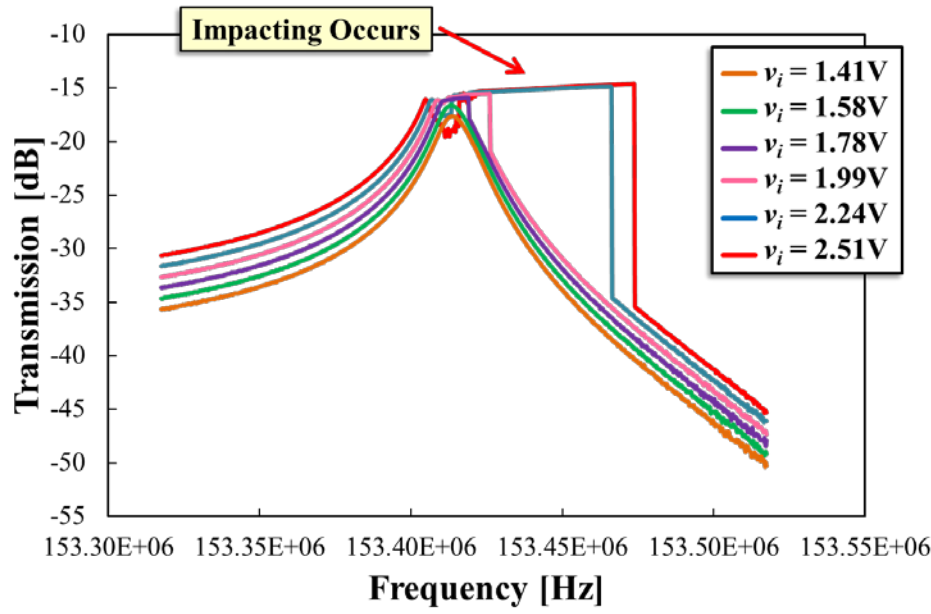
Figure 4-18: Frequency response (in vacuum) of the displacement amplifier based resoswitch for varying input ac voltage amplitudes.
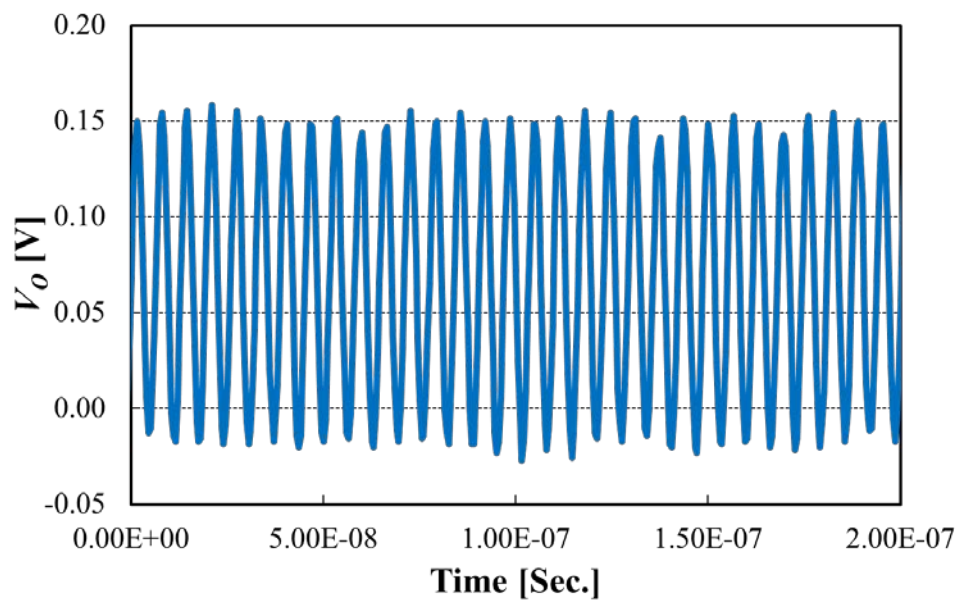
Figure 4-19: Oscilloscope (i.e., time domain) waveform at the resoswitch output node of Figure 4-16 (a) when driven by a resonance input signal with 2.51V amplitude.
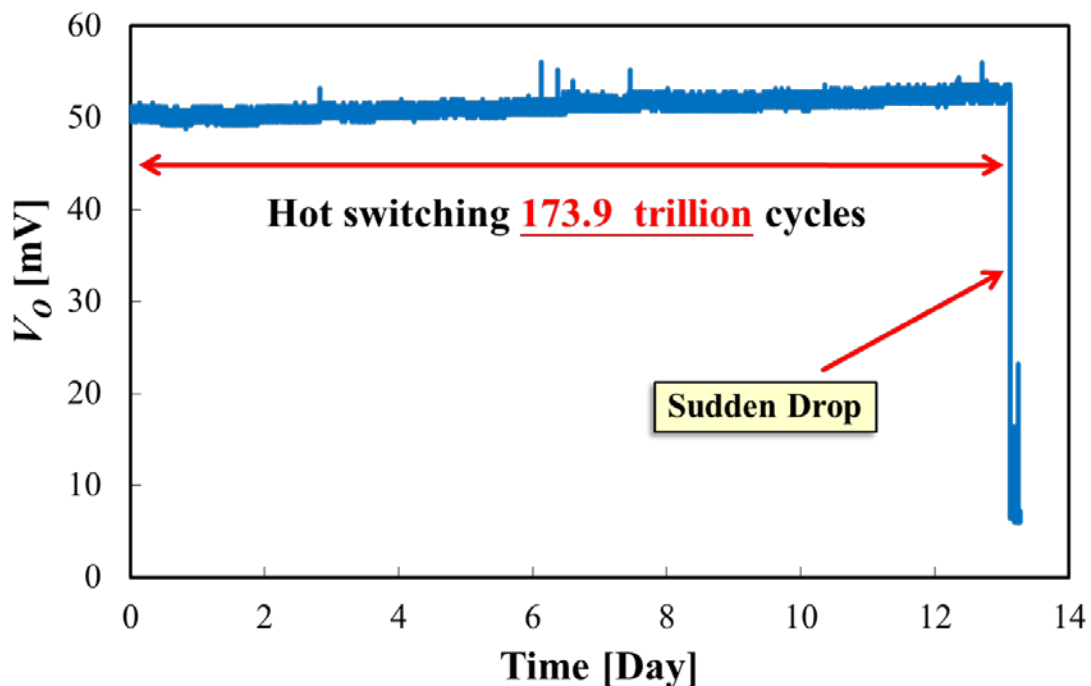
Figure 4-20: Lifetime of the displacement amplifier based resoswitch.

4.5 Conclusions

The successful use of circuit design methodologies to demonstrate a mechanical circuit capable of amplifying displacements by a factor dependent upon the ratio of the number of input and output resonators used represents a significant leap forward in mechanical circuit design capability. The ease with which this approach allows accurate specification of displacement gains for any type of resonator without any need to alter the fabrication process technology used and without any degradation in frequency or Q, encourages similar circuit-centric approaches for even larger mechanical circuits. The displacement gain function achieved here is especially useful for resonant switches, as it further idealizes the operation of such switches, which in turn should greatly improve the performance of switched-mode power amplifiers and converters that utilize them. And the resoswitch based on this displacement amplifier was successfully demonstrated that achieves an unprecedented lifetime of 173.9 trillion cycles.
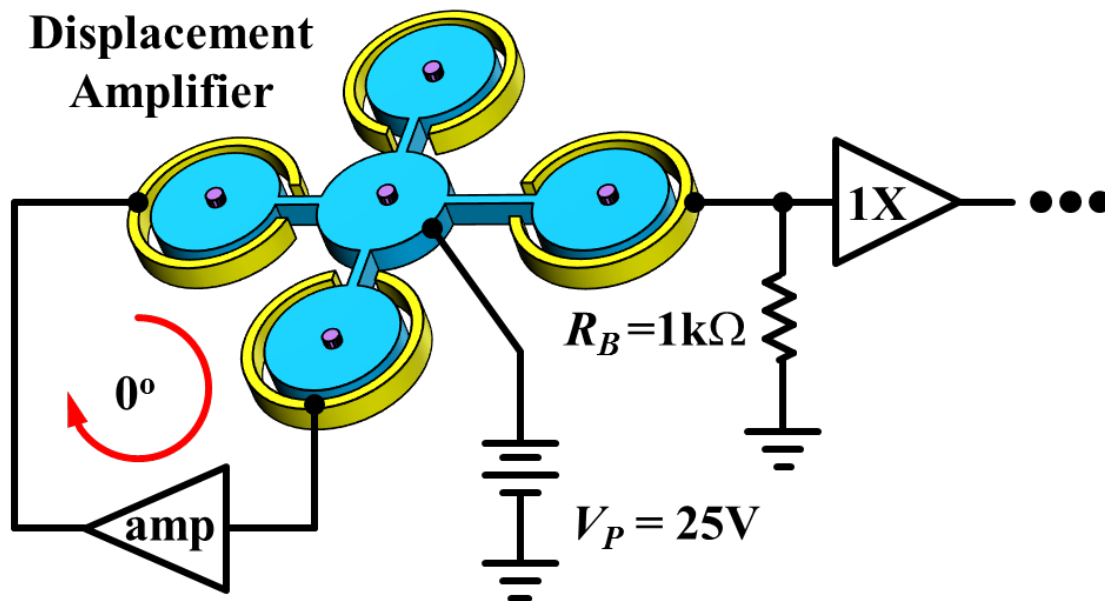
Figure 4-21: Closed loop oscillatory driving scheme for more accurate lifetime measurement of displacement amplifier based resoswitch.

CHAPTER 5 *Micromechanical Resonant Charge Pump*

The reduction of power supply voltage with each new generation of CMOS technology continues to complicate the design of charge pumps needed for high voltage applications, such as the increasing number of MEMS-based ones, e.g. gyroscopes, timing oscillators, gas sensors, etc., that integrate into systems alongside transistors chips. Indeed, aggressive scaling in CMOS leading to lower dielectric and junction breakdown voltages have forced the use of customized CMOS processes, e.g., with increased gate oxide thicknesses and/or added deep-n-wells [53]. Clearly, advances in transistor technology are going in the opposite direction of the needs of high voltage MEMS applications.

Well, if MEMS benefits from such large voltages, then they should have no problem handling such voltages. So as long as we're already using MEMS, why not also use them to generate their own needed voltages? This work does just this by exploiting the longevity and low actuation voltage attributes of recent resonant micromechanical switches (a.k.a., "resoswitches") [37] to replace the diodes or transistor switches in a Dickson's charge pump topology, *cf.* Figure 5-1(b) [20], and realize a MEMS-based charge pump, *cf.* Figure 5-1(a), that avoids the turn-on voltage and breakdown limitation of CMOS. With much higher breakdown voltages than transistor counterparts, the demonstrated MEMS charge pump implementation should eventually allow voltages higher than 50V desired for capacitive-gap transduced resonators that presently dominate the commercial MEMS-based timing market [54].

5.1 Introduction

With very few exceptions, capacitively transduced MEMS devices simply perform better when high voltages are available. Whether the device is a simple resonator, a gyroscope, an accelerometer, a movable mirror, or a motor, the higher the available voltage, the larger the output signal, as measured by a current, a voltage, or a displacement. In a perfect world, the preferred voltage used for MEMS devices would probably be in the 100-200V range.
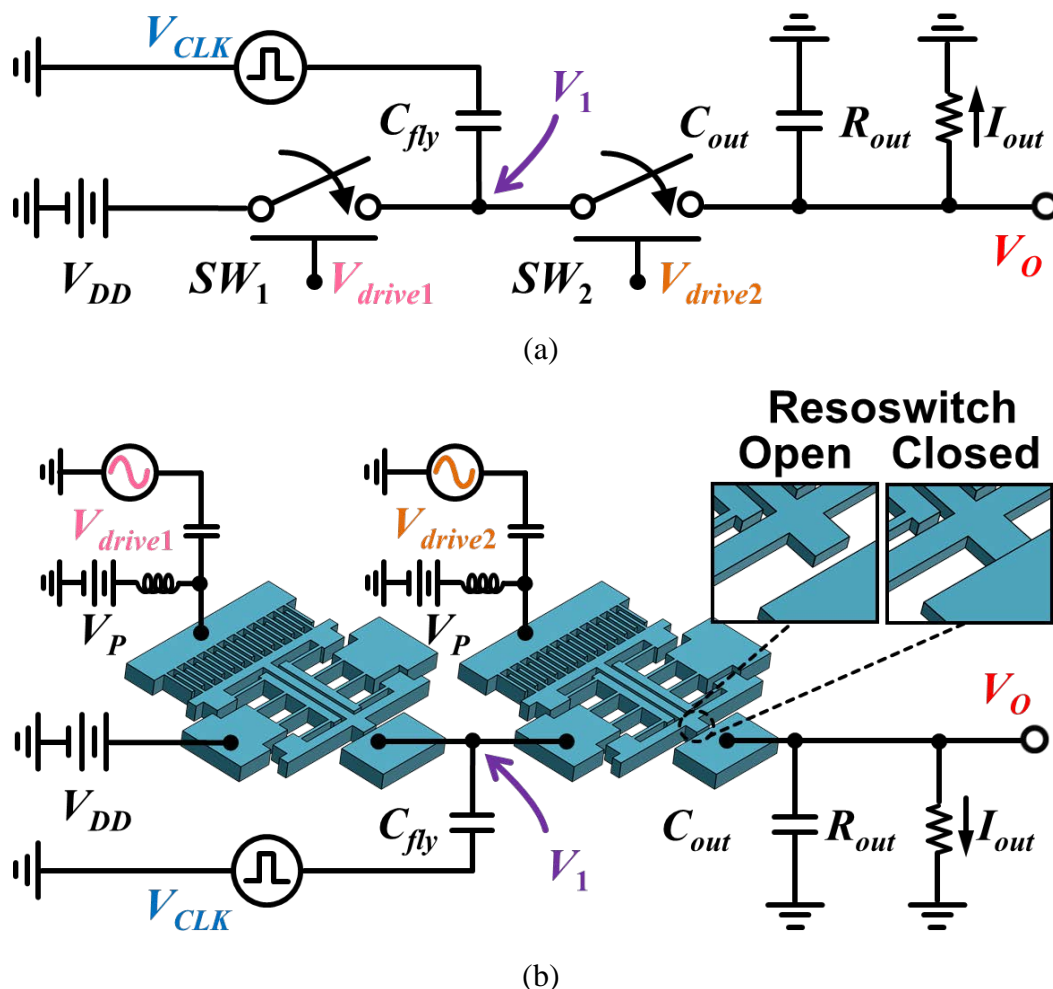
Figure 5-1: Circuit topology of (a) a single stage Dickson charge pump; and (b) the single stage micromechanical charge pump employing two resoswitches.

Unfortunately, other technologies—e.g., the batteries, the transistors with which the MEMS are often enjoined—cannot supply or do not often play well with such large voltages. Nevertheless, some MEMS products on the market require large voltages, such as digital micromirror displays (DMD) [55] and the high Q capacitively transduced resonators [54] used in some timing oscillators. Many of these products rely on charge pumps to supply such voltages, most often realized via the transistor technology that accompanies them. So far, CMOS based charge pumps perform well when generating voltages on the order of 10-15V, but for higher voltages (>15V) transistor body effect [56] substantially degrades pumping efficiency, and dielectric and p-n junction breakdown ultimately limits the maximum attainable voltage. Voltages exceeding 30V call for custom (expensive) CMOS technologies, such as SOI [57] or triple/deep n-well versions [53]. Indeed, it
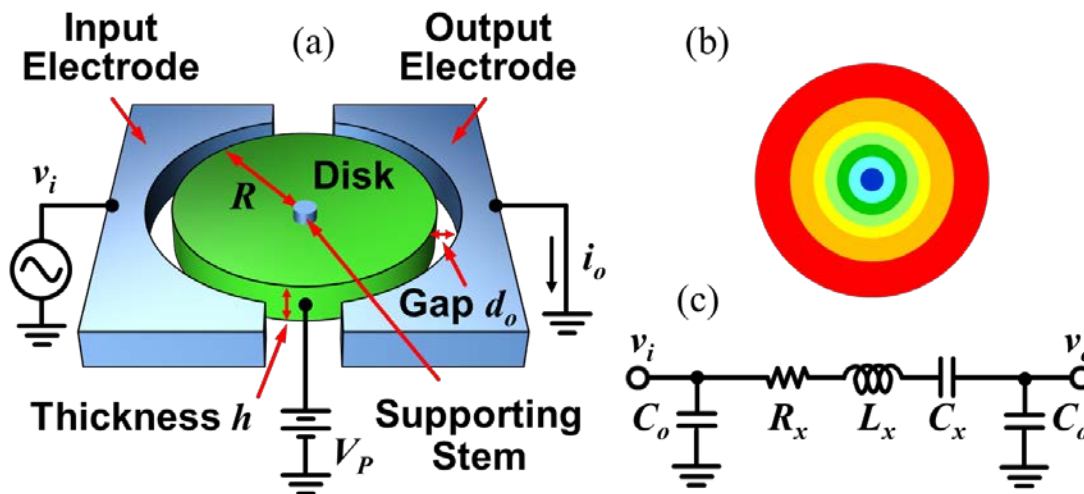
Figure 5-2: (a) Schematic of a radial mode disk resonator, (b) FEM mode shape and (c) its equivalent circuit.

would be nice if voltage levels required or desired by the MEMS devices could be decoupled from other technologies.

In response, this work demonstrates a MEMS-based charge pump, *cf.* Figure 5-1, that employs micromechanical resoswitches in a Dickson configuration to generate $2V_{DD}$ from V_{DD} power supply using single stage. Here, the use of mechanical switches eliminates diode or threshold voltage drops and raises the breakdown voltage limit to over 100V. This MEMS-based circuit also accepts a much wider range of input DC voltages, from values much smaller than a typical transistor threshold, to values much larger than a transistor's breakdown voltage. In most cases, the charge pump can simply be fabricated alongside other MEMS devices. Before elaborating, it is instructive to first establish how high of a voltage is desired by considering an example application.

5.2 High Voltage Needs

One good example of a MEMS device that benefits greatly from high voltage is the capacitively transduced vibrating RF resonator used in timing oscillators already on the market [54], and targeted for use in next generation wireless communication architectures, such as software-defined cognitive radio [58]. Such devices are attractive for these applications largely due to their unprecedentedly high Q, which now posts over 40,000 at 3GHz [59]. Unfortunately, however, this Q is accompanied by an abysmal coupling coefficient, for which (C_x/C_o) is only 0.000068% with $V_P = 8$V, which translates to a motional resistance $R_x = 81$kΩ many times larger than the 50Ω normally expected by conventional RF circuits.
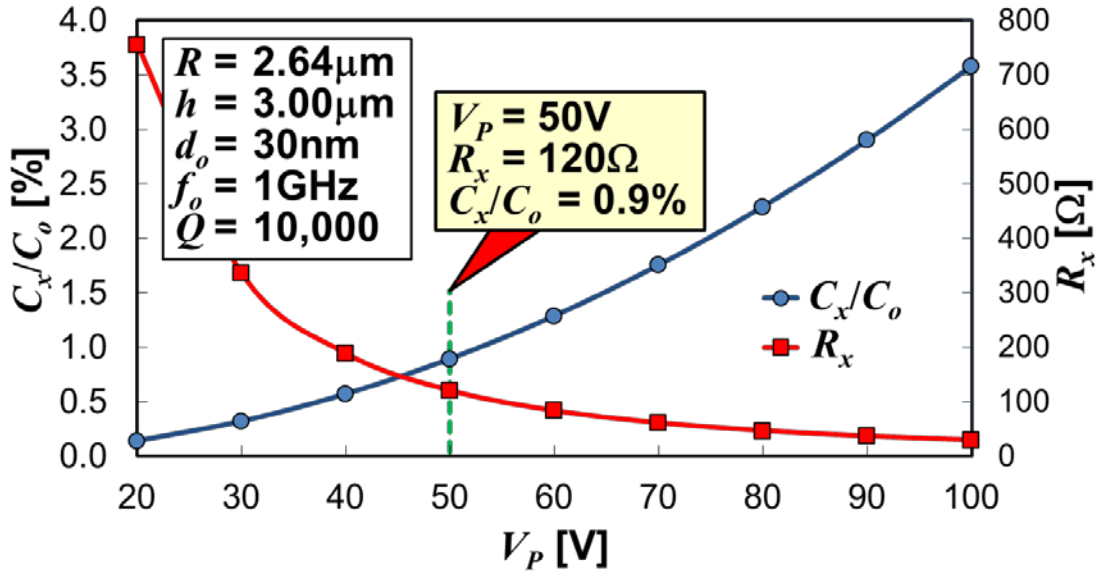
Figure 5-3: Plot of R_x and (C_x/C_o) versus V_P for a 1-GHz radial-contour mode disk resonator.

To explore how high voltage can solve this problem, expressions for the R_x and (C_x/C_o) for the classic radial-contour mode capacitive-gap transduced disk resonator [33] summarized in Figure 5-2(a) can be written as

$$R_x = \frac{\sqrt{k_r m_r}\, d_o^4}{Q \varepsilon^2 A^2 V_P^2} \qquad , \qquad \frac{C_x}{C_o} = \frac{\varepsilon A V_P^2}{k_r d_o^3} \qquad (5.1)$$

where A and d_o are the overlap area and gap between the electrode and disk, respectively; k_r and m_r are the dynamic stiffness and mass of the disk, respectively; and V_P is the dc-bias voltage applied to the resonator. Figure 5-3 uses (5.1) to plot R_x and (C_x/C_o) versus V_P for a 1-GHz disk with a reasonable electrode-to-resonator gap spacing of 30nm, showing how V_P's above 50V allow (C_x/C_o) >1% and R_x's <200Ω, which are on par with values attainable by similarly-sized piezoelectric resonators. If achievable, use of V_P =100V would actually exceed the capabilities of contour-mode d31-transduced AlN piezoelectric devices.

Note that dc-biasing essentially amounts to charging the electrode-to-resonator overlap capacitance. Thus, if a charge pump were employed to provide the charge, it need be turned on only for very short periods, between which the disk can hold its charge (against very small parasitic leakage currents) for time periods on the order of 15mins [61]. If a
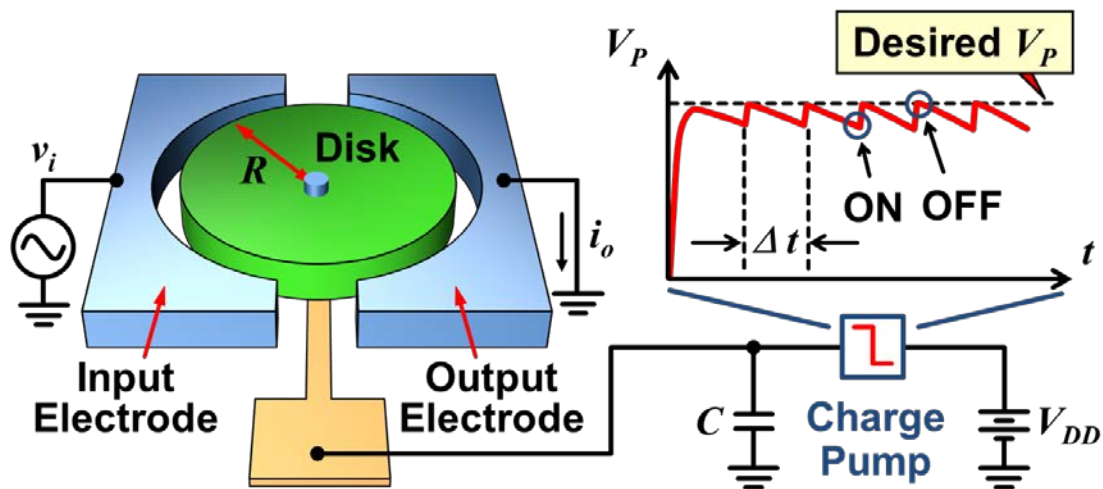
Figure 5-4: Charge-biased disk resonator employing an intermittent charge pumping scheme.

capacitor is placed in parallel with the resonator's bias port, as in Figure 5-4, the refresh time interval can be quite long, e.g., 65 hours for a 0.18μF capacitor [61].

5.3 Micromechanical Resonant Charge Pump

With the inherent advantages mentioned previously, MEMS devices are not surprisingly very promising in power conversion applications. As a result, various efforts of attempting to use MEMS structures in DC-DC power conversion have been made, which can date back to 1990. Such efforts include replacing MOS capacitors with micromachined MEMS capacitors in a power converter circuits [62], using electrostatically actuated MEMS varactors to step-up DC voltages [63], using micromechanical resonant structures in place of the LC tanks and transformers of resonant power converters [64], using micromechanical switches in place of FET diodes in a Dickson's charge pump [65] [66], etc. Unfortunately, most of the previous work stays mainly at the stage of theoretical analysis and no persuasive experimental data has been reported yet in spite of the theoretically proven validity. In fact, the micromechanical voltage multiplier proposed in [66] is actually quite similar to what's been accomplished in this work, however, again, although complete design and detailed process flow were provided, the lack of experimental data compromises the strength of persuasion. In contrast, this work goes beyond theoretical derivation and explores the benefits that MEMS technology can offer to power conversion applications experimentally.

As the first proof of concept, this work first constructed a single stage MEMS Dickson's charge pump, shown in Figure 5-1, which doubles the DC input voltage at the output. Cascaded multiple stages are then demonstrated to generate 3V and 9V from 1V and
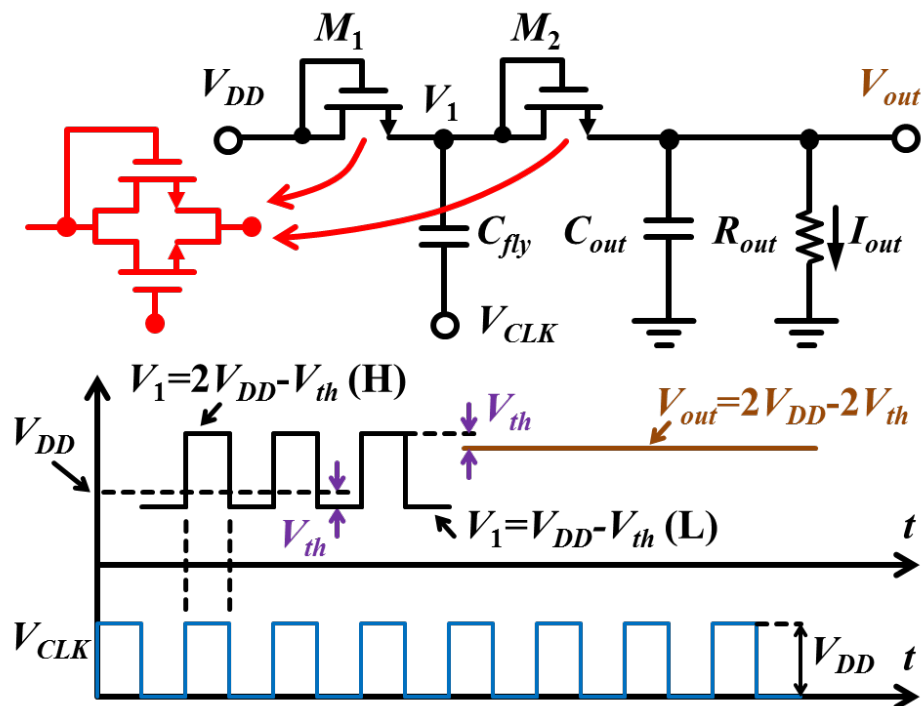
Figure 5-5: Circuit topology of a conventional single stage CMOS Dickson's charge pump and waveforms at each node.

3V power supplies, respectively, using a 2-stage design; and 6V from 1V supply using a 5-stage design; all while avoiding the diode voltage drop and breakdown voltage limitations of conventional CMOS-based charge pumps. Again, the MEMS-based charge pumps demonstrated here additionally accepts a much wider input voltage range than semiconductor technology and obviates the need for custom high voltage CMOS for applications where large voltages are needed, e.g., MEMS-based timing references [54], thereby allowing the use of virtually any CMOS process for a wide variety of MEMS-based products. Furthermore, other topologies besides Dickson's have also been constructed and tested in order for comparison and efficiency optimization. Let's start with Dickson's design.

5.3.1 Dickson's Charge Pump

For comparison with the MEMS version, it is instructive to first consider a conventional Dickson charge pump. Figure 5-5 presents the schematic and waveforms for a classic single-stage CMOS Dickson charge pump, where input DC voltage V_{DD} is fed to two diode-connected MOS transistors in series with the intermediate node V_1 connected to the top plate of a capacitor C_{fly}, with bottom plate driven by a clock signal V_{CLK} toggling between V_{DD} and GND, periodically. When V_{CLK} is at GND, M_1 turns on, and V_{DD} charges
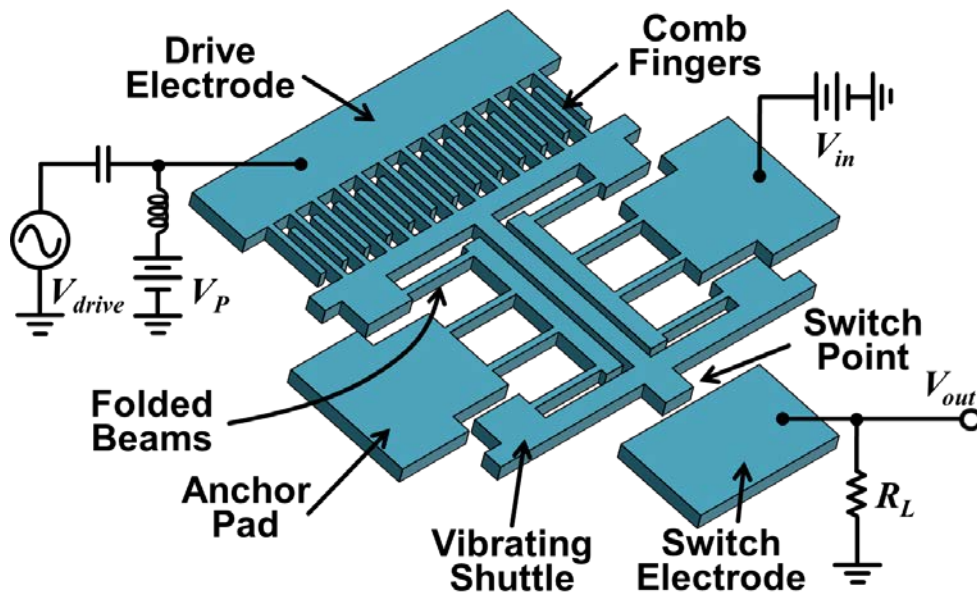
Figure 5-6: Schematic of a comb-driven resoswitch.

C_{fly} until $V_1 = V_{DD}-V_{th}$, where V_{th} is the threshold voltage of M_1 & M_2. Next, when V_{CLK} toggles to V_{DD}, V_1 becomes 2 $V_{DD}-V_{th}$ instantaneously, at which point M_1 is off and M_2 turns on to transfer charge stored on C_{fly} to the output node, resulting in an output voltage $V_{out} = 2V_{DD}-2V_{th}$. When N similar stages are cascaded, the output voltage reaches $(N+1)(V_{DD}-V_{th})$. To eliminate the diode drop term, the MOS diodes in Figure 5-5 can be replaced with pass-gate transistors, such as shown in red, after which the attainable voltage would be $(N+1)V_{DD}$. Ideally any voltage can be generated given enough stages. Unfortunately, in a CMOS charge pump the actual output voltage level is normally limited by the dielectric and p-n junction breakdown voltages of the transistors, e.g. 10-15V in a 0.18μm technology [67]. Custom CMOS technologies, e.g., SOI [57] and triple/deep n-well [53], exist to circumvent this limit, but at the price of higher cost and integration complexity.

Fortunately, more ideal switches provided by MEMS technology enable a more efficient version of the Dickson charge pump. Figure 5-1(a) presents the basic approach using ideal switches. Here, switches SW_1 and SW_2 replace the diodes (or MOS switches) of Figure 5-5. To transfer charge along only one direction, SW_1 and SW_2 must switch on in alternate phases, meaning their turn-on voltages V_{drive1} and V_{drive2} must be on in opposite clock phases. If this is the case, then charge transferred from V_{DD} to V_1 during the clock down cycle gets boosted to $V_{DD}+V_{CLK}$ during the clock up cycle, at which point SW_1 is off and SW_2 turns on to transfer the charge (and voltage) to the awaiting output capacitor. Since there are no voltage drops and the breakdown voltage can be higher than 100V, the output voltage equal to $(N+1)V_{DD}$ can be quite high, indeed.
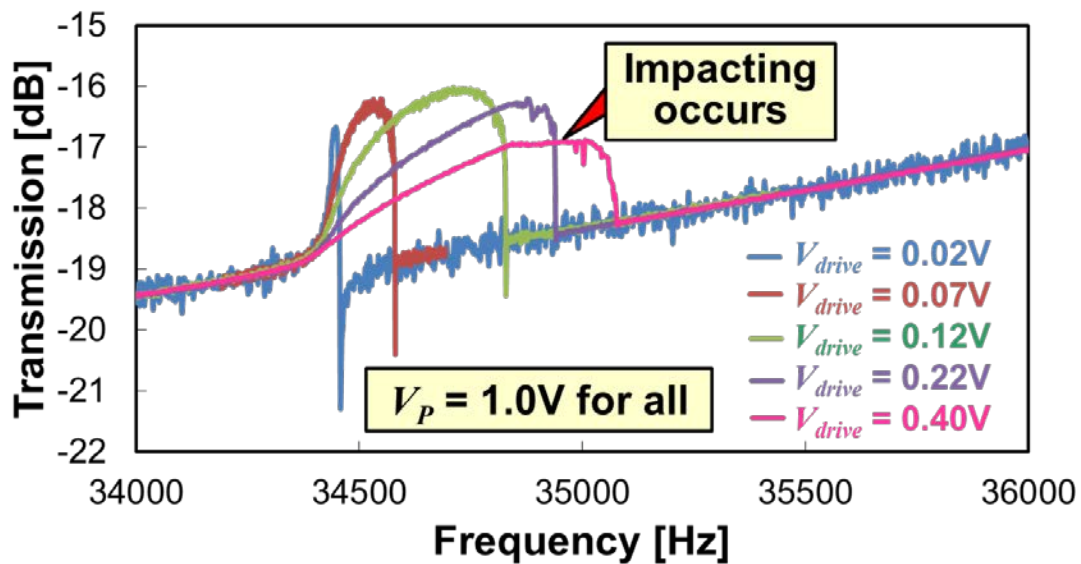
Figure 5-7: Frequency responses of the comb-driven resoswitch measured in vacuum for varying resonance input ac voltage amplitudes, showing impacting when the response flattens.

Unfortunately, there are a few caveats. Specifically, conventional MEMS switches require very large actuation voltages, usually >50V; and they are notorious for their poor reliability, as measured by limited cycle counts before failure. To solve these problems, this work employs resonant micromechanical switches, a.k.a., resoswitches.

5.3.2 Comb-Driven Resoswitches

Micromechanical resoswitches, first described in [68], use resonance operation to greatly improve switch performance. In particular, when at resonance, displacements amplify by Q, so actuation voltages are small even though the stiffness of the device can be quite large. The large stiffness in turn allows very fast operation (due to the high resonance frequency) and very reliable operation, since large stiffness equates to large restoring forces against any sticking phenomenon. To illustrate, Figure 4-20 presents cycle lifetime data obtained for a displacement amplifier version of a polysilicon disk resoswitch [42], which posts 173 trillion hot-switched cycles. The device actually did not fail; rather, its frequency shifted away from that of the drive signal, preventing further impacting.

The resoswitch of [68] and [42] are overkill for the present dc-biasing target application, at least from a frequency perspective. In particular, since a capacitively transduced MEMS device draws practically no current, a very low frequency charge pump is all that is needed. Thus, this work utilizes the much simpler comb-driven resoswitch depicted in Figure 5-6. Here, a folded-beam supported shuttle is capacitively driven into resonance
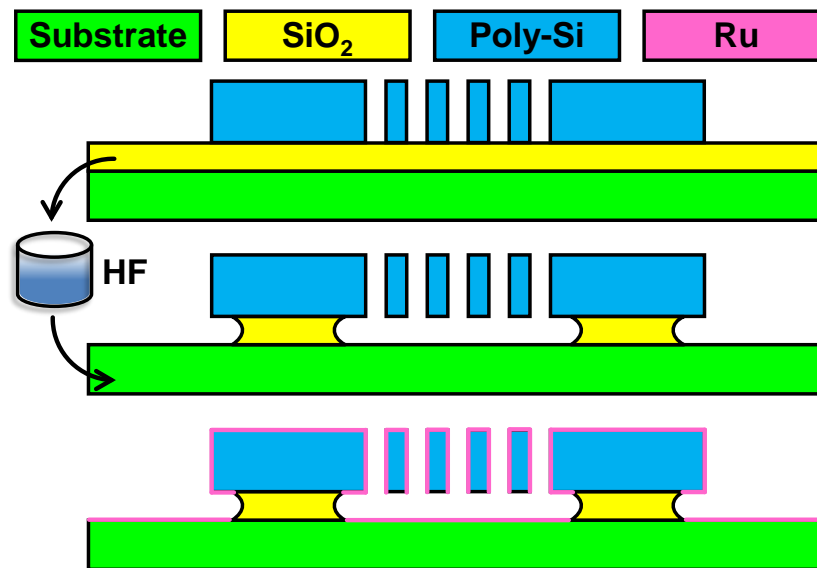
Figure 5-8: Cross-sections summarizing the one-mask process flow used to fabricate comb-driven resoswitches.

by an AC/DC voltage combination applied to comb fingers on one side. The ensuing resonance vibration then induces impacting at the switch point on the other side, which of course periodically opens and closes the mechanical switch. During hot switching, the input DC voltage applied onto the shuttle, is transferred to the output electrode periodically. When operated under vacuum, the voltage amplitude required to actuate this device can be quite small. To illustrate, Figure 5-7 presents measured curves of displacement amplitude versus frequency and drive voltage for a dc-bias of 1V. Here, impacting occurs when the drive voltage amplitude is only 0.4V, which is well under the 1V supply voltage, all enabled by resonance Q amplification.

One advantage of the present comb-driven resoswitch versus previous disk versions is its amenability to fabrication via most traditional MEMS processes, which makes it compatible with a wide array of MEMS products. This work actually fabricates comb-driven resoswitches via the very simple one-mask process summarized in Figure 5-8. Here, 3μm of poly-Si structural layer is first deposited and patterned over a 2μm SiO_2 sacrificial layer. Then the structure is time-released in HF solution, followed by a (not-so-conformal) ALD deposition of 2-5nm Ru. The Ru coating reduces switch contact resistance, which is needed for comb-driven resoswitches since their contact forces are much smaller than those of previous disks. Figure 5-9 presents SEM's of the resoswitch device coated with ALD-Ru.

Figure 5-10 presents measured output waveforms for the resoswitch of Figure 5-6, taking 1V and 0.2V as input voltages, respectively, and showing that with no "diode" drop very small voltages can be transferred by these switches.
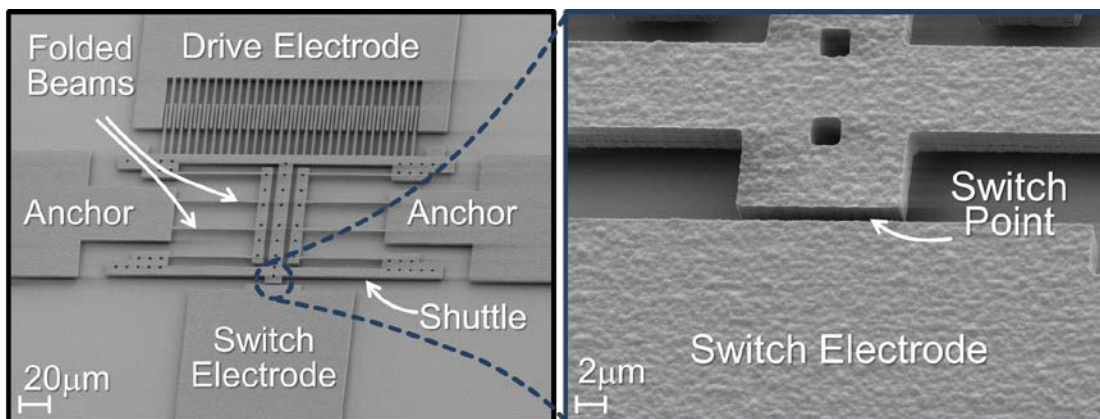
Figure 5-9: SEM photos of a fabricated ALD-Ru-coated polysilicon comb-driven resoswitch.

(a) (b)
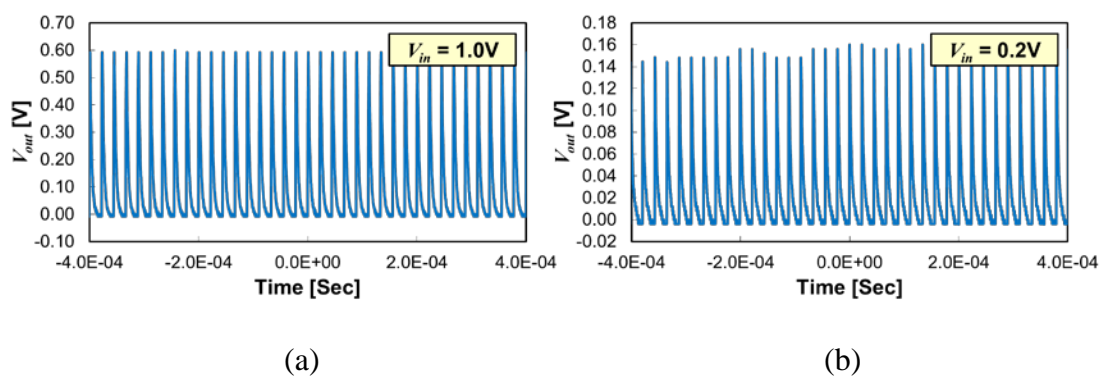
Figure 5-10: Measured oscilloscope output waveforms for the comb-driven resoswitch when operated in the circuit of Figure 5-6 with (a) 1.0V and (b) 0.2V of Vin, respectively.

5.3.3 Gated Sinusoidal Drive

Although this resonant switch provides low actuation voltage and orders of magnitude better reliability than non-resonant ones [68], it does have the apparent drawback that switching occurs only at its resonance frequency. This work overcomes this seeming limitation via use of gated-sinusoids, *cf.* Figure 5-11, top left in the inset, to effectively turn switches "on" and "off" at the period of the gate signal. In particular, during half-cycles where the resonance sinusoid is on, the switch impacts, moving charge from one side to other at its contact interface; and during the off cycle, the switch does not move, so transfers no charge and is effectively "open". Figure 5-11 also plots the measured output signal V_{O1} of a resoswitch ($f_o = 85.8$kHz) driven by the same circuit shown in Figure 5-6 except the AC driving voltage V_{drive1} is now modulated by a square wave gate signal V_{CLK} with a period of 70ms in the way shown in Figure 5-11 inset, where V_{drive1} is active
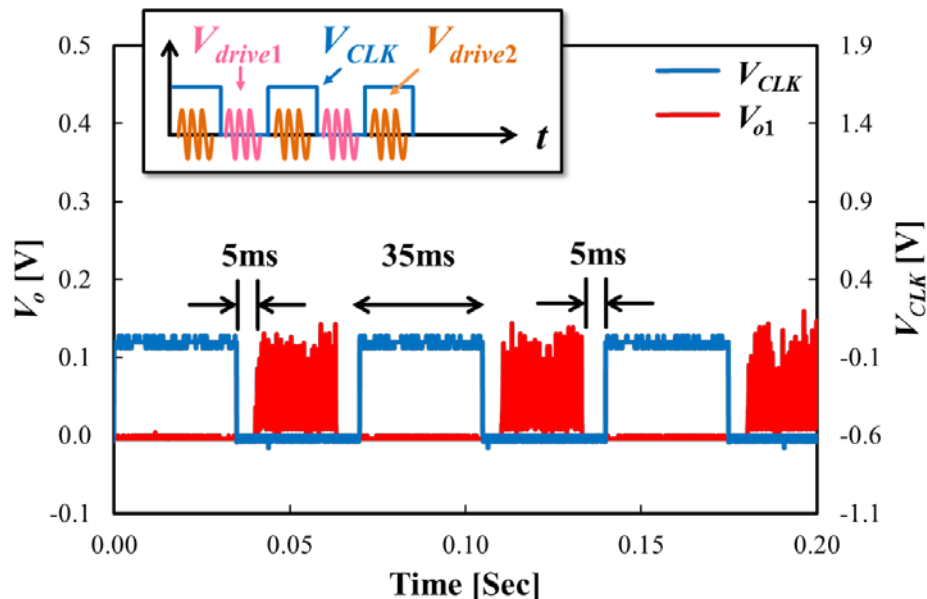
Figure 5-11: The output signal of a resoswitch driven by gated sinusoids.

during when V_{CLK} is low. The output spikes are attenuated from an input DC voltage $V_{in} =$ 0.5V down to around $0.12V_{PP}$ due to a voltage dividing circuit formed by the finite contact resistance and the load resistor $R_L = 10k\Omega$ tied to the output node. Without surprise, output spikes all fall within the time span when V_{CLK} is low, which means the switching only happens during half of each V_{CLK}'s cycles. 5ms trigger delays were inserted before and after the switching cycles to guarantee non-overlap switches.

According to the operation of Dickson's charge pump described previously, to transfer charges in forward direction without back flowing, the two switches used in the charge pump of Figure 5-1(b) needs to be actuated (by V_{drive1} and V_{drive2}) at the same frequency with exact opposite phase. However, with Q's exceeding 10,000 in vacuum, the resonance frequencies of switch 1 and 2 may be so different due to finite fabrication tolerance that AC signals at the same frequency may only be able to drive one of them into resonance switching while the displacement of the other remain tiny. In other words, it would be difficult to drive the two constituent switches into resonance simultaneously and alternatively without trimming them. With gated-sinusoids, switching's of different switches are now controlled and synchronized by V_{CLK}, which means V_{drive1} and V_{drive2} are free of the constraint of being at the same frequency, rather they can be tuned separately to frequencies matching the resonance frequencies of the switches they are driving respectively to obtain maximum displacements. In additions, the gate signal V_{CLK} can serve as the clock driving the bottom plate of C_{fly} and thus no extra clock source is needed. The use of this gated-sinusoid excitation stands to revolutionize the use of resonant switches, since it removes the previously cumbersome restriction to resonance!
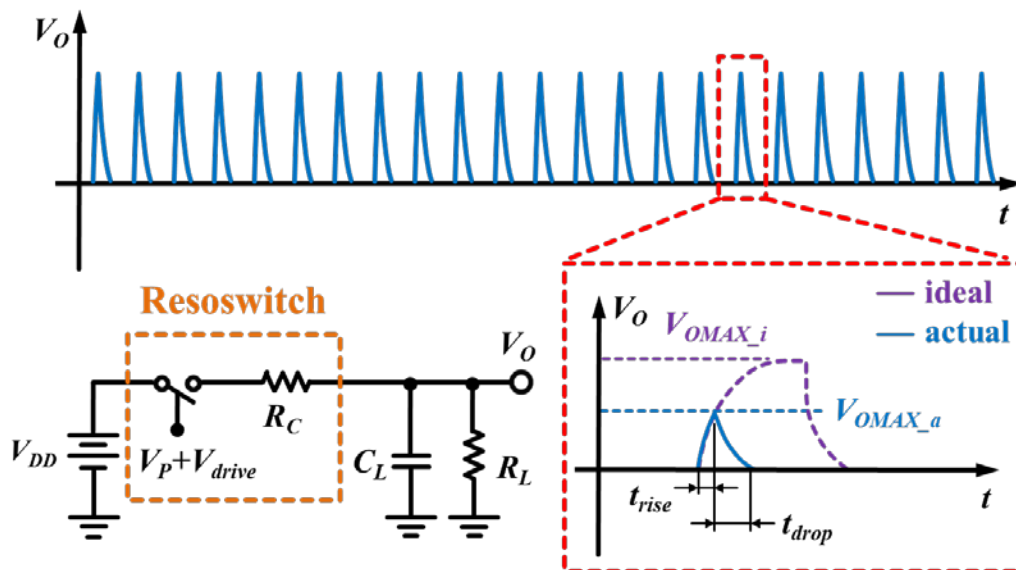
Figure 5-12: Simplified equivalent circuit of a comb-driven resoswitch shown in Figure 5-6 and expected output waveform with zoom in on the shape of each spike.

5.3.4 Suppress of Squegging

There are imperfections in the MEMS-based Dickson's charge pump shown in Figure 5-1. In particular, it has used gated-sinusoid excitation signals to synchronize the movement of charge through the pump topology and to overcome difficulty with squegging—a phenomenon where an oscillation amplitude is not constant, but rather grows and shrinks with a certain period [69], as shown (later) in Figure 5-17. This section explores contact engineering to overcome squegging and ultimately uses a Pt-silicide-based contact interface to greatly reduce impact-induced energy loss in resoswitches to the point where squegging phenomena are eliminated, so no longer constrain the clock frequency of recently demonstrated mechanical charge pumps. This opens the application range of such charge pumps to power converters capable of delivering currents much higher than the low current-draw MEMS dc-biasing applications previously targeted by [70].

To explain squegging in the subject resoswitch, review of device structure and operation is in order. The operation of the comb-driven resoswitch is simple and shown for the device of Figure 5-6: Drive the capacitive combs with a combined (dc-bias + resonance ac) voltage hard enough to affect impacting, in turn closing a mechanical switch that then periodically transfers charge from the supply V_{in} to the awaiting load (R_L or C_L) at the output. Figure 5-12 presents the equivalent circuit for the hookup of Figure 5-6, where R_C is a combination of interconnect resistance and switch contact resistance (but dominated by the latter). The expected normal output waveform from this comb-driven resoswitch is also shown to be a series of spikes shaped by the RC circuit formed between R_C, R_L and
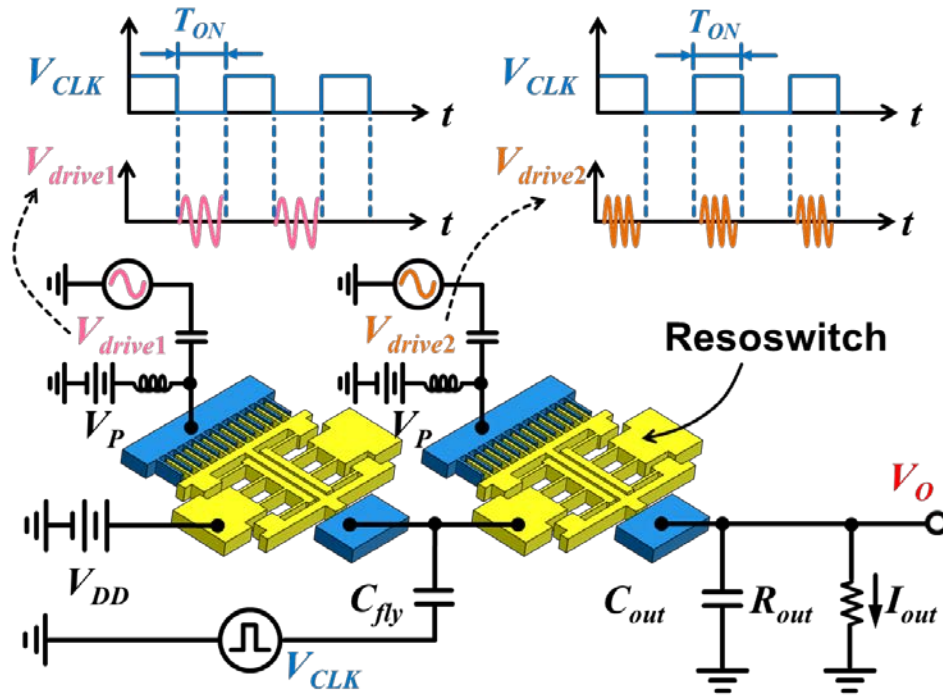
Figure 5-13: Schematic of a single-stage MEMS Dickson's charge pump and gated-sinusoid waveforms needed to affect synchronized pumping.

C_L. The governing expression from which the contact resistance R_C can be extracted takes the form

$$\frac{V_{DD} \cdot R_L}{R_C + R_L} \cdot \left(1 - exp\left(-\frac{t_{rise}}{(R_C||R_L)C_L}\right)\right) = V_{OMAX\_a} \qquad (5.2)$$

where t_{rise} is the charging time of the spike, i.e., the switch contact time; and V_{OMAX_a} is the measured spike amplitude.

In the actual charge pump application, shown in Figure 5-13, the waveforms required to actuate the devices are actually gated sinusoids rather than pure ones. This is a consequence of finite tolerances achievable via planar microfabrication that produce resoswitches with slightly different resonance frequencies. Because of this, the devices cannot be actuated simply by a single signal at one frequency phase shifted to service different pumping phases. Rather, each device requires a different frequency to affect resonant switching. To synchronize impact-based charge transfer events, gated sinusoids tailored to the resonance frequency of each individual device are needed, as illustrated in

Figure 5-13. Here, impacting charge transfer occurs only during periods when the gate is "on". The amount of charge transferred is a function of the total time of impact, i.e., during which the shuttle and electrode are in contact, which for the low frequency design of the present discussion, is generally only a small fraction of the resonance period, as shown in Figure 5-12. Indeed, one of the factors that sets the needed "gate-on" period in a charge pump is this impact residence time.

Ultimately, the other factor governing the "gate-on" time is squegging. As mentioned, squegging refers to a phenomenon where an oscillation amplitude is not constant, but rather grows and shrinks with a period [69] governed by the degree to which losses vary with time. For the resoswitch device, the loss in the system rises abruptly from its free vibration value once impacting occurs, during which each impact steals an amount of energy from the system governed by the elasticity of the impact. Squegging occurs when the energy stolen on impact is large enough to reduce the amplitude of motion so that no impact occurs on the next cycle(s). Rather, energy must build up towards another impact, after which energy is lost again, and the cycle continues with a period essentially governed by impact loss.

Of course, a squegged waveform, generates fewer impacts per "gate-on" period T_{on}, thereby requiring a longer T_{on} for a given amount of charge transfer and a smaller pumping frequency. This in turn means less pumping ability, so smaller current (or power) delivery to a load, i.e., squegging compromises the ultimate power delivery of a power converter. Thus, the power delivery capability of a MEMS-based charge pump (or other power converter type) cannot be maximized unless squegging is eliminated.

5.3.4.1 Squegging Model

The energy loss per impact can be modeled by the restitution law governing the relationship between velocity before and after impact: [69]

$$dx/dt \mid_{after\ impact} = -r \cdot dx/dt \mid_{before\ impact} \tag{5.3}$$

where x is displacement, and $r<1$ is the coefficient of restitution, governed largely by the contact material interface. Loss of velocity after impact, of course, means loss of kinetic energy, and the more energy lost per impact, the longer it takes to recover, and the larger the number of non-impact cycles during squegging. From (5.3), squegging is minimized via use of materials with higher hardness, i.e., less plastic deformation when impacting, for which r is closer to 1. In this regard, polysilicon is preferred over most metals. Polysilicon alone, however, is too resistive; but a polycide that combines polysilicon and a metal makes good sense.

The squegging behavior of the resoswitch can be captured theoretically by solving a group of ODE's consisting of (5.3) and the equation of motion (2.6). Before solving the
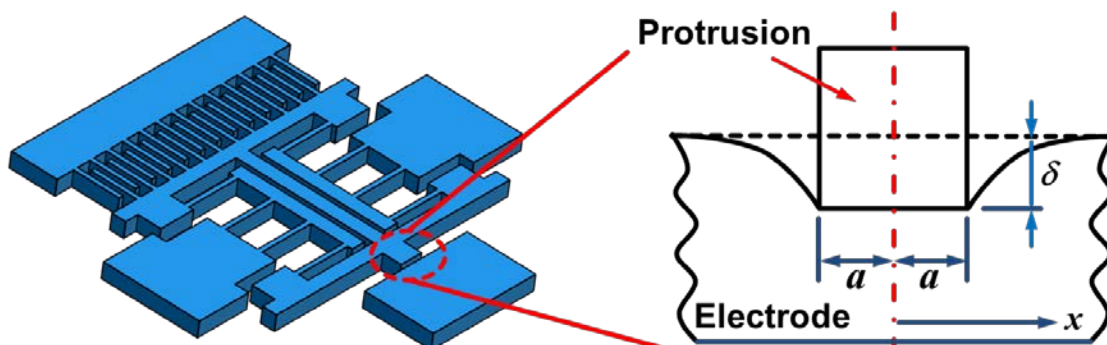
Figure 5-14: Model of a comb-driven resoswitch contact.
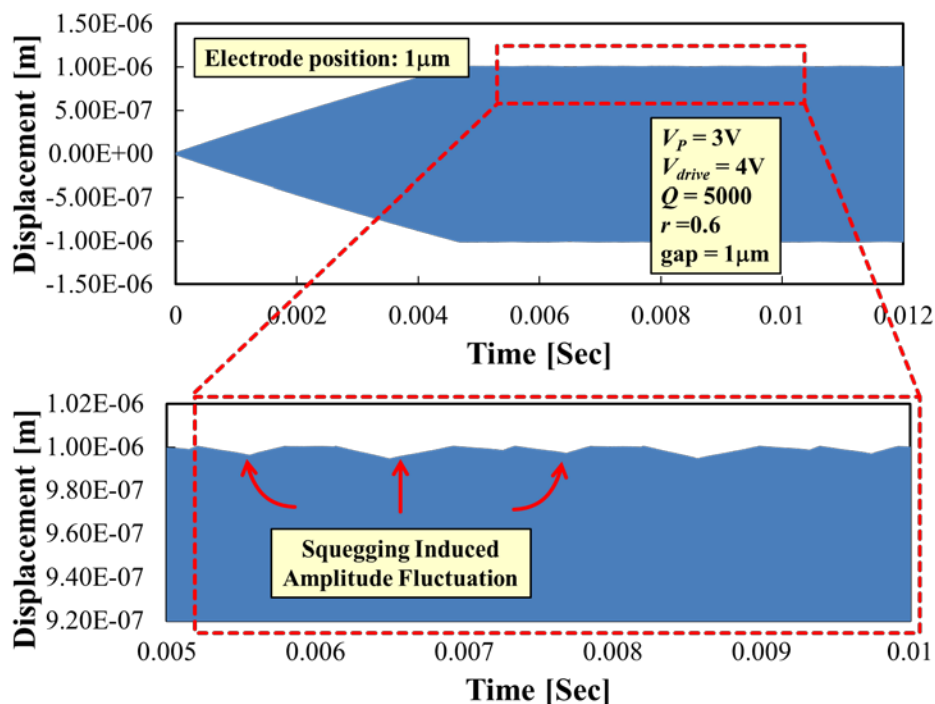
Figure 5-15: Theoretically simulated resoswitch shuttle displacement by solving (5.3) and equation of motion numerically in MATLAB.

equations, the contact stiffness $k_{contact}$ needs to be determined. Unlike the clamped-clamped beam switch, the contacts of a comb-driven resoswitch can be modeled as the indentation of a rigid flat punch into an elastic half space as shown in Figure 5-14 [29]. Figure 5-15 shows the simulated shuttle displacement with the parameters summarized in the inset table, where a fluctuation of displacement amplitude is clearly observed.

Simulation also reveals that besides choosing harder structural materials, careful me-
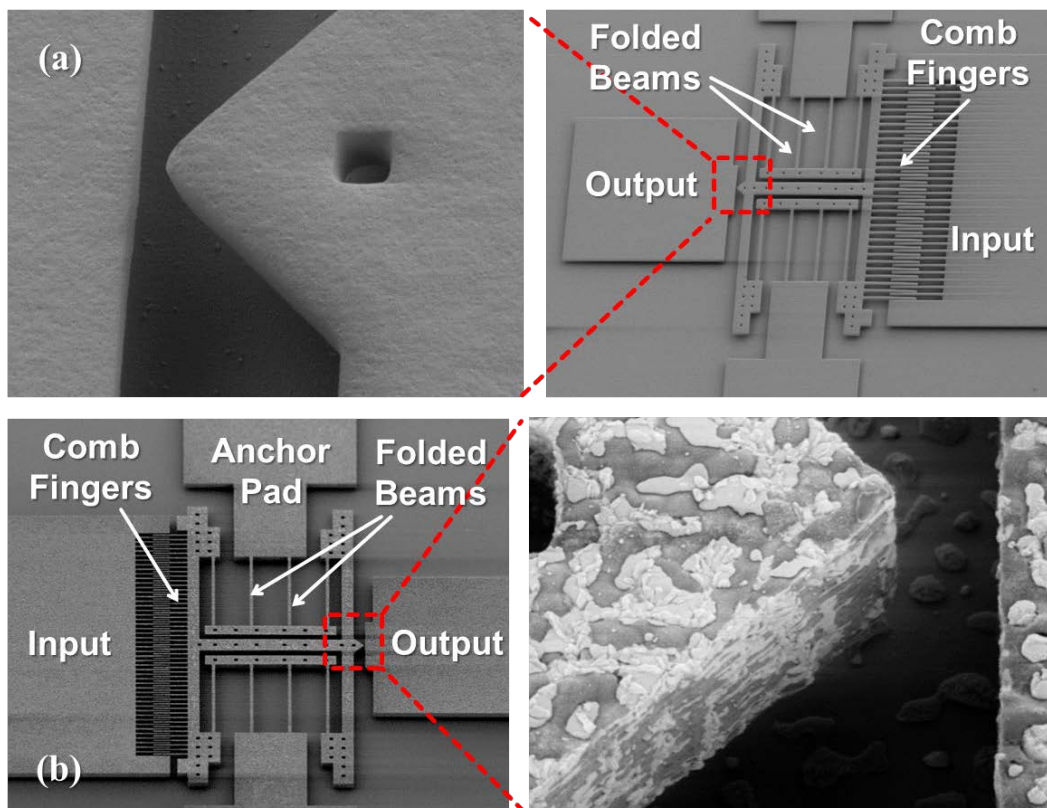
Figure 5-16: SEM photos of (a) the comb-driven resoswitch using electroplated Ni as structural material with sputtered Ru covering contact interfaces and (b) the poly silicon resoswitch with Pt-silicide covering the entire structure.

chanical design can also suppress squegging. For instance, reducing switch gap constrains the system to smaller displacements, so smaller energy deficits to recover after lossy impact, hence, less squegging. In addition, locations of electrodes relative to the contacts can affect squegging. As mentioned, placement of comb electrodes on the same side as the contact allows the electrode-generated force to drive the shuttle into the contact point, so adds to the impulsive impact force, making for more efficient energy recovery. In contrast, having drive electrodes and contacts on the opposite sides relies on less efficiently generated moment forces when contacting, so displays much more simulated squegging.

5.3.4.2 Fabrication Processes

Pursuant to gauging the influence of contact interface design on squegging, comb-transduced resoswitches were realized in various materials with various contact interfaces. These include electroplated nickel devices coated with Ruthenium to serve as soft contact resoswitches; and polycide devices to serve as hard contact ones. All devices utilized
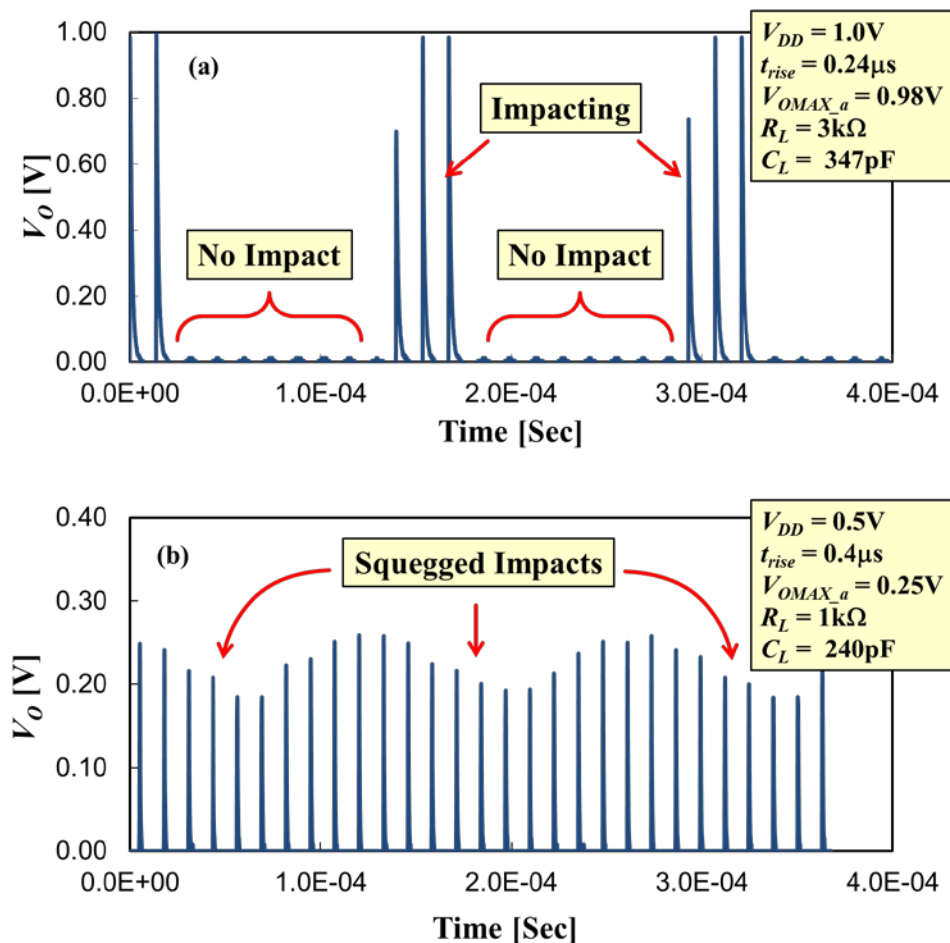
Figure 5-17: Squegged output waveforms of the (a) Ni/Ru and (b) PtSi resoswitches tested using the circuit of Figure 5-6. Here, both resoswitches had switch axis gaps of 1000nm.

simple one-mask surface-micromachining fabrication process flows, such as used in [70], where oxide mesas that remain after a timed release etch serve as anchors for suspended structures. Ni/Ru device fabrication is rather straightforward, comprising a molded Ni electroplating above an oxide spacer, followed by subsequent release and coating with 10-20nm of Ru via sputtering, which was found to be sufficiently conformal to coat the sidewalls of the structures. Figure 5-16(a) presents SEM's of a Ni/Ru device.

Polycide devices were achieved by first fabricating one-mask polysilicon device, coating them with 25nm of Pt via atomic layer deposition (ALD), then RTA annealing for 3mins to form platinum polycide. The polycide forms only over polysilicon, allowing simple removal of unreacted Pt over oxide mesa sidewalls via liquid regia. The end result is a polycided resoswitch that actually sports a lower contact resistance than the Ru-

coated polysilicon devices of [70], since the polycide layer actually ends up being thicker than [70]'s 2-5nm Ru coating. Figure 5-16(b) presents SEM's of the polycide device. Here, somewhat non-uniform silicidation [71] over the polysilicon surface does increase the contact resistance over what could have been, but still delivers sufficient conductivity for charge pumping of MEMS devices.

5.3.4.2 Experimental Verification

Figure 5-17(a) and (b) present voltage output waveforms for the fabricated Ni/Ru and PtSi resoswitches, respectively, when driven hard enough to impact across 1000nm switch gaps. Clearly, the softer Ni/Ru contact interface induces considerable squegging, where periods of no contact are clearly visible. On the other hand, the polycide device displays much less squegging and appears to make contact at all times, although some impacts are less forceful than others, so achieve larger contact resistances, hence, slightly lower output voltages. Using (5.2) with the parameters summarized in Figure 5-17, the contact resistances are found to be 49Ω and 870Ω for the Ni/Ru and PtSi devices, respectively. These are larger than desired for high power converters, but are comfortably sufficient for low power, high voltage charge pump applications, like MEMS dc biasing.

Figure 5-18 presents the measured output waveform from a resoswitch identical to that of Figure 5-6, but with a smaller switch gap of only 500nm. Here, the smaller gapped device exhibits much less squegging, in agreement with simulation. Figure 5-19 further shows that placement of actuating comb fingers on the same side as output electrode suffers less squegging than configuring them on opposite sides.

The reduction of squegging demonstrated here not only solves an important issue with resoswitches that previously constrained the operation frequency of charge pumps using them, but also identifies polycides or silicides as compelling contact interfaces. Although the use of a polycide contact yielded a rather high contact resistance for the low frequency switches demonstrated here, higher frequency disk-based resoswitches, such as demonstrated in [37], should exhibit much smaller resistances, since their impact force is much larger. With high frequency, no squegging, and potentially good contact resistance, disk resoswitches using polycide material might just fit the bill for their targeted power amplifier and converter applications.
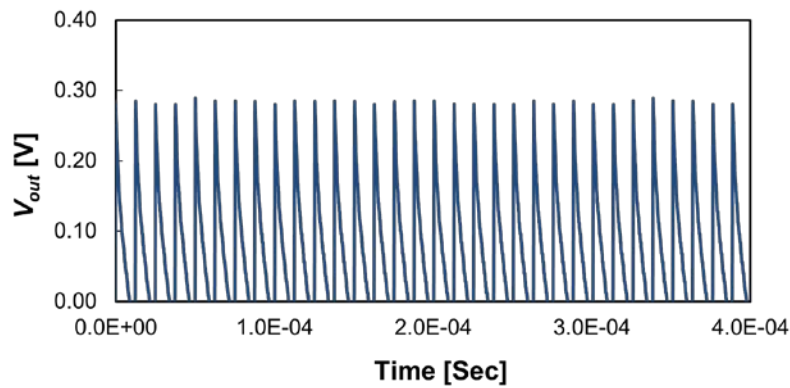
Figure 5-18: Output waveform of the PtSi resoswitch with a 500nm lateral switch gap showing much less squegging induced amplitude fluctuation.
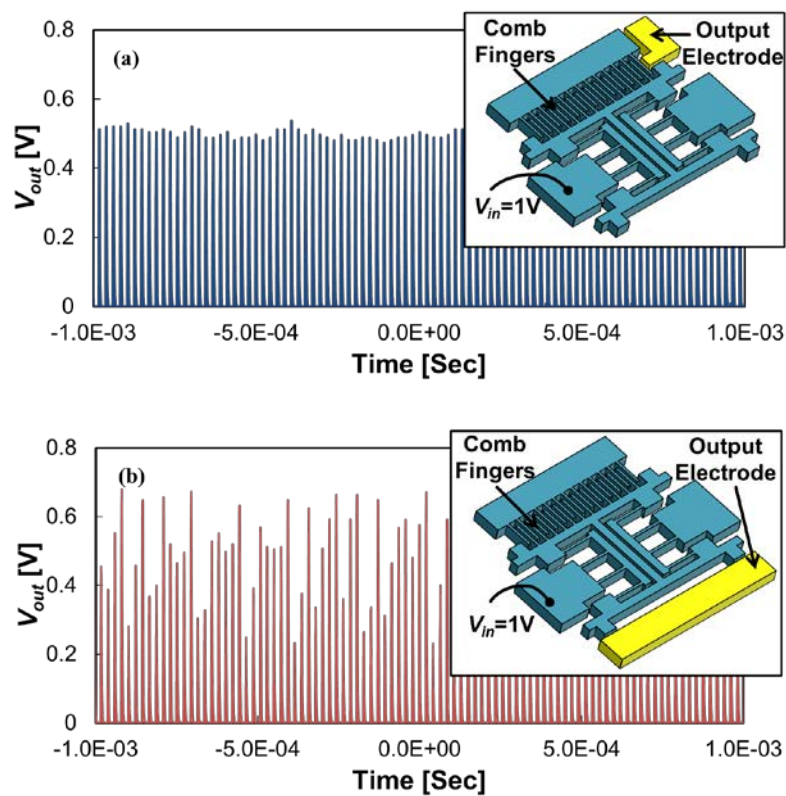
Figure 5-19: Output waveforms of the PtSi resoswitch with output electrode placed on (a) the same side and (b) opposite side of the actuating comb fingers.
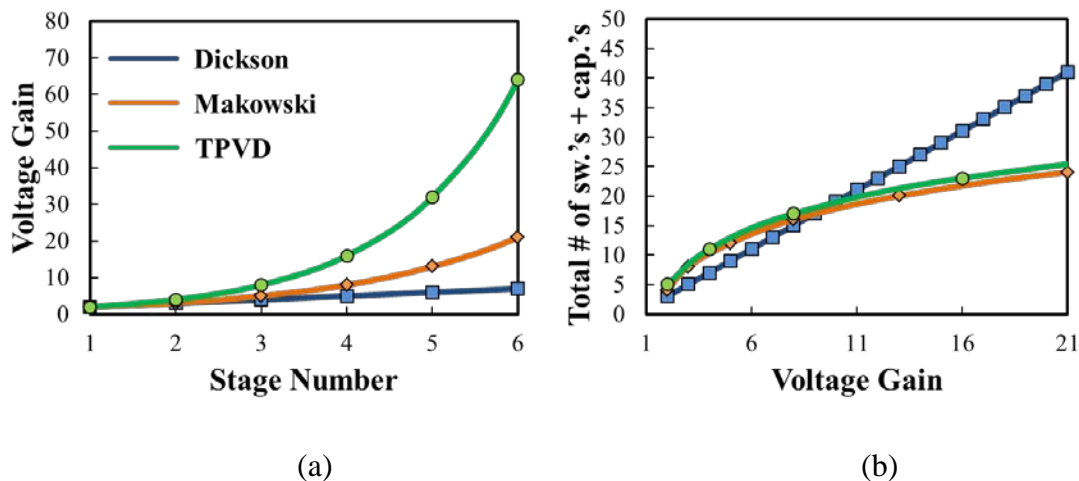
Figure 5-20: (a) Voltage gain as a function of stage number and (b) total amount of needed charge transfer switches and pumping capacitors as a function of voltage gain for Dickson's, Makowski's and two-phase voltage doubling charge pumps.

5.3.5 Switched Capacitor Voltage Doubler

While Dickson's charge pump is the most widely used topology, it has some inherent drawbacks. First of all, the voltage gain, numbers of switches and capacitors of Dickson's design all increase linearly with number of stages N. With this slow growth of voltage gain, the charge pump would need more stages especially when high output voltages (e.g. 50-100V) are desired. And it costs more and more area as well as pumping energy, which is related to the numbers of capacitors and switches used, for increasing number of stages. Secondly, since more charge transfer switches and pumping capacitors are needed, there tends to be more series resistances and stray capacitances, which consume extra charges and degrade the pumping efficiency in the end. Regarding solving these issues, other types of charge pumps have been developed including switched capacitor voltage doublers [72]. Figure 5-20 compares the voltage gains as a function of stages and numbers of capacitors as a function of voltage gains of various kinds of charge pump topology. Apparently, as the number of stages increases, voltage gain growth of Dickson's design is relatively slow and for the same desired voltage gain it requires much more capacitors. Therefore, besides Dickson's design, this work also explores the possibility of implementing switched capacitor voltage doubler using MEMS resoswitches.

Figure 5-21 shows the schematic of a single stage switched capacitor voltage doubler designed and demonstrated in this work, which actually mimics Makowski's design [72] and replaces the MOS switches with micromechanical comb-driven resoswitches. The four switches RSW_{1-4} are separated into two groups driven in opposite phases, Φ and $\bar{\Phi}$, respectively. When $\Phi = 1$, RSW_1 and RSW_2 both turn on connecting top and bottom plates of C_{fly} to V_{DD} and GND at the same time and charging V_1 to V_{DD}. And when $\Phi = 0$, RSW_{1-}
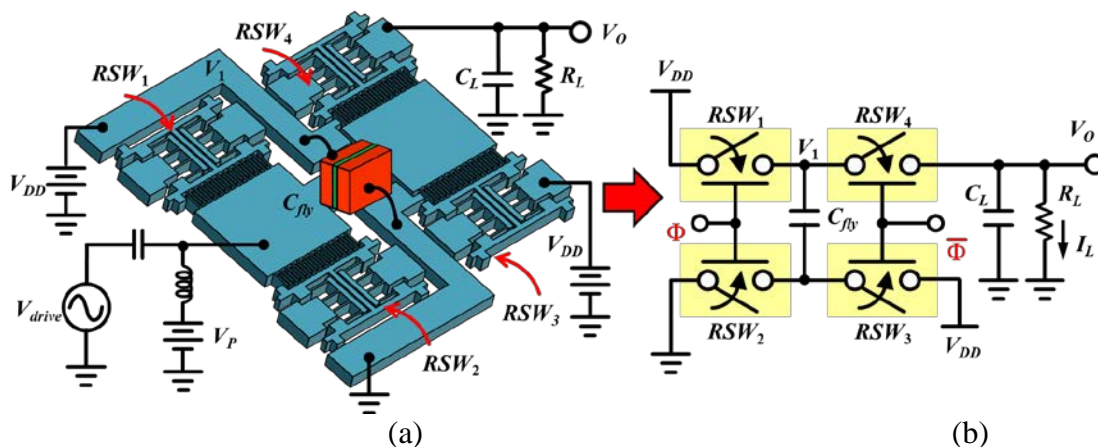
Figure 5-21: (a) Schematic of a single stage micromechanical switched capacitor voltage doubler and (b) the equivalent circuit topology.
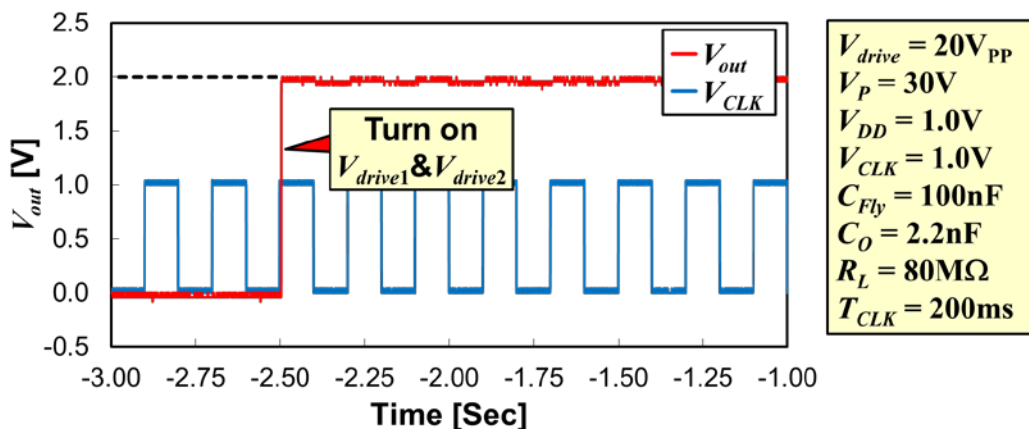
Figure 5-22: Measured oscilloscope output waveform of the single stage micromechanical charge pump together with the clock signal controlling gated-sinusoids.

$_2$ turn off and RSW_{3-4} turn on connecting bottom plate of C_{fly} to V_{DD} and toggling V_1 to $2V_{DD}$ instantaneously. This doubled DC voltage of V_1 is then transferred out to the output load through the closed RSW_4. When N such stages are cascaded, an output voltage equal to the $(N+2)$th Fibonacci number times of V_{IN} can be obtained.

In theory, two out-of-phase AC signals are needed to drive RSW_{1-2} and RSW_{3-4} separately, but in reality only one AC source is used as shown in Figure 5-21(a) thanks to the clever mechanical design. To be more specific, the switch contact bumps of RSW_{1-2} are designed to be all on the opposite side of the comb fingers while those of RSW_{3-4} are on the same side. Therefore, when all driven by the same solo V_{drive}, the vibration of the four shuttles are synchronized and the mechanical impacts of RSW_{1-2} ensue simultaneously
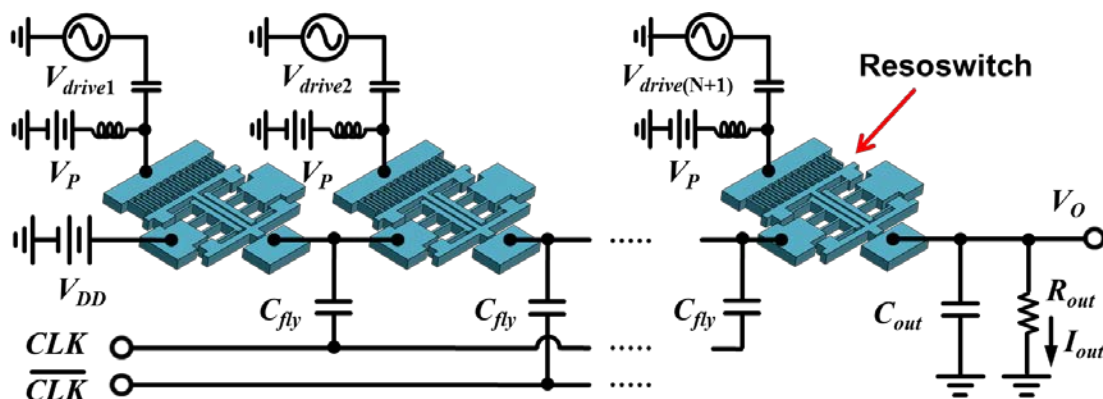
Figure 5-23: Schematic of an *N*-stage MEMS Dickson's charge pump.
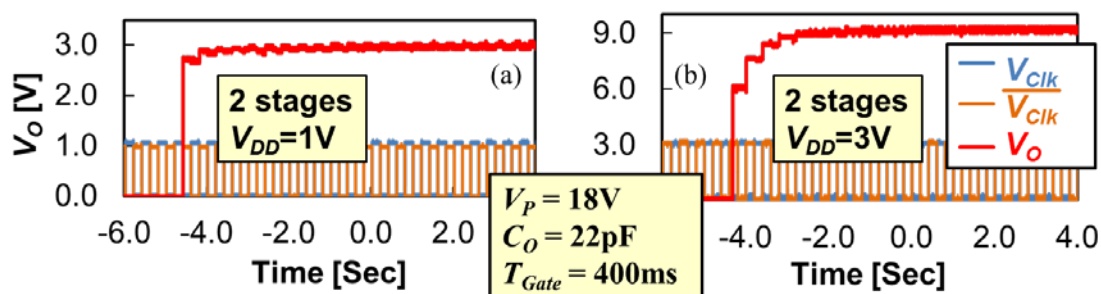
Figure 5-24: Output waveforms of a 2-stage MEMS charge pump with (a) 1.0V and (b) 3.0V input voltages, both showing 3× voltage boosts.

while differing from those of RSW_{3-4} by 180°. V_{drive} needs not to be gated by V_{CLK} when tested in the air, where the Q's of the resonant devices are loaded heavily by air damping and the resonance spectra can thus spread out wide enough to overlap with each other such that signal of single frequency is sufficient to drive all the switches into resonance.

5.3.6 Measurement Results of Charge Pumps

Using the comb-driven resoswitches described above, a Dickson charge pump was built mimicking the circuit topology of Figure 5-1(a), but with a few modifications shown in (b) and Figure 5-22 finally presents the output voltage wave-form it, where a 1V input has been successfully boosted to 2V at the output. And of course, as more resoswitch-capacitor stages are added, the charge-pumped voltage increases. This result, however, was obtained not in vacuum but in the air instead to avoid the difficulty in testing brought by impact induced frequency instability (squegging) in vacuum. And due to the much lower quality factors of comb-driven folded beam structure in the air, ~50 compared to 10,000-50,000 in vacuum, the driving voltages needed are much higher. Therefore, for the result shown in Figure 5-22, $V_P = 30$V and $V_{drive} = 20$V$_{PP}$ are used. And since the wir-
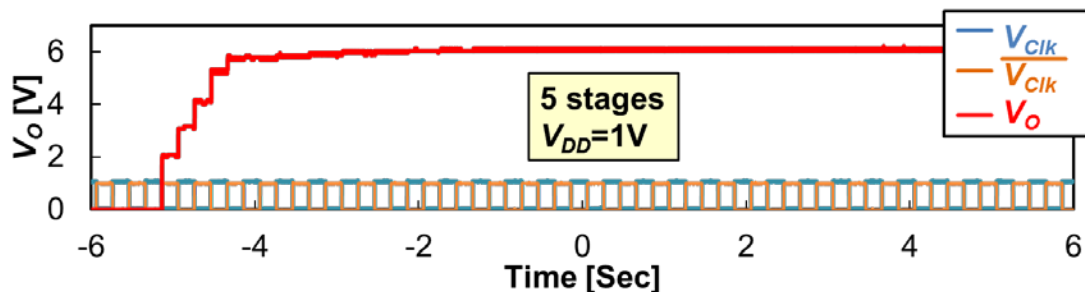
Figure 5-25: Output waveforms of a 5-stage MEMS charge pump with 1.0V input voltage indicating a 6× voltage boost.
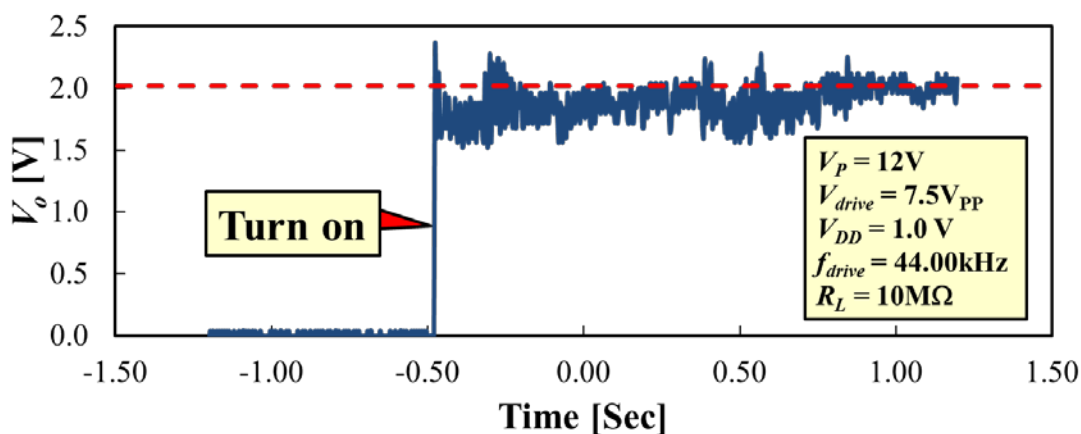
Figure 5-26: Output waveform of a single stage voltage doubler shown in Figure 5-21.

ing are performed on a breadboard, a C_{fly} as big as 220nF has to be used in order to overcome the large stray capacitance and reduce the charge loss to maximize the voltage gain. A load R_L = 80MΩ and C_L = 2.2nF is used to simulate the large isolation resistance [61] and shunt capacitance of the electrostatic resonators the charge pump intends to bias. The detailed driving conditions are summarized to the right of the waveform.

Figure 5-23 shows the schematic of *N*-stage micromechanical Dickson's charge pump and Figure 5-24 presents output waveforms of a 2-stage charge pump, showing boosting of 1V and 3V supply voltages by 3×, to 3V and 9V, respectively. Again, these measurement results were all taken in the air with similar driving conditions to the single stage case with differences summarized in Figure 5-24. Figure 5-25 presents the output waveform of a 5-stage charge pump that pumps the 1V supply voltage to 6V. Given *N* stages, the output voltage level can very simply be calculated using (5.4):

$$V_O = V_{DD} + N \times V_{DD} = (N+1) \times V_{DD} \tag{5.4}$$

Figure 5-26 shows a single stage Makowski's switched capacitor voltage doubler that boosts 1V of V_{DD} to 2.0V. The constituent switches are designed to be exactly the same and resonating at f_o = 44kHz due to a more flexural folded beam design (L=40μm, W=1μm). The lower resonance frequency and a smaller switch gap, 0.5μm compared to 1μm for switches used in Dickon's version, all lead to a smaller required driving voltages as also indicated in Figure 5-26. If this scaling keeps going and combine some other scaling techniques, e.g. increasing number of fingers, reducing comb-finger gaps, etc., the required V_P and V_{drive} are very likely to be reduced to below 1V even in the air ambient.

5.4 Conclusions and Future Work

This work demonstrates a micromechanical Dickson charge pump employing comb-driven resonant switches to boost 1V of V_{DD} to 2V with single stage. By cascading multiple single stages, the charge pump successfully boosts supply voltages by 3× and 6× using 2-stage and 5-stage designs, respectively. By removing the diode drop and junction breakdown issues of conventional transistor implementations, this MEMS-based charge pump can transfer charge with any input voltage level and can actually achieve ultra-high voltages needed by MEMS devices—something that becomes exponentially more difficult as CMOS continues to scale. Besides Dickson's topology, this work also explores the prospect of building other types of charge pump using MEMS resoswitches that potentially will be more area and power efficient than the traditional Dickson's design. In particular, a single stage Makowski's switched capacitor voltage doubler has been demonstrated that doubles 1V of V_{DD} to 2V.

In doing so, this mechanical circuit opens a path towards much higher voltages attained by merely utilizing more charge pumping stages—something easily done right next to a given MEMS device, using virtually the same fabrication process sequence that achieved that MEMS device. By raising voltages directly on the MEMS chip, this mechanical charge pump greatly improves MEMS device performance, while simultaneously lowering cost by obviating any need for (expensive) custom high voltage CMOS processes. But perhaps the most important contribution here is psychological: With this technology, MEMS designers need no longer put limits on permissible voltage levels. It would be wonderful if this new-found freedom inspires new designs and capabilities previously unthinkable.

There are some unsolved issues. First of all, the measurement should have been performed in vacuum in order to fully harness the benefits of resonance switching. However, to overcome the more significant squegging induced frequency shift in vacuum, instead of the current open loop driving, a closed loop oscillatory driving, similar to the one shown on Figure 4-21, may be needed. Second, the charge pump circuits would be even more power efficient when implemented on a PCB board or eventually on chip, where stray capacitances are much smaller than those currently on the breadboard. When all switches, capacitors and routings are integrated entirely on chip, the MEMS charge pump demonstrated in this work can be used to bias any MEMS devices conveniently.

CHAPTER 6 *Micromechanical Resonator Frequency Repeatability*

With Q's over 150,000 at VHF [12] and over 15,000 into the GHz range [33], plus demonstrated aging and drift stabilities suitable for low-end timing products that are now entering consumer electronics markets [54], vibrating micromechanical resonator technology has garnered considerable momentum and now targets higher-end markets, such as communication-grade filters and oscillators for wireless handsets. Applications like these, however, tend to rely more heavily on the sheer performance of the resonators they use. Since resonator performance is a statistical quantity, the success of a higher-end product often depends more on the degree to which the manufacturing process can consistently achieve a specific frequency and maintain a Q above a certain threshold. Regarding the main focus of this dissertation, frequency and Q repeatability is also crucial for MEMS-based charge pump implementation, because eventually a single frequency source needs to be able to drive all the constituent switches into impacting whose resonance frequencies are designed to match with each other. Therefore, statistical studies in this chapter are instrumental for future charge pump designs.

6.1 Effect of Electrode Configuration on f_o & Q Repeatability

A statistical evaluation of the standard deviations of the resonance frequencies and quality factors of polysilicon surface-micromachined micromechanical disk resonators with fully-surrounding and split electrode configurations has been conducted by fabricating and measuring a large quantity (>400) of devices. Through this analysis, respective single-wafer resonance frequency standard deviations as low as 642 ppm for fully-surrounding electrode devices; and 984 ppm for two-port split electrode devices; have been measured. Respective average quality factor standard deviations for fully surrounding electrode devices of 5.6% in vacuum; and 3.9% in air; have also been obtained. The standard deviations for both frequency and Q of each resonator type are well within values needed to achieve the ~3% percent bandwidth requirements for filters presently used in the RF front-ends of wireless communication devices without trimming.

Pursuant to better understanding the breadth of applications accessible to untrimmed vibrating micromechanical resonator technology, this work compiles a sufficient volume
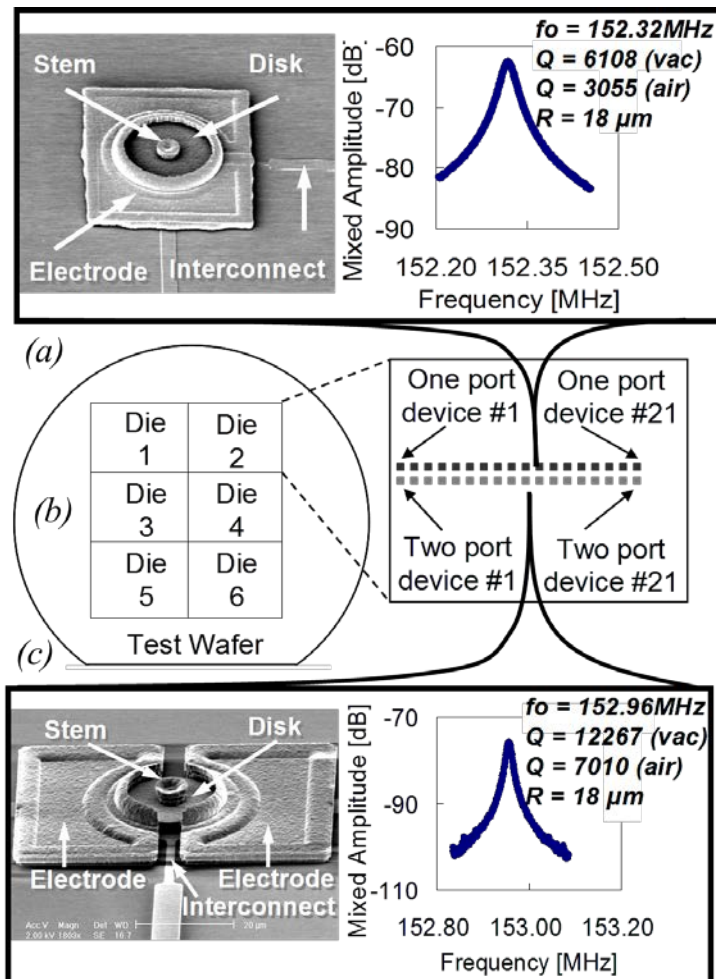
Figure 6-1: SEM's and measured frequency characteristics of fabricated disk resonators with a) a fully surrounding one-port electrode; and c) a split two-port electrode. b) Test die and device location.

of data to determine the statistical repeatability with which VHF micromechanical contour-mode disk resonators can be manufactured via the self-aligned stem sacrificial-sidewall gap surface-micromachining process of [33]. Through this analysis, respective single-wafer resonance frequency standard deviations as low as 642 ppm for fully surrounding electrode devices; and 984 ppm for two-port split electrode devices; have been measured. This data is much more substantial than that of [73], which included only fully-surrounding electrode data, and which did not include quality factor or air versus vacuum data. Respective average quality factor standard deviations for fully surrounding electrode devices of 5.6% in vacuum; and 3.9% in air; have also been obtained. The standard deviations for both frequency and Q of each resonator type are well within values needed to achieve the ~3% percent bandwidth requirements for filters presently used in the RF front-ends of wireless communication devices without trimming.
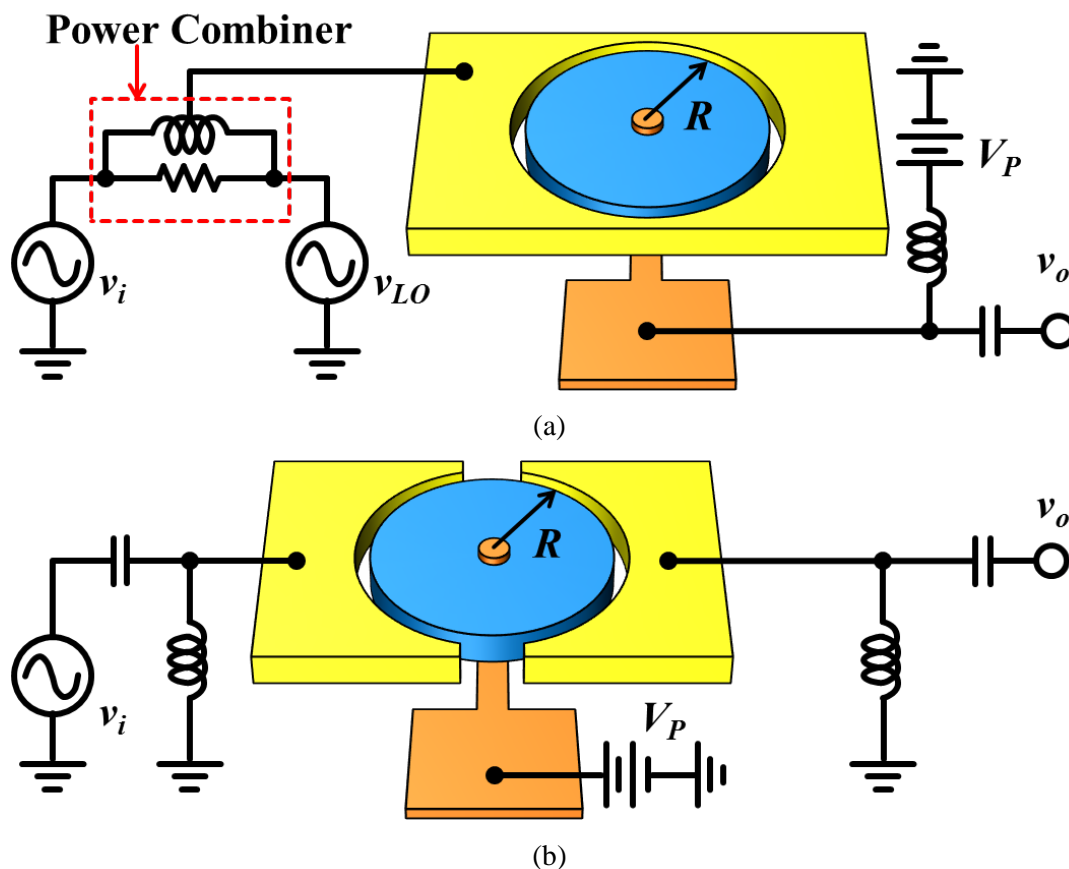
Figure 6-2: Mixing measurement set-up for (a) fully-surrounding electrode one port devices; and (b) split electrode two-port devices.

Again, the polysilicon radial contour mode devices used for this work were based on the design and fabrication process of [33]. Figure 6-1 presents SEM's of the one- and two-port devices tested here. As shown, each device comprises a polysilicon disk suspended at its very center by a self-aligned stem support and surrounded by at least one electrode that overlaps its sidewall with a gap spacing less than 100 nm. An ac excitation signal applied to an electrode can then drive the device into a resonance vibration mode shape where the disk expands and contracts radially about its circumference, in a "breathing-like" motion. The one-port resonators feature a fully-surrounding electrode, as depicted in the SEM of Figure 6-1(a), whereas the two-ports split the electrode to generate two electrode halves, as depicted in the SEM of Figure 6-1(c). Typically measured frequency characteristics are also shown in Figure 6-1 next to respective SEM pictures.

As detailed in [33], the radial contour-mode resonance frequency of this disk depends primarily on its radius, and is only peripherally dependent upon its thickness. There is also a strong dependence on stem placement, where a mere 1μm of stem offset from the

Table 6-1: Resonance Frequency Statistical Summary.

Resonance Frequency	36 μm Diameter Polysilicon Disk Resonators											
	Wafer I (6 dies)						Wafer II (6 dies)					
One Port	#1	#2	#3	#4	#5	#6	#7	#8	#9	#10	#11	#12
Average [MHz]	153	153	153	153	152	152	152	153	152	152	153	153
Std. Dev. [ppm]	407	254	428	530	438	674	690	515	666	345	268	586
3 Adj. Std. [ppm]	306	199	404	547	415	586	677	511	599	313	259	636
Overall Std. [ppm]	1133						642					
3 Adj.Std. [ppm]	450						534					
Two Ports	#1	#2	#3	#4	#5	#6	#7	#8	#9	#10	#11	#12
Average [MHz]	153	152	152	152	152	152	152	152	152	152	153	152
Std. Dev. [ppm]	365	660	378	751	991	1061	819	1702	607	365	660	378
3 Adj. Std. [ppm]	219	316	310	447	429	821	321	1214	264	631	826	670
Overall Std. [ppm]	1214						984					
3 Adj.Std. [ppm]	584						695					

<div align="center">(a)</div> <div align="center">(b)</div>
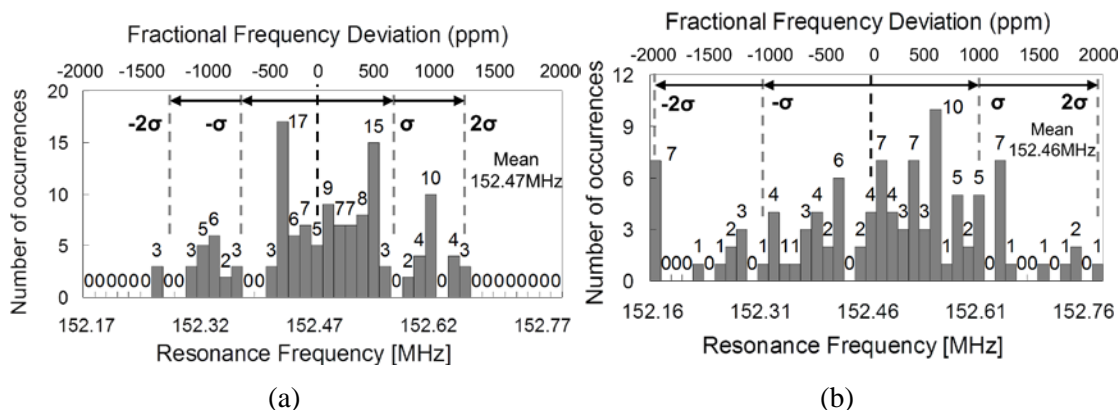
Figure 6-3: Resonance frequency distributions of one port (a) and two port (b) devices on wafer 2, clearly showing a wider spread of two port devices

disk center has been measured to cause a 3MHz change in resonance frequency [33]. Stem placement also greatly influences the Q of a stem-supported disk resonator. Thus, the present statistical analysis might also be interpreted as an evaluation of how well the process of [33] actually self-aligns the stem.

The data presented here were extracted across 12 dies from 2 wafers, 6 dies each, fabricated in two identical but independent runs using university facilities. The wafers from the two runs will be denoted wafer 1 and wafer 2 in the text that follows. Figure 6-1(b) illustrates the location of the test devices used for this work. As shown, the 6 dies chosen on each wafer are located near the center, and each die contains 21 self-aligned 36μm-diameter polysilicon disk resonators, in both one-port and two-port configurations.

Table 6-2: Quality Factor Statistical Summary.

Quality Factor	36 µm Diameter Polysilicon Disk Resonators With Single Surrounding Electrode											
	Wafer I (6 dies)						Wafer II (6 dies)					
Vacuum	#1	#2	#3	#4	#5	#6	#7	#8	#9	#10	#11	#12
Average [MHz]	6387	6262	6317	6471	6279	6406	6418	6478	6427	6364	6363	6417
Std. Dev. [ppm]	428	372	395	352	290	495	399	318	260	386	314	459
3 Adj. Std. [ppm]	495	317	320	302	228	414	292	313	234	368	306	396
Overall Std. [ppm]	393 (i.e. 6.14%)						357 (i.e. 5.58%)					
3 Adj.Std. [ppm]	361 (i.e. 5.64%)						320 (i.e. 5.00%)					
Air	#1	#2	#3	#4	#5	#6	#7	#8	#9	#10	#11	#12
Average [MHz]	4091	4018	4031	4149	4019	4122	4071	4052	4082	4123	4091	4018
Std. Dev. [ppm]	132	139	231	164	185	177	143	161	157	151	132	139
3 Adj. Std. [ppm]	135	150	220	121	158	155	121	175	165	171	153	138
Overall Std. [ppm]	179 (i.e. 4.48%)						156 (i.e. 3.90%)					
3 Adj.Std. [ppm]	161 (i.e. 4.03%)						151 (i.e. 3.78%)					
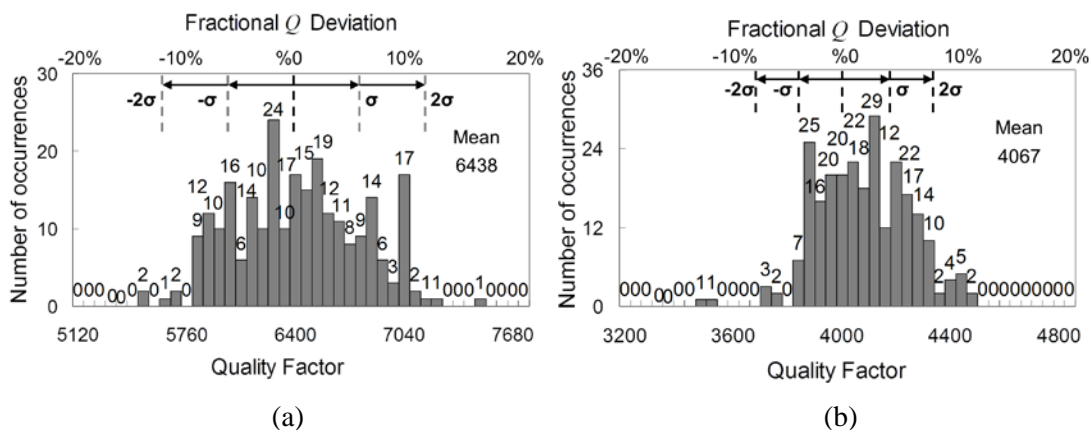
Figure 6-4: Quality factor distributions for the fully surrounding electrode one port device operating a) under vacuum; and b) in air, clearly showing a tighter Q distribution in air.

The fabricated disk resonators were tested under vacuum and air environments using the mixing measurement method described in [51] and depicted in Figure 6-2 for the cases of (a) one-port and (b) two-port devices. For both cases, a dc-bias V_P of 8V, local oscillator amplitude and frequencies of 3V and 15MHz, respectively, and an unmatched RF input power of -5dBm, were used. Table 6-1 and Table 6-2 summarize the measured averages and standard deviations (including pooled).

Figure 6-3(a) presents a histogram giving the resonance frequency distribution for fully-surrounding electrode one-port devices across all dies on wafer 2, showing a standard deviation of 642 ppm. The standard deviation across wafer 2 was considerably smaller than the 1133 ppm on wafer 1, indicating a variance in the processing conditions at the University of Michigan microfabrication facility from run to run. The resonance frequency averages of wafers 1 and 2 are seen to differ by 260 ppm. Although a larger data set is

needed to make any useful conclusions, the deviation seen so far from these two wafers is good enough to achieve 3%-bandwidth pre-select RF filters for communication front-ends without the need for trimming.

Since micromechanical filters [32] generally consist of coupled resonators in close proximity, the standard deviation obtained from the pooled variance amongst all sets of three adjacent resonators is perhaps more useful than the simple device-to-device standard deviation [73]. The three-adjacent pooled standard deviation over wafer 1 is 450 ppm; over wafer 2 is 534 ppm; and over both wafers is 462 ppm. Again, these are all is actually good enough to reliably attain 3%-bandwidth filters without trimming.

Figure 6-3(b) presents a histogram for the split electrode two-port devices of wafer 2. Here, a much wider spread in frequencies than for wafer 2's fully-surrounding electrode devices is seen, with a standard deviation of 984 ppm. It is possible that this larger standard deviation derives from the asymmetrical nature of a two-port drive and sense configuration versus the more balanced drive of a fully-surrounding electrode. In particular, the more balanced excitation afforded by the fully-surrounding electrode may help to reduce anchor-derived frequency shifts, leading to a tighter distribution. On the other hand, a two-port drive excites the disk on one side, and thus, pushes on the anchor from that direction, giving the anchor more influence on the frequency of the device. More study is required to verify this hypothesis, but if true, then anchor design now becomes crucial for frequency repeatability, as well as Q (for which it has always been important).

Figure 6-4 presents histograms of measured Q across all dies of all wafers for fully-surrounding electrode devices operated under (a) vacuum and (b) air. Here, a tighter distribution is clearly seen for air-operated devices, which (at the expense of lower Q) exhibit a 4.18% standard deviation versus the 5.86% seen under vacuum. It appears that viscous gas damping in air provides a more repeatable damping mechanism than the anchor loss mechanisms that dominate in vacuum.

6.2 Resonator Arraying for Better f_o Repeatability

Through previous study, the resonance frequency repeatability of micromechanical disk resonator fabricated using a university facility has been evaluated. Although the more balanced fully surrounding electrode configuration can reduce the standard deviation of f_o down to 642ppm, which satisfy the needs for ~3% bandwidth pre-select filters without trimming, this amount of frequency stability is still not sufficient for filters with even tinier bandwidth filters, e.g. RF channel select filters. In addition, the fully surrounding electrode configuration is not a prevalent remedy for all kinds of resonator designs, especially some of the very high quality factor devices, e.g. side supported wine-glass mode disk resonators. Fortunately, a better technique that can more effectively enhance the manufacturing precision has been developed. Detailed theoretical analysis and experimental study of this technique are explained in the following section.

In this section, a statistical comparison between the resonance frequency variations of stand-alone micromechanical disk resonators and mechanically-coupled array composites of them reveals that mechanically-coupled arraying of on-chip micromechanical resonators can very effectively enhance the manufacturing repeatability of resonance frequencies. In particular, twenty 3-disk resonator array-composites on a single die achieve a measured resonance frequency standard deviation as small as 165.7 ppm around a 61.25 MHz average, which is significantly smaller than the 316.4 ppm measured for twenty stand-alone disk resonators on the same die. This new standard deviation reduces the expected filter percent bandwidth achievable with a 90% confidence interval without the need for trimming from the 1.89% of previous work to now just 0.86%. Larger arrays should further reduce the frequency standard deviation, perhaps to the point of allowing trim-free RF channel-select bandwidths with reasonable manufacturing confidence interval.

Again, micromechanical filters constructed using high-Q on-chip micromechanical resonators have recently been demonstrated with insertion losses less than 2.5dB for filter percent bandwidths small enough to select individual communication receiver channels (as opposed to bands of channels), while rejecting all out-of-channel interferers. For example, the filter of [47] utilized micromechanical disk resonators with Q's of 10,000 to achieve a two-pole Chebyshev response with a percent bandwidth of 0.06%, for which only 2.43dB of insertion was observed. If implemented using the much higher frequency disks of [74], which also achieve Q's >10,000, such a filter structure might then allow channel-selection right at RF, immediately after the antenna in a wireless receiver. As described in [75], by removing all interferers and allowing only the desired signal to pass to subsequent electronics in the receive path, such an RF channelizer would greatly lower the dynamic range requirements of the electronics, and thereby substantially enhance the robustness and lower the power consumption of the receiver.

To realize this, a practical RF channelizer would likely need to employ one of the following schemes:

1) A single channel-selecting RF filter tunable over the desired frequency range, as depicted in Figure 6-5(a).

2) A bank of on-off switchable channel-selecting RF filters, placed side-by-side and covering the desired frequency range, as depicted in Figure 6-5(b).

3) A combination of 1) and 2) above, i.e., a bank of tunable and on-off switchable channel-selecting RF filters covering the desired frequency range, as depicted in Figure 6-5(c).

Note that although approach 2) requires the largest number of resonators, it also can realize the fastest spectrum analyzer of the three approaches—something needed for future cognitive radio targets [58] [76]. Also, note that each of the above schemes is possi-
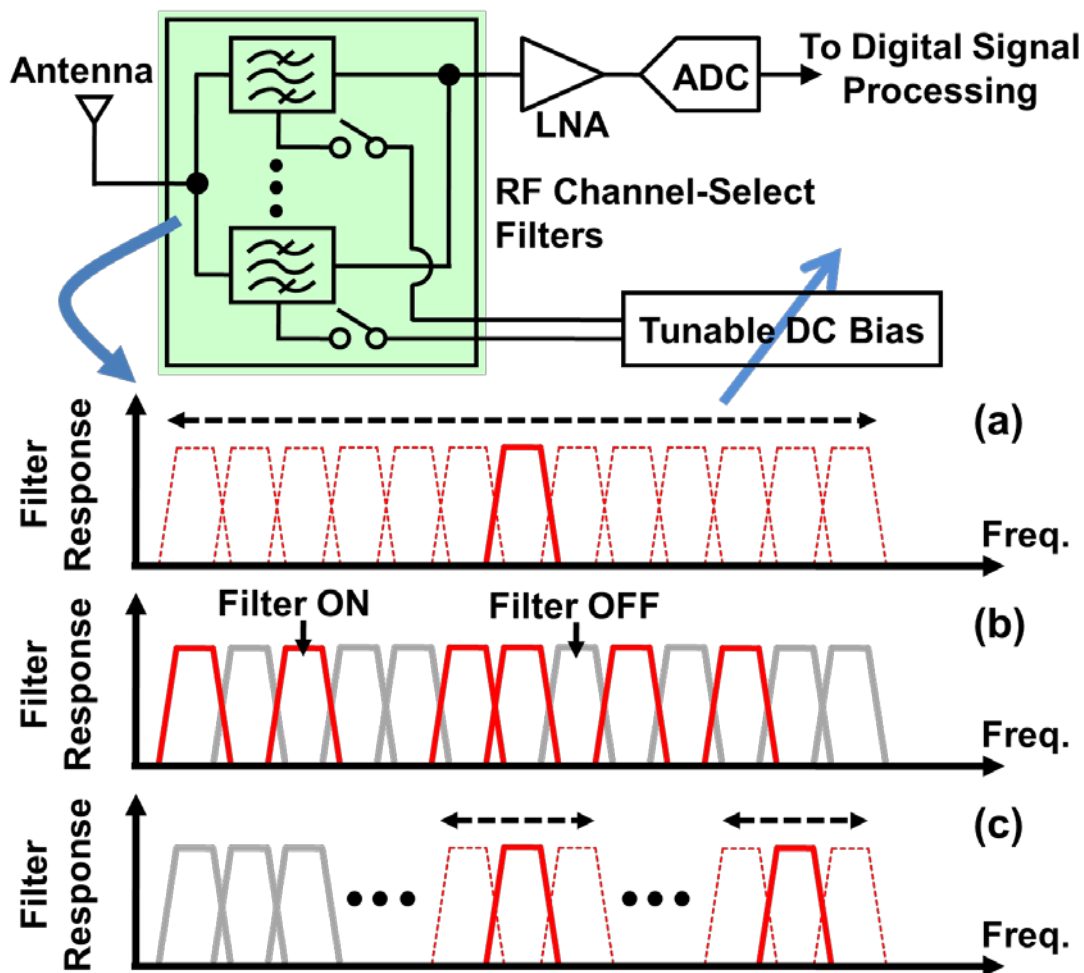
Figure 6-5: Schematic of a channelizing RF front-end with three implementation options: (a) A single tunable channel-selecting filter. (b) A large bank of non-tunable, but on-off switchable, filters. (c) A smaller bank of tunable and on-off switchable filters.

ble using filters comprised of capacitively transduced micromechanical resonators, where the dc-bias required for resonator operation can be utilized to both switch a given filter on and off [77] and tune its center frequency [2] [30].

Each of the above schemes also benefits greatly from its tunable or banked implementation, which very conveniently obviate the need for stringent absolute tolerances in center frequency. In particular, for the case of approaches 1) and 3), as long as the fabrication process can place a filter's center frequency within the band over which the filter must be tuned, the exact value of the untuned center frequency does not matter. For the case of the bank of filters in approach 2), it again does not matter where the filter initial center frequencies land immediately after fabrication, as long as the separations between
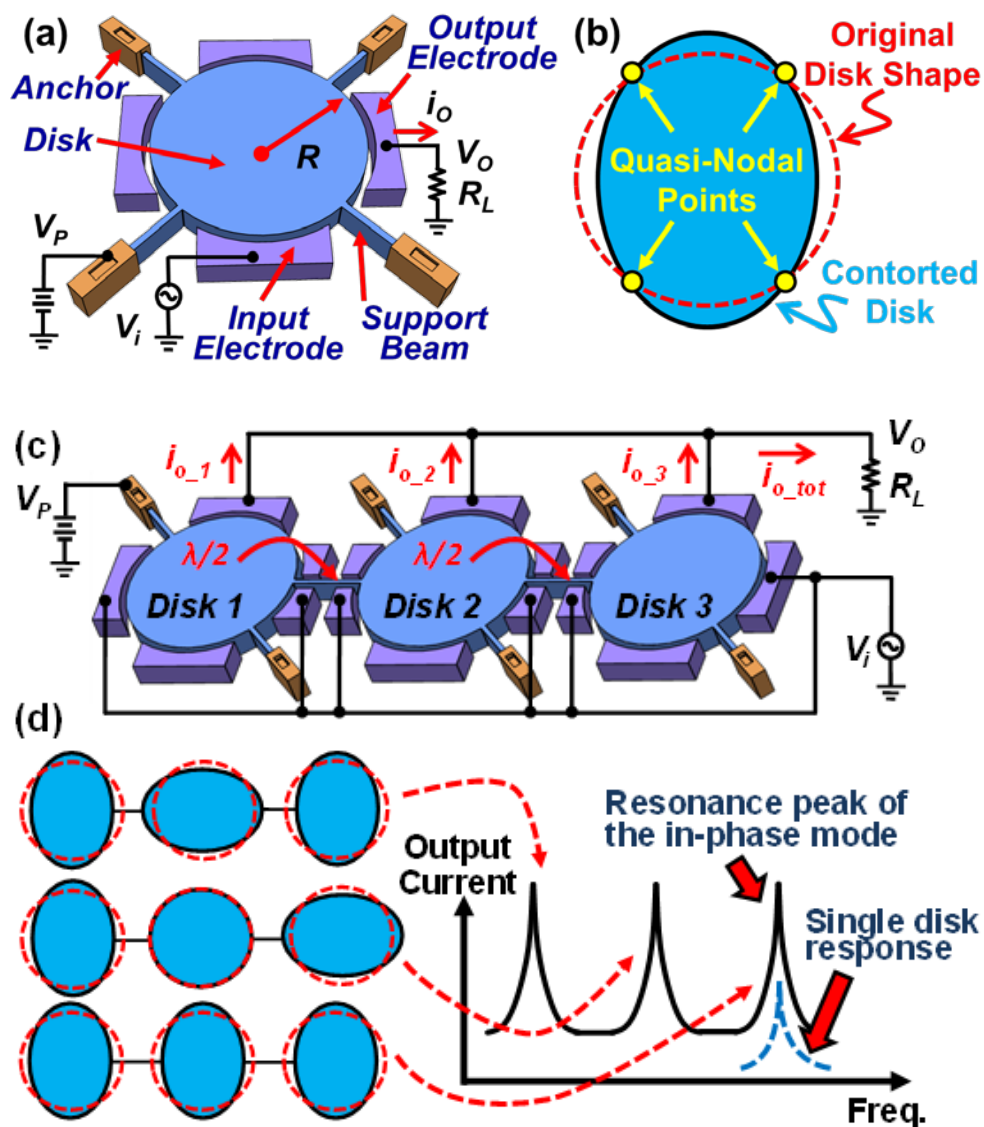
Figure 6-6: (a) Perspective-view schematic of a stand-alone micromechanical wine-glass mode disk resonator in a typical two-port bias and excitation configuration and (b) schematic of its compound (2,1) mode shape. (c) Perspective-view schematic of a 3-disk composite array resonator and (d) its three different mode shapes.

the center frequencies of adjacent filters is correct, and as long as a global frequency tuning capability exists where all filters can be tuned in one direction simultaneously. As already mentioned, the dc-bias provides such a global frequency tuning capability.

Still, although the above schemes obviate the need for minimum absolute tolerances, they do not necessarily eliminate the need for matching tolerances. In particular, the flat-

ness or accuracy of the passband of any filter relies heavily on the relative frequencies of its constituent resonators. Because of this, and because wafer-level fabrication processes often achieve much better matching tolerances than absolute tolerances, past micromechanical filters have been designed using identical resonators with quarter-wavelength couplers to spread their frequencies and generate a passband [78]. Here, the matching tolerance of the fabrication process used must be sufficiently good to avoid passband distortion caused by mismatches in the constituent resonators [73].

Unfortunately, although sufficient for 1.6% bandwidth filters [73], the matching tolerances achieved by a university microfabrication facility are still not good enough to achieve channel-selecting filters, with percent bandwidths below 0.14% at GHz frequencies. Tuning via dc-bias voltages can of course still be used to correct for mismatch-derived pass-band distortions, but this would entail more complicated control electronics and interconnect routing, so probably should be avoided, if possible. At any rate, a method for reducing the mismatch tolerances, i.e., frequency standard deviation, of a given micromechanical resonator is highly desirable.

Pursuant to attaining improved frequency standard deviations, this work employs mechanically-coupled array composite resonators [48] to effect a frequency averaging that reduces the overall standard deviation of frequency by approximately the square root of the number of resonators in the array. Specifically, a statistical comparison between the resonance frequency variations of stand-alone micromechanical disk resonators and mechanically-coupled array composites of them reveals that mechanical-coupled arraying of on-chip micromechanical resonators can very effectively enhance the manufacturing repeatability of resonance frequencies. In particular, twenty 3-disk resonator array-composites on a single die achieve a measured resonance frequency standard deviation as small as 165.7 ppm around 61.25 MHz, which is significantly smaller than the 316.4 ppm measured for twenty stand-alone disk resonators on the same die.

Figure 6-6(a) presents the basic micromechanical resonator used in this work as a vehicle to evaluate the efficacy of arraying for better repeatability. This device, dubbed the "wine-glass disk" resonator, consists of a polysilicon disk supported by four beams attached at quasi-nodal locations, and surrounded by two pairs of electrodes along two orthogonal axes. When driven by the combination of a dc-bias voltage applied to its structure and an ac voltage at its resonance frequency applied to one of the electrode pairs, the disk vibrates in the compound (2,1) mode shape, where it extends along one axis while contracting along the orthogonal axis, as depicted in Figure 6-6(b). This figure also shows how the support beam attachment locations correspond to extensional nodal locations (but not tangential, hence the term "quasi-nodal"). In practice, these locations are not perfect extensional nodes, either. They, however, negate motion well enough that choosing them as support attachment locations minimizes energy loss through the supports to the substrate, thereby maximizing the Q of the compound (2,1) mode. As shown in Figure 6-10, measured Q's regularly exceed 120,000.
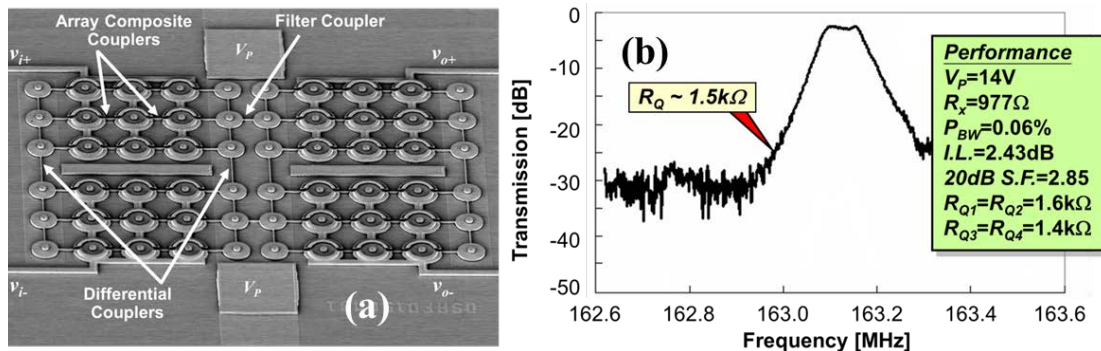
Figure 6-7: (a) SEM photo of a 163-MHz differential disk-array composite microme-chanical filter and (b) frequency transmission spectrum.

With Q's this high, the stand-alone device of Figure 6-6 is obviously quite useful as the frequency setting element for a self-sustaining oscillator, and indeed oscillators that satisfy the reference oscillator phase noise specifications for GSM cellular phones have already been successfully achieved using stand-alone wine-glass disk resonators [28]. Still, improved device properties and much greater functionality ensue when a number of the above disk resonators are mechanically coupled into a composite array resonator, such as shown in Figure 6-6(c). In past work, mechanically coupled arrays have been used to alleviate certain perceived micromechanical resonator deficiencies, specifically high impedance and low power handling ability relative to much larger conventional high-Q devices, such as quartz crystals. In the mechanically coupled array composite of Figure 6-6(c), half-wavelength mechanical coupling between the resonators forces them to vibrate at the same mode frequency, which then allows their responses to directly add, into a much larger output current—larger by a factor equal to the number of resonators used in the array. This larger output current, of course, results in higher power handling and lower motional resistance, each by a factor equal to the number of resonators used. To insure a single resonance peak, the array composite resonator of Figure 6-6(c) uses half-wavelength coupling and strategic phasing of electrode excitations to accentuate a desired mode while suppressing unwanted ones.

Among examples where such array composite resonators have been used successfully are the GSM-phase-noise compliant oscillator demonstrated in [28] that achieved phase noise marks of -140dBc/Hz at 1kHz offset from a 13-MHz carrier and -150dBc/Hz at far-from-carrier offsets; and the disk array composite filter of [47] that achieved an insertion loss of only 2.43dB for a 0.06% bandwidth centered around 163MHz. The last of these, depicted in Figure 6-7 with a measured transmission spectrum, is particularly compelling, as it actually employs four identical arrays in a hierarchical mechanical circuit structure. As described in [47], the four arrays not only enable termination impedances of 1.5kΩ that are optimal for a fully integrated receiver front-end, but also make possible a differential input/output configuration that suppresses electrical feedthrough and eliminates spurious mechanical responses. The resulting filter occupies only 560μm×360μm and, if

translated to higher RF frequencies, would be much smaller while also suitable for implementation of the channelizers in Figure 6-5.

Unfortunately, however, the filter response in Figure 6-7(b) was achievable only via tuning of its resonator frequencies via the dc-bias-dependent electrical stiffness mentioned previously. Indeed, immediately after fabrication, mismatches between resonators in each array generate an offset in the relative positions of the two filter peaks, leading to a large dip in the ensuing filter passband, i.e., distorting the filter pass-band.

Interestingly, if the filter of Figure 6-7 had only used more resonators in its four array composites, it might have required much less tuning, if any at all. To see this, we first establish that for certain modes of a mechanically-coupled array, the frequency of the array at which all of its constituent resonators vibrate essentially ends up being the average of the resonance frequencies of each of the constituent resonators.

6.2.1 Resonance Frequency Averaging

The resonance frequency of the in-phase-mode of the 3-disk array composite depicted in Figure 6-6 can be expressed by [48]

$$f_{array} = \frac{1}{2\pi} \sqrt{\frac{\sum_{i=1}^{3} k_i}{\sum_{i=1}^{3} m_i}} = \frac{1}{2\pi} \sqrt{\frac{k_1 + k_2 + k_3}{m_1 + m_2 + m_3}} \tag{6.1}$$

where k_i and m_i are the effective spring constant and mass, respectively, of the ith resonator. For the case where the resonators in the array are identically dimensioned wine-glass mode disks, (6.1) predicts that the in-phase mode frequency of the array will be the same as that of a single one of its constituent resonators.

If on the other hand each resonator experiences small deviations in frequency Δf_i, perhaps arising from small deviations in radius ΔR_i that in turn generate deviations in mass Δm_i, then (6.1) can be expanded as:

$$f_{array} = \frac{1}{2\pi} \sqrt{\frac{3k_o}{(m_o + \Delta m_1) + (m_o + \Delta m_2) + (m_o + \Delta m_3)}}$$

$$\tag{6.2}$$

$$f_{array} = \frac{1}{2\pi} \sqrt{\frac{3k_o}{3m_o} \left(1 + \frac{1}{3}\frac{\Delta m_1}{m_o} + \frac{1}{3}\frac{\Delta m_2}{m_o} + \frac{1}{3}\frac{\Delta m_3}{m_o}\right)^{-1/2}}$$

where k_o and m_o are the designed effective spring constant and mass, respectively, and where it has been recognized that the stiffness k_o of a wine-glass disk resonator is to first order not a function of radius. If the deviations between resonators are small, (6.2) can be Taylor expanded to first order to yield:

$$f_{array} = f_s \cdot \left[1 + \left(-\frac{1}{2} \right) \left(1 + \frac{1}{3} \frac{\Delta m_1}{m_o} + \frac{1}{3} \frac{\Delta m_2}{m_o} + \frac{1}{3} \frac{\Delta m_3}{m_o} \right) \right] \tag{6.3}$$

which then reduces to:

$$f_{array} = \frac{1}{3}(f_s - \Delta f_1) + \frac{1}{3}(f_s - \Delta f_2) + \frac{1}{3}(f_s - \Delta f_3)$$

$$\tag{6.4}$$

$$f_{array} = \frac{1}{3}(f_1 + f_2 + f_3)$$

where f_s is the designed resonance frequency of single disk. Thus, for the case where all resonators are nearly identical, i.e., the deviations are small, the resonance frequency of an array composite of them is approximately equal to the average of the frequencies of its constituent resonators.

6.2.2 Reduction in Standard Deviation

The frequency averaging governed by (6.4) is beneficial, since it reduces the resonance frequency standard deviation of the array composite resonator caused by random process variations. In particular, the standard deviation of the resonance frequency of a disk-array composite resonator is given by

$$\sigma_{f_{array}} = \frac{1}{N} \sqrt{\sum_{i=1}^{N} VAR(f_i) + \sum_{i,j=1, i \neq j}^{N} 2COV(f_i, f_j)} \tag{6.5}$$

where N is the number of resonators coupled in the array. In general, process variations across a wafer might not be completely random, so the covariance term in (6.5) would take on a finite value. However, for the present case of an array of resonators occupying a very small area on a die, the variations might indeed take on a more random nature, which would then null out the covariance terms, yielding a very simple expression for the composite array frequency standard deviation:
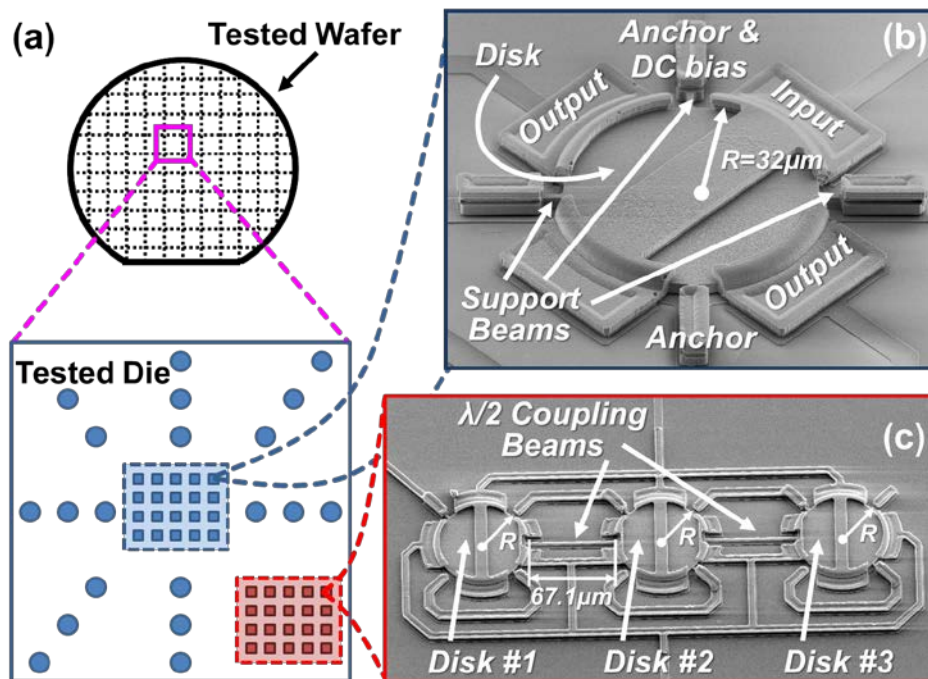
Figure 6-8: (a) Relative locations on each tested die and SEM photos of the measured 61-MHz (b) stand-alone wine-glass mode resonators; and (c) 3-disk mechanically-coupled array composites. The disks of (b) and (c) all have radius $R = 32$ μm, thickness $h = 3$ μm, and electrode-to-resonator gap spacing $d_o = 100$ μm. In addition, the wavelength $\lambda = 134.2$ μm.

$$\sigma_{f_{array}} = \frac{\sqrt{N}}{N}\sigma_{f_i} = \frac{1}{\sqrt{N}}\sigma_{f_i}(i = 1,2,\cdots,N) \tag{6.6}$$

6.2.3 Measurement Results

To verify the above formulations, 61-MHz micromechanical wine-glass disks and three-resonator array composites of them were fabricated via the small lateral-gap polysilicon surface micromachining process described in [33].This work compiles measured data from five dies fabricated in two different runs. Each die contains twenty single disks and twenty 3-disk arrays at the relative locations indicated in Figure 6-8, which also presents SEM photos of each device type.

Devices were tested via an Agilent E5071B Network Analyzer while under 1.5μTorr vacuum provided by the SUSS PMC150 temperature-controllable vacuum probe station
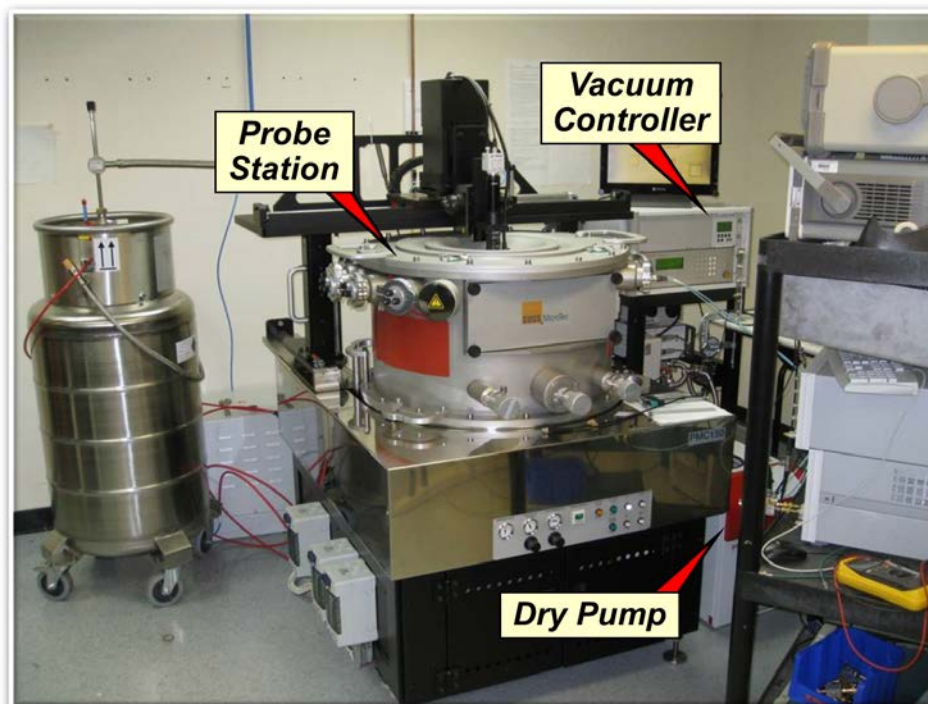
Figure 6-9: Photo of the SUSS MicroTech PMC150 temperature-controllable vacuum probe station used to collect statistical resonance frequency data.

pictured in Figure 6-9. The lift and pan capability of probes on the SUSS tool greatly facilitated testing of the many devices required to attain adequate statistical convergence.

Single Device Measurements

Figure 6-10 compares the measured frequency response characteristics of a stand-alone 61-MHz wine-glass disk and a 3-disk array composite of them. As expected, the 3-disk array composite provides a higher peak, which corresponds to a smaller motional resistance. In addition, the Q of the array composite is still quite high, in excess of 120,000, and not much smaller than the 141,000 of a stand-alone wine-glass disk.

Measured Statistics

Figure 6-11(a) presents a plot of measured frequency versus device index for the 200 disks and array composites from the 5 tested dies. Clearly, the arrays of each die exhibit smaller frequency variations compared to the stand-alone disk devices on the same die. Figure 6-11(b) zooms in on the data for die #2, for which the resonance frequency standard deviation of the twenty 3-disk arrays is only 165.7 ppm, which is around 1.92× smaller than the 316.4 ppm exhibited by the twenty stand-alone disk resonators located on the same die. Although a larger number of data points would instill more confidence
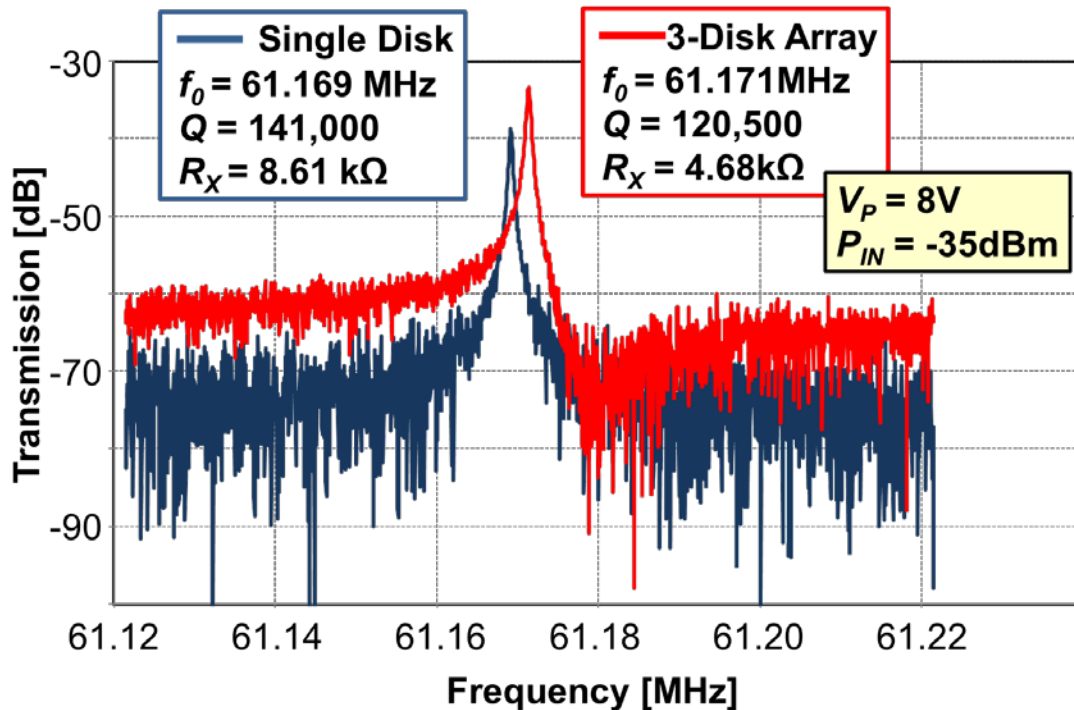
Figure 6-10: Measured plots comparing the frequency characteristics of a stand-alone 61-MHz wine-glass mode micromechanical disk resonator (in blue) and a 3-disk array composite of them (in red).

in this result, the measured ratio of resonance frequency standard deviation between stand-alone disks and 3-disk arrays is very consistent with the theoretical prediction of (6.6). This seems to support the assumption made in (6.6)'s derivation that the variations causing frequency shifts in the resonators making up the arrays were largely random, i.e., were uncorrelated.

Statistical Benefits of Arraying

Pursuant to gauging the benefits offered by the improved frequency repeatability afforded via arraying, a three-resonator 0.5% bandwidth micromechanical disk filter centered at 150-MHz with a designed ripple of 0.5dB (such as depicted in Figure 6-12) was first designed using the methods of [78] assuming perfectly matched constituent resonators, yielding the red simulated curve in Figure 6-12. Then, using data from Figure 6-11(b), radius variations of $\sigma_{single} = 316$ ppm and $\sigma_{array} = 165$ ppm were introduced according to the ΔR deviations depicted in Figure 6-12, which represent the worst case radial spread among resonators, i.e., the spread of ΔR's yielding the most passband distortion. The results of simulations using these spreads are plotted alongside the ideal simulation in Figure 6-12. The filter with 316 ppm radial variation exhibits passband distortion degradation as large as 0.7dB, which is large enough to impact a system application using
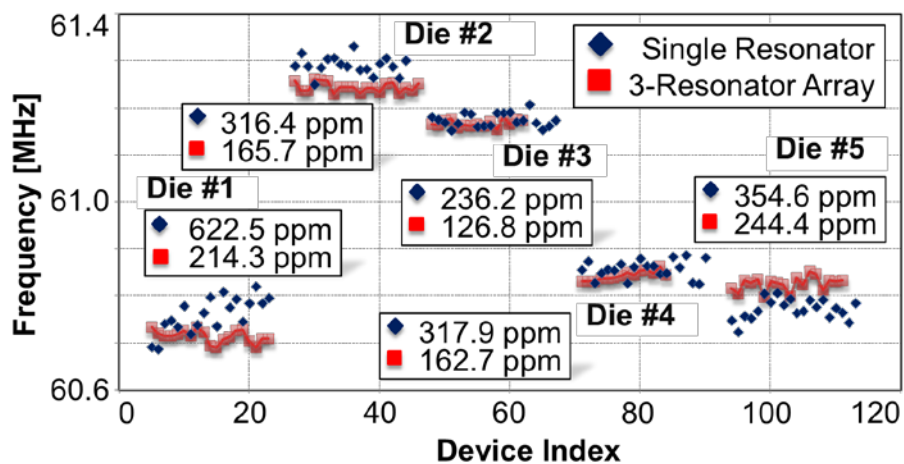
(a)
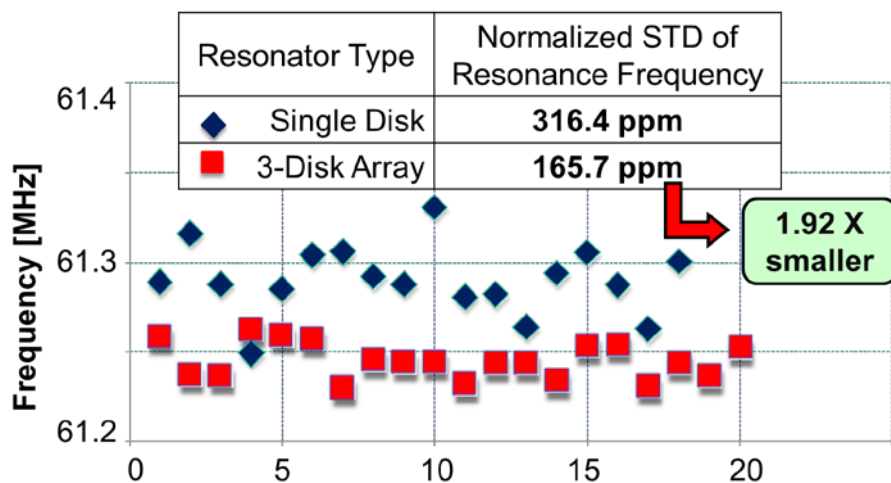
(b)

Figure 6-11: Measured plots comparing the frequency characteristics of a stand-alone 61-MHz wine-glass mode micromechanical disk resonator (in blue) and a 3-disk array composite of them (in red).

this filter. The same filter with 165 ppm radial variation shows a much smaller passband distortion degradation, on the order of only 0.29dB, which is often acceptable. Since 165 ppm corresponds to one standard deviation for a 3-disk array composite resonator, a 0.5% bandwidth filter of the type in Figure 6-12 but using 3-disk array composites as resonators could be made using our university fabrication process with a 68.2% confidence interval that passband distortions will be less than 0.3dB.

As the number of the resonators coupled in the array in-creases, (5.6) dictates that the frequency variation can be further reduced, allowing even smaller percent bandwidth fil-
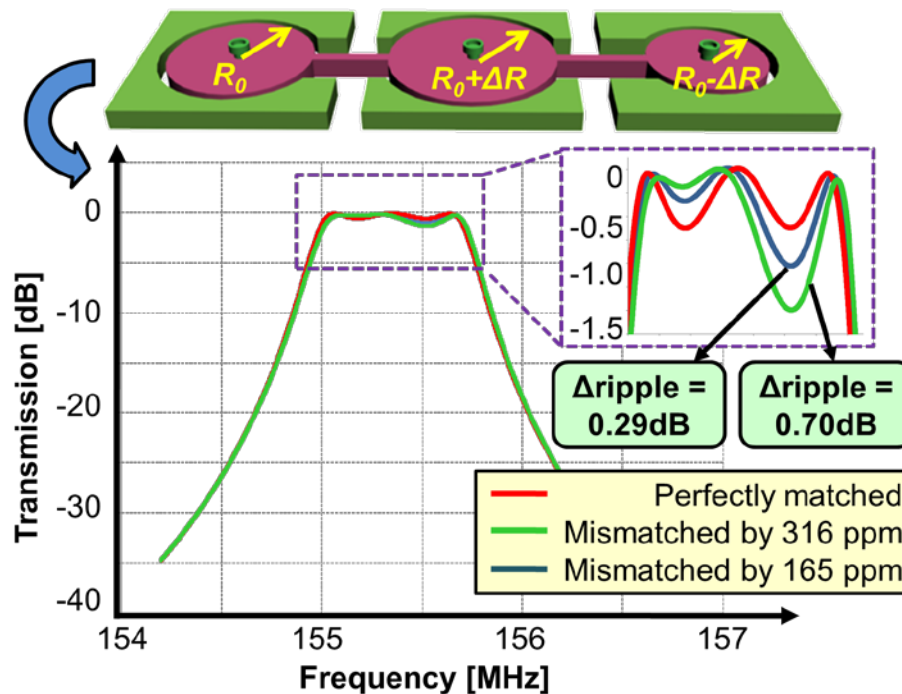
Figure 6-12: Simulated transmission curves for a properly designed and terminated 0.5% bandwidth three-pole micromechanical disk filter with no mismatch between resonators (red); $\Delta R/R = 165$ ppm, for which a passband distortion degradation of 0.29dB is seen; and $\Delta R/R = 316$ ppm, for which a passband distortion degradation of 0.7dB is seen.

ters without the need for trimming. Figure 6-13 illustrates this by plotting the standard deviations achievable by array composites of resonators for single-resonator starting standard deviations of 316 ppm (i.e., the value measured in this work) and 120 ppm, which might be achievable in a more professional foundry than the university one used for this work. The vertical axis on the left indicates the standard deviation for an array composite using the number of resonators indicated in the x-axis, while the right vertical axis indicates the corresponding percent bandwidth 3-resonator filter achievable without trimming with a 90% confidence interval. As shown, a prohibitively large number of resonators would be required to bring the standard deviation down to the 20 ppm level required for CDMA channel-selection at 900 MHz using a university fabrication process. However, if a more capable foundry with a 120 ppm single-resonator standard deviation were used, then a composite array of only 27 disks would be required to achieve the 0.14% bandwidth needed for CDMA channel-selection with 90% confidence interval without the need for trimming.

Of course, the above analysis pertains mainly to the case where only variations in the resonators are predominant. In general, variations in the beams coupling the resonators in
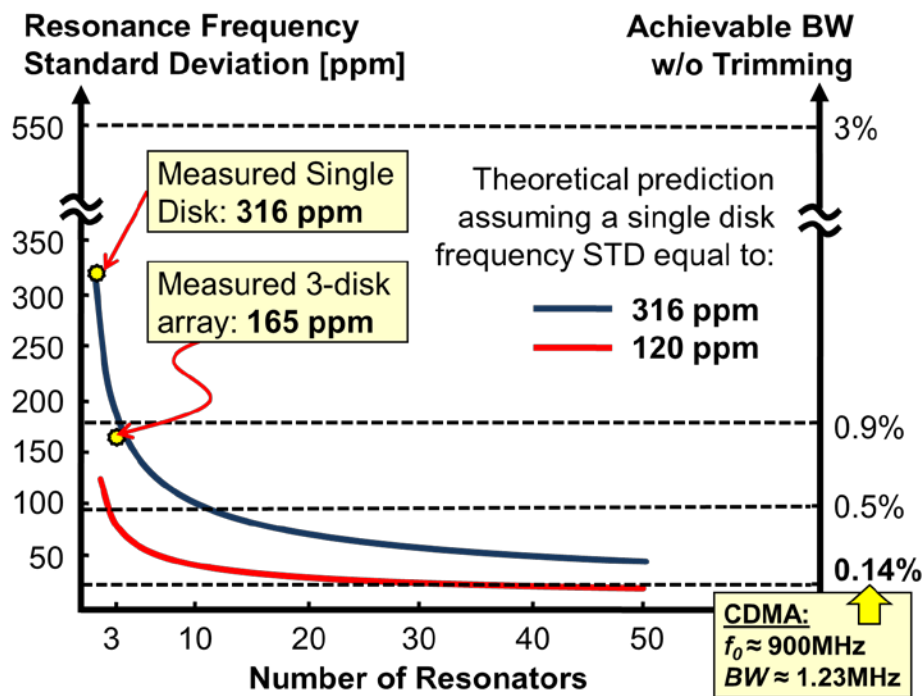
Figure 6-13: Theoretically predicted plots of resonance frequency standard deviation for array-composite resonators and the corresponding 90% confidence interval 3-pole filter bandwidth achievable via such resonators without trimming, both versus the number of resonators coupled in the array.

a filter will also contribute to passband ripple, but the effect of such variations will be less pronounced when the coupling beams are designed with quarter-wavelength dimensions, as described in [78]. The degree to which coupling beam mismatch affects passband distortion is presently under study.

The demonstration of standard deviation reductions from the 316 ppm of stand-alone resonators to the 165 ppm of 3-resonator array composites represents a reduction in the expected manufacturable 90% confidence interval trim-free filter percent bandwidth from 1.89% to now just 0.86%. While 0.86% still is not small enough for direct RF channel-selection, it does bring us significantly closer to this, and an RF front-end with 0.86% bandwidth selectivity would still greatly reduce the dynamic range requirements of subsequent receiver electronics over the current 3% bandwidth pre-select filters presently in use. The demonstrated reduction of frequency standard deviation via mechanically coupled arraying suggests that if trimming is to be avoided, filters using array composite resonators, such as that of [47] or [79], might be preferred over filter realizations that utilize only stand-alone resonators in their construction. Indeed, it seems that arraying might outright be needed to actually achieve RF channel-select bandwidths of less than 0.14% without trimming.

6.3 Conclusions

This chapter summarizes and compares the frequency and Q standard deviation data taken from several resonator designs. The frequencies of wine-glass mode disk resonators with side supports shows tighter distribution than stem supported radial-contour mode ones. On top of that, the mechanically coupled arraying technique was found to be able to effectively reduce the frequency variation even more. These studies have pointed out a way to reduce minimum achievable bandwidth of the channel-select filters without trimming. More importantly for the main target of this dissertation, the suggested mechanically arraying is probably also the right approach when using multiple disk resoswitches to construct higher speed MEMS power converters because the frequencies of the constituent resoswitches are required to be as close to each as possible in order to avoid the slower gated sinusoidal driving.

CHAPTER 7 *Conclusions*

MEMS switches have the potential of replacing solid state switches in many applications, including some high volume ones e.g. power converters and power amplifiers, where high switch *FOM*'s are desired for better performance. However, so far they have done reasonably well only in microwave applications like antenna switching. There are certain key aspects for them to improve such as reduction of actuation voltages and increase of switching speed and life time cycles. If MEMS switches want to break the hurdle to enter the new broader fields, these improvements are very much mandatory. Having this as the ultimate target, this dissertation proposed this new resonant switch and has achieved the following:

1) Developed the polysilicon wine-glass mode disk resoswitch as a demonstration vehicle that proves the advantages of high-Q resonance operation;

2) Constructed an electroplated nickel disk resoswitch that has much lower series and contact resistances suitable for on-chip power amplification and demonstrated 17.7dB of power gain from a simple amplifier topology;

3) Designed and implemented a micromechanical displacement amplifier using mechanical circuit methodology that ensues larger displacement at output compared to that of input and thus avoids the unwanted mechanical impacts at input port effectively extending the hot-switched life time cycles of the disk resoswitch to over 173 trillion;

4) Demonstrated the first MEMS charge pumps with various topologies, including the Dickson's design and charge transfer series (CTS) voltage doubler design, based on comb-driven resoswitches;

5) Discovered characteristics of resoswitches through comparing switches made of different structural and contact materials. Identified and solved extra practical issues when orchestrating multiple resoswitches within a system such as squegging and resonance frequency variations;

6) Collected and analyzed the real process induced frequency variation data from adequate amount of devices fabricated using university facility and proposed a practical way that is verified in both theory and experiments to reduce the variation;

Although further characterizations of the resoswitches are undoubtedly need, the investigations done in this dissertation have gained sufficient confidence for carrying out the research in this field towards more ground breaking achievements.

7.1 Future Research Directions

The results presented in this dissertation provide a cultivation ground for future research. During the development of resoswitches and resoswitch based charge pumps, many new phenomena ranging from dynamics and material science were discovered and some of them were grasped more than the others. Each chapter has explained its own unsolved problems, but it is helpful from a systematic stand of point to reorganize them and summarize here the issues that need to be addressed in the near future:

1) Although the cycle life time of resoswitches are demonstrated to be substantially better than traditional RF MEMS switches, more complete data taken from devices that are being inserted in a oscillator loop (as shown in Figure 4-21) to maintain sustaining resonance are necessary in order to fully capture the life time limit of the resoswitches. Due to much larger contact forces, more extensive choices of materials are available and they can be easily evaluated and compared once the correct oscillatory test bench is built. It is very likely that optimization of contact resistances and life time cycles simultaneously will yield totally different material selections from what's being commonly suggested in current RF MEMS switches.

2) The amount of charge transferred is a function of the total time of impact, however, the contact time of the current rigid dynamic impacts is only a small fraction (1/30-1/20) of the switching period. It would require less cycles for given amount of charge to be transferred if the contact time can be increased. The ability to control contact time will take some more in-depth theoretical studies and one possible way to tune the contact time is to use flexural electrode supports instead of rigidly anchored ones.

3) During the testing of resoswitches, it is found that multiple contacts within one cycle can be excited when changing the frequency of the driving signal around the resonance frequency of the device (as shown in Figure 7-1). As also indicated on Figure 7-1, shapes and relative positions of the switching spike compared to V_{drive} are also changing as f_{drive} slightly increases. Provided more detailed investigation, this could be an alternative way to increase contact time of each cycle and to achieve more efficient charge transfer.

With more concrete understandings of the device characteristics, the charge pumps and the power amplifiers based upon resoswitches designed in this dissertation can then
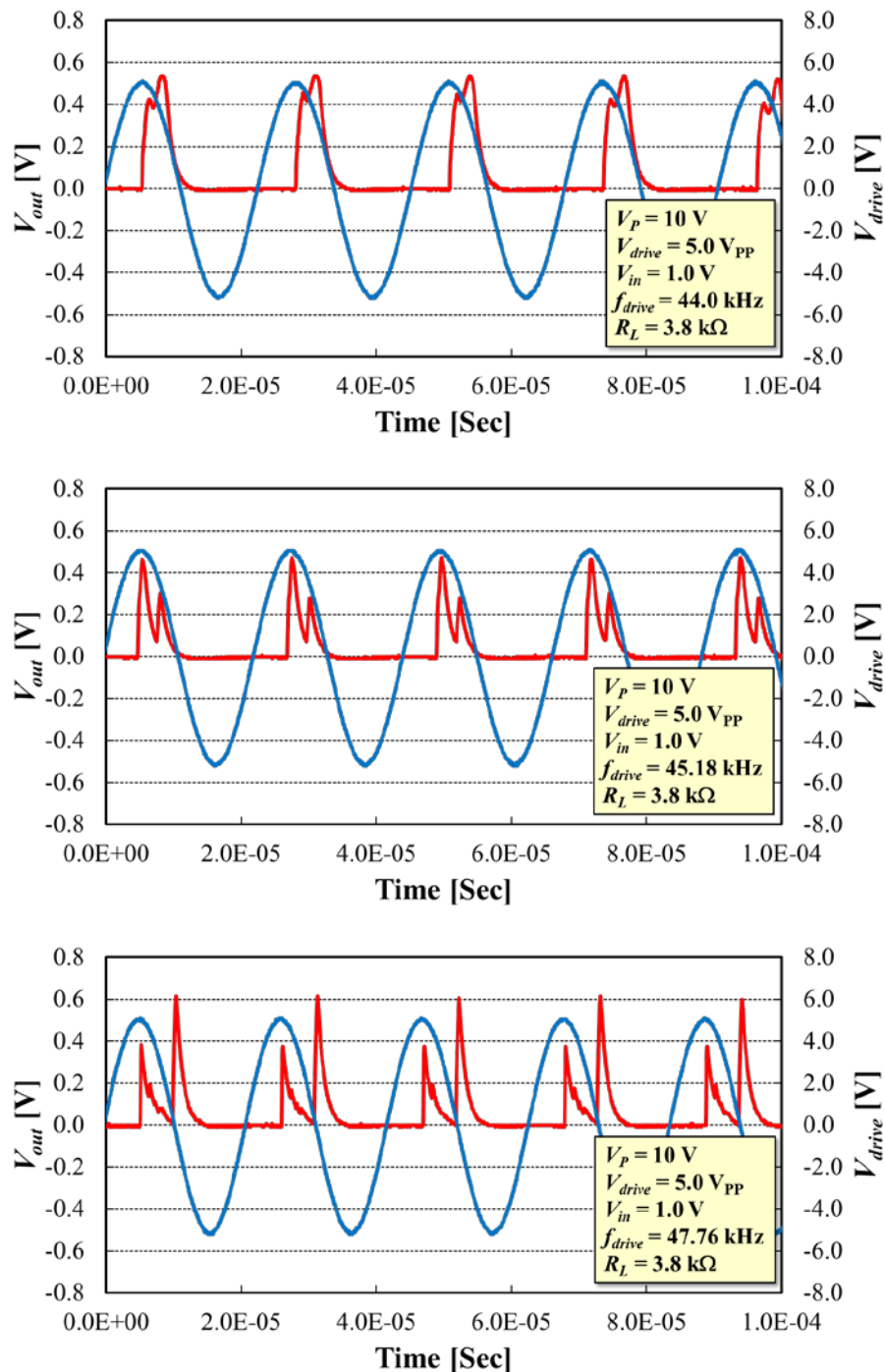
Figure 7-1: Output waveforms of a 44kHz comb-driven resoswitch obtained in air using the schematic of Figure 5-6 with increasing frequencies (f_{drive}) of the driving signal (V_{drive}) summarized in each inset table.
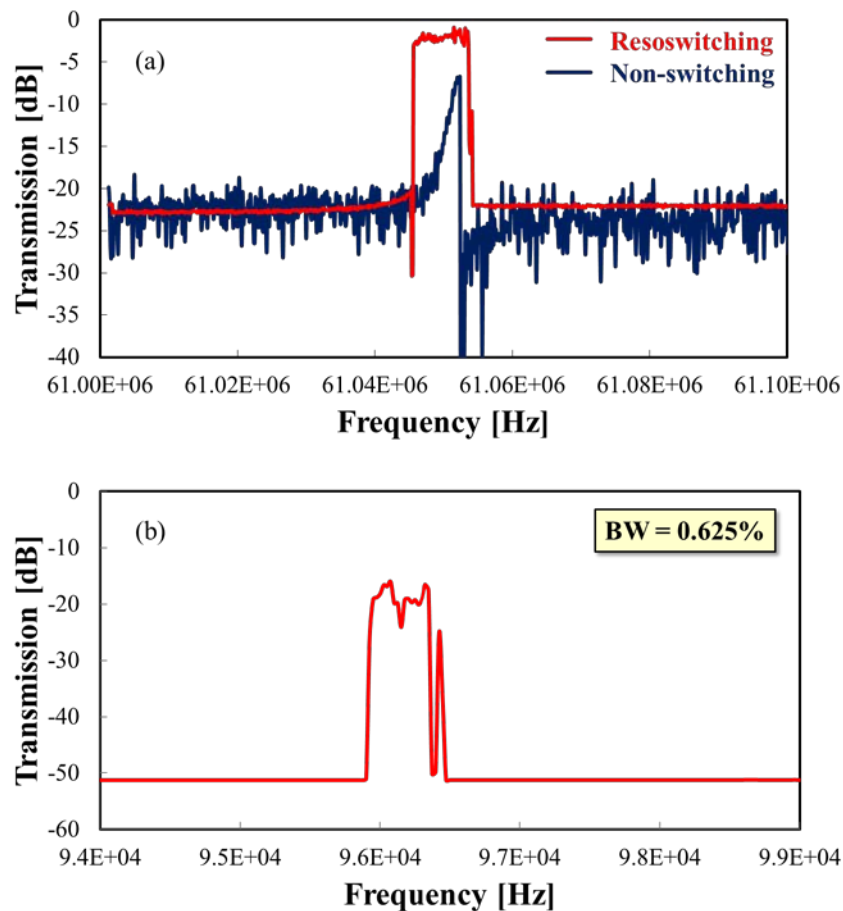
Figure 7-2: Measured spectra of (a) a 61MHz wine-glass mode disk resoswitch and (b) a 96kHz comb-driven resoswitch, both showing flat top filter type responses.

be optimized to become truly outperform the CMOS ones in terms of efficiencies and power delivery capability which are currently not advantageous on the MEMS side. By then, charge pumps with more stages (>5) will be demonstrated that can generate ultra-high output voltages (100-200V). Some other converter topologies which are considered to be cost or area inefficient in the CMOS world, such as buck converters, can also be implemented using resoswitches and MEMS inductors that can easily be fabricated at the same time at no extra cost. Real MEMS class-E power amplifiers will be demonstrated as well that can achieve sufficient power gain and life time with lower cost and higher efficiencies than solid state technologies.

Meanwhile, better designed resoswitches that achieve even lower needed actuation voltages and contact resistances can soon enable the capability of constructing some other types of components, such as:
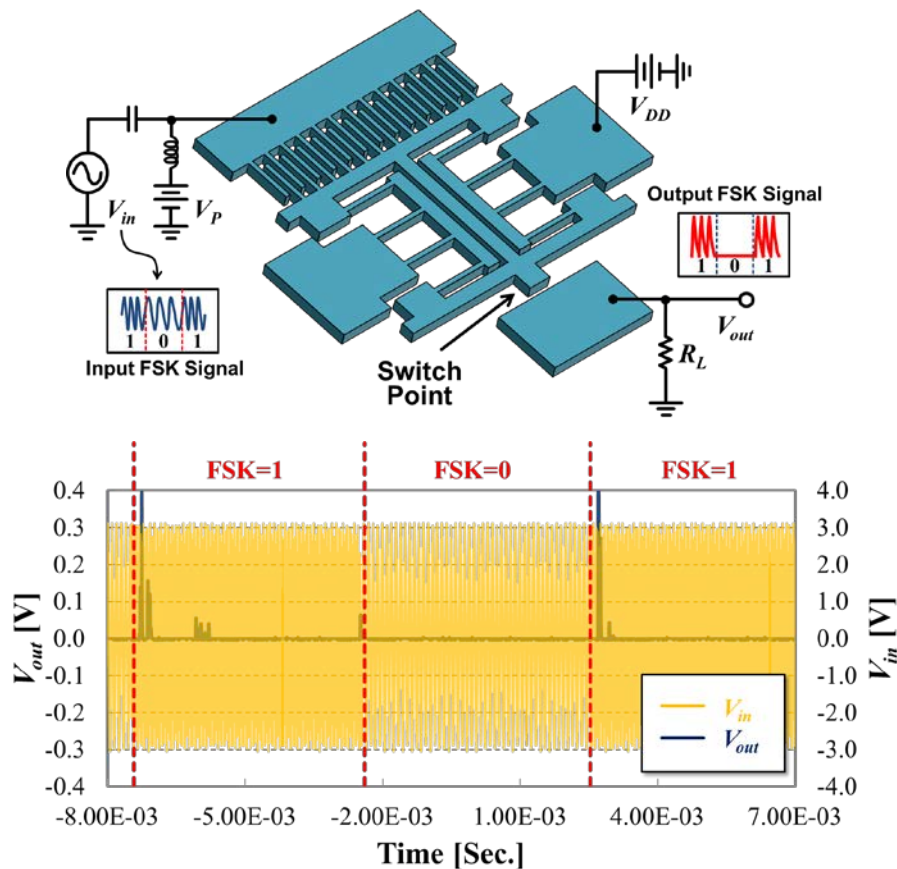
Figure 7-3: Schematic of FSK input signals driving a 44kHz comb-driven resoswitch and the measured input and output waveforms.

1) Resoswitch based filter

Problems with conventional electrostatic MEMS filters can possibly be solved by resoswitches. First of all, being an electrostatic vibrating device, the resoswitch retains the nice frequency selective properties due to the same high-Q resonance operation. On the other hand, hot-switched impacting at the output port boosts output signal amplitude to overcome the deficit at the input capacitively transduction or even get gain [38] [80]. Advantages of resoswitches in improving filter performances have been initially discovered during the experimental characterization of resoswitches. Figure 7-2 are the measured frequency spectra of a disk resoswitch and comb-driven resoswitch, both showing a transmission curve shape with ultra-sharp roll off and tiny insertion loss, an ideal filter response that MEMS technology has always been pursuing. Furthermore, the bandwidth of the resoswitched-filter can be simply tuned by changing mechanical design parameters, such as switch gap size. The ripples of the passbands shown in Figure 7-2 are not acceptable. However, given the more careful contact engineering mentioned above, much smoother passbands can eventually be expected.

2) Low power frequency-shift keying (FSK) receiver

Combining the frequency selective and power amplifying functions, the resoswitches can ideally be turned into a low power filter-LNA that would greatly benefit the front-end RF receiver design [80]. The idea of frequency-shift keying channel select receiver proposed in [80] has been preliminarily verified via a 44kHz comb-driven resoswitch. The testing circuit schematic and the measured waveforms are shown in Figure 7-3, where output spikes are only triggered when FSK=1. Despite the fact that the operating frequency is not within the range that RF receivers generally are interested in and the sensitivity is not high enough yet to tolerate the dynamic range of the received signals, the feasibility of going down this path is crystal clear.

7.2 Concluding Remarks

In summary, this dissertation has studied and presented the first micromechanical switch operating at high-Q resonance that solves a number of issues of conventional MEMS switches. Through the demonstrations of the first resoswitch based power amplifier and charge pump, the promising potential of positioning MEMS devices in power conversion and amplification (or even more) applications has been exhibited and the foundation for further research and development in the future has been established.

Bibliography

[1] L. E. Larson, R. H. Hackett and R. F. Lohr, "Micromachined microwave actuator (MIMAC) technology-a new tuning approach for microwave integrated circuits," in *Digest of Papers, Microwave and Millimeter-Wave Monolithic Circuits Symposium*, Boston, MA, Jun. 1991, pp. 27-30.

[2] H. C. Nathanson, W. E. Newell, R. A. Wickstrom and J. R. Davis, Jr., "The resonant gate transistor," *IEEE Transactions on Electron Devices,* vol. 14, no. 3, pp. 117-133, 1967.

[3] H.-P. Le, S. R. Sanders and E. Alon, "Design techniques for fully integrated switched-capacitor DC-DC converters," *IEEE Journal of Solid-State Circuits,* vol. 46, no. 9, pp. 2120-2131, Sep. 2011.

[4] M. Seeman, V. W. Ng, H.-P. Le, M. John, E. Alon and S. R. Sanders, "A comparative analysis of switched-capacitor and inductor-based dc-dc conversion technologies," in *2010 IEEE 12th Workshop on Control and Modeling for Power Electronics (COMPEL)*, Boulder, CO, Jun. 2010, pp. 1-7.

[5] S. R. Sanders, E. Alon, H.-P. Le, M. D. Seeman, M. John and V. Ng, "The road to fully integrated DC-DC conversion via the switched-capacitor approach," *IEEE Transactions on power electronics,* vol. 28, no. 9, pp. 4146-4155, Sep. 2013.

[6] V. Ng and S. R. Sanders, "Switched capacitor DC-DC converter: superior where the buck converter has dominated," PhD Dissertation, University of California, Berkeley, Berkeley, CA, 2011.

[7] S. E. Alper and T. Akin, "Symmetrical and decoupled nickel microgyroscope on insulating substrate," *Sensors and Actuators A: Physical,* vol. 115, no. 2, pp. 336-350, Jun. 2004.

[8] Z. Yao, S. Chen, D. Denniston and C. Goldsmith, "Micromachined low-loss microwave switches," *Journal of Micromechanical Systems,* vol. 8, no. 2, pp. 129-134, June 1999.

[9] R. E. Mihailovich, M. Kim, J. B. Hacker, E. A. Sovero, J. Studer, J. A. Higgins and J. F. DeNatale, "MEM relay for reconfigurable RF circuits," *IEEE Microwave and Wireless Components Letters,* vol. 1.11, no. 2, pp. 53-55, Feb. 2001.

[10] S. Majumder, J. Lampen, R. Morrison and J. Maciel, "A packaged, high-lifetime ohmic MEMS RF switch," in *Microwave Symposium Digest, 2003 IEEE MTT-S International*, Philadelphia, PA, Jun. 2003, vol. 3, pp1935-1938.

[11] S. Pacheco, C. T.-C. Nguyen and L. P. Katehi, "Design of low actuation voltage RF MEMS switch," in *IEEE MTT-S International Microwave Symposium Digest*, Boston, MA, Jun. 2000, pp. 165-168.

[12] Y.-W. Lin, "Low phase noise micromechanical reference oscillators for wireless communications," PhD Dissertation, Univeristy of Michigan, Ann Arbor, Ann Arbor, MI, 2007.

[13] C. T.-C. Nguyen, "Micromechanical signal processors," PhD Dissertation, University of California, Berkeley, Berkeley, CA, 1994.

[14] J. E.-Y. Lee, B. Nahreyni, Y. Zhu and S. A. Ashwin, "A single-crystal-silicon bulk-acoustic-mode microresonator oscillator," *IEEE Electron Device Letters,* vol. 29, no. 7, pp. 701-703, 2009.

[15] C. L. Goldsmith, Z. Yao, S. Eshelman and D. Denniston, "Performance of Low-Loss RF MEMS capacitive switches," *IEEE Microwave and Guided Wave Letters,* vol. 8, no. 8, pp. 269-271, Aug. 1998.

[16] P. Grant and M. Denhoff, "A comparison between RF MEMS switches and semiconductor switches," in *Proceedings 2004 International Conference on MEMS, NANO and Smart Systems (ICMENS'04)*, Aug. 2004, pp. 515-521.

[17] H. Kamitsuna, Y. Yamane, M. Tokumitsu, H. Sugahara and M. Muraguchi, "A fast low-power 4×4 switch IC using InP HEMTs for 10-Gbit/s Systems," in *2004 IEEE Compound Semiconductor Integrated Circuit Symposium*, Oct. 2004, pp. 97-100.

[18] S. Majumder, J. Lampen, R. Morrison and J. Maciel, "MEMS switches," *IEEE Instrumentation & Measurement Magazine,* pp. 12-15, March 2003.

[19] N. Mohan, T. M. Undeland and W. P. Robbins, Power Electronics: Converters, Applications and Design, Hoboken, NJ: John Wiley & Sons, 2003.

[20] J. F. Dickson, "On-chip high-voltage generation in MNOS integrated circuits using an improved voltage multiplier technique," *IEEE Journal of Solid-State Circuits,*

vol. 11, no. 3, pp. 374-378, 1976.

[21] R. D. Middlebrook, "Small-signal modeling of pulse-width modulated switching-mode power converters," *Proceedings of the IEEE,* vol. 76, no. 4, pp. 343-354, 1988.

[22] S. Rajapandian, K. L. Shepard, P. Hazucha and T. Karnik, "High-voltage power delivery through charge recycling," *IEEE Journal of Solid-State Circuits,* vol. 41, no. 6, pp. 1400-1410, 2006.

[23] A. D. Sokal and N. O. Sokal, "Class E-A new class of high-efficiency tuned single-ended switching power amplifiers," *IEEE Journal of Solid-State Circuits,* vol. 10, no. 3, pp. 168-176, 1975.

[24] K.-C. Tsai and P. R. Gray, "A 1.9GHz 1W CMOS class E power amplifier for wireless communications," in *Proceedings of the 24th European Solid-State Circuits Conference, 1998 (ESSCIRC'98)*, Hague, Netherlands, Sep. 1998, pp. 76-79.

[25] S. Wolf, Silicon Processing for the VLSI Era Volume 3-The Submicron MOSFET, Sunset Beach, CA: Lattice Press, 1995.

[26] Y. C. Woo, H. K. Lee, D. Lee, J. Lai and T.-J. K. Liu, "Compact Nano-Electro-Mechanical Non-Volatile Memory (NEMory) for 3D Integration," in *Technical Digest, 2007 IEEE International Electron Devices Meeting (IEDM'07)*, Washington, DC, Dec. 2007, pp. 603-606.

[27] Z. J. Guo, N. E. McGruer and G. G. Adams, "Modeling, simulation and measurement of the dynamic performance of an ohmic contact, electrostatically actuated RF MEMS switch," *Journal of Micromechanics and Microengineering,* vol. 17, no. 9, pp. 1899-1909, 2007.

[28] Y.-W. Lin, S. Lee, S.-S. Li, Y. Xie, Z. Ren and C. T.-C. Nguyen, "Series-resonant VHF micromechanical resonator reference oscillators," *IEEE Journal of Solid-State Circuits,* vol. 39, no. 12, pp. 2477-2491, Dec. 2004.

[29] K. L. Johnson, Contact Mechanics, New York: Cambridge University Press, 1987.

[30] F. D. Bannon, III, J. R. Clark and C. T.-C. Nguyen, "High-Q HF microelectromechanical filters," *IEEE Journal of Solid-State Circuits,* vol. 35, no. 4, pp. 512-526, Apr. 2000.

[31] E. Quevy, B. Legrand, D. Collard and L. Buchaillot, "Tapping-mode HF nanometric lateral gap resonators experimental and theory," in *Digest of Technical Papers, the 12th International Conference on Solid-State Sensors, Actuators and Microsystems (Transducers'03)*, Boston, MA, Jun. 2003, pp. 879-882.

[32] K. Wang, A.-C. Wong and C. T.-C. Nguyen, "VHF free-free beam high-Q micromechanical resonators," *Journal of Micromechanical Systems,* vol. 9, no. 3, pp. 347-360, Sept. 2000.

[33] J. Wang, Z. Ren and C. T.-C. Nguyen, "1.156-GHz self-aligned vibrating micromechanical disk resonator," *IEEE Transactions on Ultrasonics, Ferroelectrics and Frequency Control,* vol. 51, no. 12, pp. 1607-1628, Dec. 2004.

[34] Y. Xie, S.-S. Li, Y.-W. Lin, Z. Ren and C. T.-C. Nguyen, "1.52-GHz micromechanical extensional wine-glass mode ring resonators," *IEEE Transactions on Ultrasonics, Ferroelectrics and Frequency Control,* vol. 55, no. 4, pp. 890-907, Apr. 2008.

[35] H. S. Newman, J. L. Ebel, D. Judy and J. Maciel, "Lifetime measurements on a high-reliability RF-MEMS contact switch," *Microwave and Wireless Components Letters,* vol. 18, no. 2, pp. 100-102, 2008.

[36] W. Zhang, W. Zhang and K. L. Turner, "Nonlinear Dynamics of Micro Impact Oscillators in High Frequency MEMS," in *Digest of Technical Papers, the 13th International Conference on Solid-State Sensors, Actuators and Microsystems (Transducers'05)*, Seoul, Korea, Jun. 2005, pp. 768-771.

[37] Y. Lin, W.-C. Li, Z. Ren and C. T.-C. Nguyen, "The micromechanical resonant switch ("Resoswitch")," in *Technical Digest, 2008 Solid-State Sensor, Actuator, and Microsystems Workshop*, Hiltion Head, SC, Jun. 2008, pp. 40-43.

[38] Y. Lin, T. Riekkinen, W.-C. Li, E. Alon and C. T.-C. Nguyen, "A metal micromechanical resonant switch for on-chip power applications," in *Technical Digest, 2011 IEEE International Electron Devices Meeting (IEDM'11)*, Washington DC, Dec. 2011, pp. 20.6.1-20.6.4.

[39] I. Aoki, S. Kee, R. Magoon, R. Aparicio, F. Bohn, J. Zachan, G. Hatcher, D. McClymont and A. Hajimiri, "A fully-integrated quad-band GSM/GPRS CMOS power amplifier," *IEEE Solid-State Circuits,* vol. 43, no. 12, pp. 2747-2758, 2008.

[40] D. A. Blackwell, D. E. Dawson and D. C. Buck, "X-band MMIC switch with 70 dB isolation and 0.5 dB insertion loss," in *Digest of Papers, IEEE 1995 Microwave and Millimeter-Wave Monolithic Circuits Symposium*, Orlando, FL, May 1995, pp. 97-100.

[41] J. Putnam, M. Barter, K. Wood and J. LeBlanc, "A monolithic GaAs PIN switch network for a 77 GHz automotive collision warning radar," in *1997 IEEE Radio Frequency Integrated Circuits (RFIC) Symposium*, Burlington, MA, Jun. 1997, pp. 225-228.

[42] Y. Lin, W.-C. Li, G. Ilya, S.-S. Li, Y.-W. Lin, Z. Ren, B. Kim and C. T.-C. Nguyen, "Digitally-specified micromechanical displacement amplifiers," in *Technical Digest, the 15th International Conference on Solid-State Sensors, Actuators and Microsystems (Transducers'09)*, Denver, CO, Jun. 2009, pp. 781-784.

[43] B. Kim, Y. Lin, W.-L. Huang, M. Akgul, W.-C. Li, Z. Ren and C. T.-C. Nguyen, "Micromechanical resonant displacement gain stages," in *Technical Digest, IEEE 22nd International Conference on Micro Electro Mechanical Systmes, 2009. MEMS 2009*, Sorrento, Italy, Jan. 2009, pp. 19-22.

[44] W.-L. Huang, Z. Ren, Y.-W. Lin, H.-Y. Chen, J. Lahann and C. T.-C. Nguyen, "Fully monolithic CMOS nickel micromechanical resonator oscillator," in *Technical Digest, IEEE 21st International Conference on Micro Electro Mechanical Systems (MEMS'08)*, Tucson, AZ, Jan. 2008, pp. 10-13.

[45] W.-T. Hsu, J. R. Clark and C. T.-C. Nguyen, "A sub-micron capacitive gap process for multiple-metal-electrode lateral micromechanical resonators," in *Technical Digest, The 14th IEEE International Conference on Micro Electro Mechanical Systems (MEMS'01)*, Interlaken, Switzerland, Jan. 2001, pp. 349-352.

[46] Y.-W. Lin, S.-S. Li, Z. Ren and C. T.-C. Nguyen, "Low phase noise array-composite micromechanical wine-glass disk oscillator," in *Technical Digest, IEEE Internation Electron Device Meeting, IEDM'05*, Washington, DC, Dec. 2005, pp. 287-290.

[47] S.-S. Li, Y.-W. Lin, Z. Ren and C. T.-C. Nguyen, "An MSI micromechanical differential disk array filter," in *Digest of Technical Papers, the 14th International Conference on Solid-State Sensors & Actuators, Transducers'07*, Lyon, France, Jun. 2007, pp. 307-311.

[48] M. U. Demirci and C. T.-C. Nguyen, "Mechanically corner-coupled square microresonator array for reduced series motional resistance," *Journal of Microelectromechanical Systems,* vol. 16, no. 6, pp. 1419-1436, Dec. 2006.

[49] R. A. Johnson, Mechanical filters in electronics, New York: John Wiley & Sons, 1983.

[50] Y.-W. Lin, L.-W. Hung, S.-S. Li, Z. Ren and C. T.-C. Nguyen, "Quality factor boosting via mechanically-coupled arraying," in *Digest of Technical Papers, the 14th Internation Conference on Solid-State Sensors & Actuators, Transducers'07*, Lyon, France, Jun. 2007, pp 2453-2456.

[51] J. R. Clark, W.-T. Hsu, M. A. Abdelmoneum and C. T.-C. Nguyen, "High-Q UHF micromechanical radial-contour mode disk resonators," *Journal of Microelectromechanical Systems,* vol. 14, no. 6, pp. 1298-1310, Dec. 2005.

[52] J. Maciel, S. Majumder, R. Morrison and J. Lampen, "Lifetime characteristics of ohmic MEMS switches," in *Proceedings, Micromachining and Microfabrication, International Society for Optics and Photonics*, Jan. 2004, pp. 9-14.

[53] A. Shirane, H. Ito, N. Ishihara and K. Masu, "A 21V output charge pump circuit with appropriate well-bias supply technique in 0.18μm Si CMOS," in *Proceedings of*

the 2011 International SoC Design Conference (ISOCC), Jeju, Korea, Nov. 2011, pp. 28-31.

[54] W.-T. Hsu, "Recent Progress in Silicon MEMS Oscillators," in *Proceedings of the 40th Annual Precise Time and Time Interval Meeting*, Reston, VA, Dec. 2008, pp. 135-146.

[55] J. Wang, J. Huffman, P. Pinheiro and J. Hall, "An Integrated Low-Power High-Voltage Driving Circuit for Digital Micromirror Devices (DMD)," in *Digest of Technical Papers International Conference on Consumer Electronics, 2009. ICCE'09*, Las Vegas, NV, Jan. 2009, pp. 1-2.

[56] T. Tanzawa and T. Tanaka, "A dynamic analysis of the Dickson charge pump circuit," *IEEE Journal of Solid-State Circuits,* vol. 32, no. 8, pp. 1231-1240, Aug. 1997.

[57] M. R. Hoque, T. McNutt, J. Zhang, A. Mantooth and M. Mojarradi, "A high voltage Dickson charge pump in SOI CMOS," in *Proceedings of the IEEE 2003 Custom Integrated Circuits Conference*, San Jose, CA, Sep. 2003.

[58] C. T.-C. Nguyen, "MEMS-based RF channel-selection for true software-defined cognitive radio and low power sensor communications," *IEEE Communication Magazine,* vol. 51, no. 4, pp. 110-119, Apr. 2013.

[59] T. L. Naing, T. Beyazoglu, L. Wu, M. Akgul, Z. Ren, T. O. Rocheleau and C. T.-C. Nguyen, "2.97-GHz CVD diamond ring resonator with Q >40,000," in *Proceedings of the 2012 IEEE International Frequency Control Symposium (FCS'12)*, Baltimore, MD, May 2012, pp. 1-6.

[60] S.-S. Li, Y.-W. Lin, Y. Xie, Z. Ren and C. T.-C. Nguyen, "Charge-biased vibrating micromechanical resonators," in *Proceedings of the 2005 IEEE Ultrasonics Symposium*, Rotterdam, Netherlands, Sep. 2005, pp. 1596-1599.

[61] P. Khanna, "High voltage conversion for MEMS applications using micromachined capacitors," MS Thesis, University of South Florida, Tampa, FL, 2004.

[62] C. H. Haas and M. Kraft, "Modelling and analysis of a MEMS approach to dc voltage step-up conversion," *Journal of Micromechanics and Microengineering,* vol. 14, no. 9, pp. S114-S122, 2004.

[63] J. M. Noworolski and S. R. Sanders, "An electrostatic microresonant power conversion device," in *23rd Annual IEEE Power Electronics Specialists Conference (PESC'92)*, Toledo, OH, Jun. 1992, pp. 997-1002.

[64] M. Hill and C. O. Mahony, "Modelling and performance evaluation of a MEMS dc/dc converter," *Journal of micromechanics and microengineering,* vol. 16, no. 6, pp. S149-S155, 2006.

[65] P. Valizadeh, Y. Yang and P. Famouri, "A CMOS compatible MEMS-based voltage multiplier for on-chip generation of large DC voltages," in *2006 Conference on Optoelectronic and Microelectronic Materials and Devices*, Perth, WA, Dec. 2006, pp. 117-120.

[66] M. Innocent, P. Wambacq, S. Donnay, W. Sansen and H. D. Man, "A linear high voltage charge pump for MEMs applications in 0.18μm CMOS technology," in *Proceedings of the 29th European Solid-State Circuits Conference, 2003. ESSCIRC'03.*, Estoril, Portugal, Sep. 2003, pp. 457-460.

[67] Y. Lin, W.-C. Li, Z. Ren and C. T.-C. Nguyen, "A resonance dynamical approach to faster, more reliable micromechanical switches," in *Proceedings of the 2008 IEEE International Frequency Control Symposium*, Honolulu, HI, May 2008, pp. 640-645.

[68] C. Budd and F. Dux, "Chattering and related behaviour in impact oscillators," *Philosophical Transactions of the Royal Society of London. Series A: Physical And Engieering Sciences,* vol. 347, no. 1683, pp. 365-389, May 1994.

[69] Y. Lin, R. Liu, W.-C. Li, M. Akgul and C. T.-C. Nguyen, "A micromechanical resonant charge pump," in *Proceedings, 2013 Transducers and Eurosensors XXVII: The 17th International Conference on Solid-State Sensors, Actuators and Microsystems (TRANSDUCERS & EUROSENSORS XXVII)*, Barcelona, Spain, Jun. 2013, pp. 1727-1730.

[70] P. Shrestha, D. Gu, N. H. Tran, K. Tapily, H. Baumgart and G. Namkoong, "Investigation of Volmer-Weber growth during the nucleation phase of ALD platinum thin films and template based platinum nanotubes," *ECS Transactions,* vol. 33, no. 2, pp. 127-134, 2010.

[71] J. A. Starzyk, Y.-W. Jan and F. Qiu, "A DC-DC charge pump design based on voltage doublers," *IEEE Transactions on Circuits and Systems I: Fundamental Theory and Applications,* vol. 48, no. 3, pp. 350-359, Mar. 2001.

[72] M. S. Makowski, "Realizability conditions and bounds on synthesis of switched-capacitor DC-DC voltage multiplier circuits," *IEEE Transactions on Circuits and Systems I: Fundamental Theory and Applications,* vol. 44, no. 8, pp. 684-691, Aug. 1997.

[73] J. Wang, Y. Xie and C. T.-C. Nguyen, "Frequency tolerance of RF micromechanical disk resonators in nanocrystalline diamond and polysilicon structural materials," in *Technical Digest, 2005 IEEE International Electron Device Meeting (IEDM'05)*, Washington, DC, Dec. 2005, pp. 291-294.

[74] J. Wang, J. E. Butler, T. Feygelson and C. T.-C. Nguyen, "1.51-GHz polydiamond micromechanical disk resonator with impedance mismatched isolating support," in *Proceedings, the 17th IEEE International Conference on Micro Electro Mechanical*

Systems, 2004 (MEMS'04), Maastricht, The Netherlands, Jan. 2004, pp. 641-644.

[75] C. T.-C. Nguyen, "MEMS technology for timing and frequency control," *IEEE Transactions on Ultrasonics, Ferroelectrics and Frequency Control,* vol. 54, no. 2, pp. 251-270, Feb. 2007.

[76] J. Mitola III and G. Q. Maguire Jr., "Cognitive radio: making software radios more personal," *IEEE Personal Communications,* vol. 6, no. 4, pp. 13-18, Aug. 1999.

[77] S.-S. Li, Y.-W. Lin, Z. Ren and C. T.-C. Nguyen, "Self-switching vibrating micromechanical filter bank," in *Proceedings, 2005 IEEE International Frequency Control Symposium and Exposition*, Vancouver, Canada, Aug. 2005, pp. 135-141.

[78] K. Wang and C. T.-C. Nguyen, "High-order medium frequency micromechanical filters," *IEEE Journal of Microelectromechanical Systems,* vol. 8, no. 4, pp. 534-557, Dec. 1999.

[79] S. Mitarai, M. Tada, S. Yanagawa, T. Yamaguchi, T. Kinoshita, M. Tanaka, K. Ikeda and K. Yamashita, "Embedded MEMS filter chip and its fabrication for VHF applications," in *Technical Digest, 2005 IEEE International Electron Device Meeting (IEDM'05)*, Washington, DC, Dec. 2005, pp. 299-302.

[80] W.-C. Li, Y. Lin and C. T.-C. Nguyen, "Metal micromechanical filter-power amplifier utilizing a displacement-amplifying resonant switch," in *Proceedings, 2013 Transducers & Eurosensors XXVII, The 17th International Conference on Solid-State Sensors, Actuators and Microsystems (TRANSDUCERS & EUROSENSORS XXVII)*, Barcelona, Spain, Jun. 2013, pp. 2469-2472.

[81] Agilent Technologies, "Agilent solid state switches: selecting the right switch technology for your application," 2007.

[82] G. M. Rebeiz and J. B. Muldavin, "RF MEMS Switches and switch circuits," *IEEE Microwave Magazine,* vol. 2, no. 4, pp. 59-71, 2001.

Appendix   *Electroplated Nickel Resoswitch Process Outline*

The following comprises a step-by-step outline of the electroplated nickel process used to fabricate the nickel resoswitches presented in Chapter 3.

0.0   Starting Wafers: 8-12 ohm-cm, p-type, <100>

1.0   Insulation layer deposition

LTO (Tystar 11), 450°C, target = 2μm
Low stress nitride, 876°C, target = 200nm

2.0   Electrode (interconnect metal layer) deposition, lift off

2.1   Prime oven (or 120°C dehydration bake + 5min sink4 HMDS coating)

2.2   Spin on AZ5214IR photoresist (spinner1)

500 rpm for 4s
4k rpm for 30s
90°C soft bake 1min

2.3   Photolithography (Mask#1)

Initial Exposure (MA6: low vacuum contact mode 3~3.5s)
115°C Image reversal baking 1min
Flood Exposure (MA6: without mask for 25s)
Develop (svgdev: 4262 developer 90s)

2.4   Sputtered metal (Randex)

5nm NiTi

100nm Ni (Ar: 70sccm, Pressure: 2.5x10-5 Torr, Power: 100W, 9 minutes sputtering with cooling every minute)
Two steps of sputtering are done consecutively without venting
Measure sheet resistance (4ptprb)

    2.5   Ultrasonic liftoff in acetone

Place wafer in acetone beaker and put into ultrasonic tank
Wipe wafer in acetone using swabs if feature edge residues don't come off
Rinse wafer in methanol beaker
Clean beakers and repeat 2.5.1 and 2.5.2 for 2~3 times

3.0   Bottom sacrificial layer deposition

Sputter TiW (Randex), target = 700nm

4.0   Structural anchor definition

    4.1   Prime Oven (or 120OC dehydration bake + 5min sink4 HMDS coating)

    4.2   PR coating (svgcoat2: I-line 1.1 um and bake 90OC for 60s)

    4.3   Photolithography (Mask#2)

MA6: low vacuum contact mode for 13s

    4.4   Develop (svgdev: 4262 developer 60s + PEB)

    4.5   TiW dry etch (ptherm): SF_6+O_2

    4.6   Descum (technics-c: 50W for 1min)

5.0   Electroplate structural layer

    5.1   Make PR mode

Pime Oven (or 120°C dehydration bake + 5min sink4 HMDS coating)
PR coating (svgcoat2: SPR220-7.0 5 um (6k) and bake 90°C 100s)
Bake 115°C another 100s
Wait overnight or at least 3~5 hours
Photolithography (Mask#3)
Expose (MA6: low vacuum contact mode 20s)
Develop (LDD-26 40s)
Measure mold thickness (asiq)

    5.2   Nickel solution preparation

Nickel sulphamate solution + boric acid (30g/L) at 50°C
The hotplate temperature is around 90°C to get 50°C in the solution (2L). Normally, need about 1650~1700ml before putting in anode and cathode, so boric acid would be around 50g in total. Mix them adequately, make sure no particles are in the solution, sometimes filtering is required. May heat up the solution to around 90~95°C to expedite the dissolving.

5.3   Electroplate Nickel, target = 2-3μm

Clean everything with DI water gun
Open PR window for cathode clamping using acetone
Rinse wafer using DI water and submerge in the solution and wait 1-3 minutes (*note: try not to submerge the cathode clamp*)
Calculate plating current according to current density and plating area and then turn on the current source and time the electroplating

5.4   Electroplate Cu as top spacer, target = 1-2μm

RTU copper plating solution
Room temperature, same plating current

5.5   Strip PR mold in acetone, rinse 3-4 times in methanol and DI water

6.0   Sidewall spacer deposition

Sputter TiW (Randex), target = 80nm

7.0   Electrode anchor definition

7.1   Prime Oven (or 120°C dehydration bake + 5min sink4 HMDS coating)

7.2   PR coating (svgcoat2: I-line 1.1 um and bake 90°C 60s)

7.3   Photolithography (Mask#4)

MA6: low vacuum contact mode for 13s

7.4   Develop (svgdev: 4262 developer 60s + PEB)

7.5   TiW dry etch (ptherm): SF_6+O_2, cooling every minute

7.6   Descum (technics-c: 50W for 1min)

8.0   Electroplate electrode layer

8.1   Make PR mode

Pime Oven (or 120°C dehydration bake + 5min sink4 HMDS coating)
PR coating (svgcoat2: SPR220-7.0 5 um (6k) and bake 90°C 100s)
Bake 115oC another 100s
Wait overnight or at least 3~5 hours
Photolithography (Mask#3)
Expose (MA6: low vacuum contact mode 20s)
Develop (LDD-26 40s)
Measure mold thickness (asiq)

8.2   Electroplate Nickel, target = 2-3μm

8.3   Strip PR mold in acetone, rinse 3-4 times in methanol and DI water

9.0   Release in mixture of H$_2$O (100ml), H$_2$O$_2$ (100ml) and NH$_4$OH (5ml)